



NRL/MR/6110--10-9235

**Quantification of Noise Sources in EMI Surveys  
Technology Demonstration Report  
Army Research Laboratory  
Blossom Point, Maryland  
July – September, 2006**

G.R. HARBAUGH

D.A. STEINHURST

*Nova Research, Inc.  
Alexandria, Virginia*

M. HOWARD

*NAEVA Geophysics, Inc.  
Charlottesville, Virginia*

B.J. BARROW

J.T. MILLER

T.H. BELL

*SAIC, Inc. - ASAD  
Arlington, Virginia*

January 14, 2010

Approved for public release; distribution is unlimited.

REPORT DOCUMENTATION PAGE				Form Approved OMB No. 0704-0188	
Public reporting burden for this collection of information is estimated to average 1 hour per response, including the time for reviewing instructions, searching existing data sources, gathering and maintaining the data needed, and completing and reviewing this collection of information. Send comments regarding this burden estimate or any other aspect of this collection of information, including suggestions for reducing this burden to Department of Defense, Washington Headquarters Services, Directorate for Information Operations and Reports (0704-0188), 1215 Jefferson Davis Highway, Suite 1204, Arlington, VA 22202-4302. Respondents should be aware that notwithstanding any other provision of law, no person shall be subject to any penalty for failing to comply with a collection of information if it does not display a currently valid OMB control number. <b>PLEASE DO NOT RETURN YOUR FORM TO THE ABOVE ADDRESS.</b>					
1. REPORT DATE (DD-MM-YYYY) 14-01-2010		2. REPORT TYPE Interim Report		3. DATES COVERED (From - To) April 1, 2006 to October 8, 2008	
4. TITLE AND SUBTITLE  Quantification of Noise Sources in EMI Surveys Technology Demonstration Report Army Research Laboratory Blossom Point Facility, Maryland July – September, 2006				5a. CONTRACT NUMBER	
				5b. GRANT NUMBER	
				5c. PROGRAM ELEMENT NUMBER 0603851D8Z	
				5d. PROJECT NUMBER MM-0508	
6. AUTHOR(S)  G.R. Harbaugh,* D.A. Steinhurst,* M. Howard,† B.J. Barrow,‡ J.T. Miller,‡ and T.H. Bell‡				5e. TASK NUMBER	
				5f. WORK UNIT NUMBER 61-5802-H-9	
				8. PERFORMING ORGANIZATION REPORT NUMBER  NRL/MR/6110--10-9235	
7. PERFORMING ORGANIZATION NAME(S) AND ADDRESS(ES)  Naval Research Laboratory, Code 6110 4555 Overlook Avenue, SW Washington, DC 20375-5320				10. SPONSOR / MONITOR'S ACRONYM(S)  ESTCP	
9. SPONSORING / MONITORING AGENCY NAME(S) AND ADDRESS(ES)  Environmental Security Technology Certification Program (ESTCP) Program Office 901 North Stuart Street, Suite 303 Arlington, VA 22203				11. SPONSOR / MONITOR'S REPORT NUMBER(S)	
12. DISTRIBUTION / AVAILABILITY STATEMENT  Approved for public release; distribution is unlimited.					
13. SUPPLEMENTARY NOTES *Nova Research, Inc., 1900 Elkin Street, Suite 230, Alexandria, VA 22308 †NAEVA Geophysics, Inc., P.O. Box 7325, Charlottesville, VA 22906 ‡SAIC, Inc. - ASAD, 1225 South Clark Street, Suite 800, Arlington, VA 22202					
14. ABSTRACT  This demonstration was conducted at the Army Research Laboratory Blossom Point Facility between July and September 2006. The magnitudes and effects of several types of background and/or noise sources on the data collected with several commonly used EMI sensors were measured. These noise sources included ground response/geology, inherent sensor noise, external noise sources, motion-induced noise, and position uncertainty. Using Monte Carlo simulations, the impact of each noise source on the final fitted parameters result was determined. Additional measurements were conducted at Blossom Point and other nearby locations to help separate the individual contributions of the convolved sources. The Blossom Point site was found to provide a good benchmark for a site where it should be feasible to conduct a survey-mode EMI survey. Two recommendations are provided as to a set of EMI sensors and a demonstration protocol to be used for future demonstrations. From these results, we can begin to understand real world EMI survey noise sources, and quantify these effects in terms of meaningful survey configuration parameters, such as lane spacing.					
15. SUBJECT TERMS Unexploded Ordnance (UXO)      Noise sources      Classification Electromagnetic Induction (EMI)      Survey background levels      Discrimination					
16. SECURITY CLASSIFICATION OF:			17. LIMITATION OF ABSTRACT  UL	18. NUMBER OF PAGES  134	19a. NAME OF RESPONSIBLE PERSON B.J. Spargo, NRL, Code 6110
a. REPORT Unclassified	b. ABSTRACT Unclassified	c. THIS PAGE Unclassified			19b. TELEPHONE NUMBER (include area code) (202) 404-6392

# Contents

Figures.....	vii
Tables.....	xiv
Acronyms Used.....	xv
1. Introduction .....	1
1.1 Background.....	1
1.2 Objectives of the Demonstration .....	1
1.3 Regulatory Drivers.....	2
1.4 Stakeholder / End User Issues.....	2
2. Technology Description .....	2
2.1 Technology Development and Application .....	2
2.1.1 Geophysical Instruments.....	2
2.1.1.1 Geonics EM61 MkII .....	3
2.1.1.2 Geonics EM63 .....	4
2.1.1.3 Geophex GEM-3.....	5
2.1.1.4 Position and Orientation .....	6
2.1.2 NRL Low Frequency Spectrum Analyzer .....	7
2.2 Data Collection and Preprocessing.....	8
2.2.1 Inherent Sensor Noise.....	8
2.2.2 Motion-Induced Noise .....	8
2.2.3 External Noise.....	10
2.2.4 Geologic Response.....	12
2.2.5 Location Uncertainties .....	14

2.3	Data Analysis .....	15
2.4	Previous Testing of the Technology .....	15
2.5	Factors Affecting Cost and Performance .....	15
2.6	Advantages and Limitations of the Technology .....	16
3.	Demonstration Design .....	16
3.1	Performance Objectives .....	16
3.2	Test Site Selection.....	17
3.2.1	Test Site History / Characteristics.....	17
3.2.2	Climate .....	18
3.2.3	Geology .....	20
3.2.4	Test Locations within Blossom Point .....	21
3.2.4.1	Environmental Area .....	21
3.2.4.2	Boat Launch .....	21
3.2.4.3	L Range .....	22
3.3	Present Operations .....	23
3.4	Pre-Demonstration Testing and Analysis .....	23
3.5	Testing and Evaluation Plan .....	23
3.5.1	Demonstration Set-Up and Start-Ups .....	23
3.5.2	Period of Operation.....	23
3.5.3	Scope of Demonstration.....	24
3.5.4	Residuals Handling .....	24
3.5.5	GPS Control Monuments .....	24
3.5.6	Operational Parameters for the Technology .....	25
3.5.7	Demobilization.....	25

3.5.8	Health and Safety Plan (HASP).....	25
3.6	Characterization of the Soil by Standard Techniques.....	25
3.6.1	Soil Moisture.....	25
3.6.2	Magnetic susceptibility of soils .....	28
3.7	Analysis of the GEM-3 Data.....	29
3.7.1	External Noise.....	29
3.7.2	Inherent Noise .....	32
3.7.3	Geological Response.....	35
3.7.4	Motion-Induced Noise .....	43
3.8	Analysis of the EM61 MkII Data.....	71
3.8.1	Sensor Variability .....	71
3.8.2	External Noise.....	76
3.8.3	Inherent Noise .....	77
3.8.4	Geologic Response.....	79
3.8.5	Motion-Induced Noise .....	81
3.9	Monte Carlo Study .....	94
3.9.1	Objective .....	94
3.9.2	The Monte Carlo Approach .....	94
3.9.3	System under Study .....	94
3.9.4	Stochastic Model.....	94
3.9.4.1	STEP 1. The Target is Defined.....	95
3.9.4.2	STEP 2. The Survey is Defined .....	97
3.9.4.3	STEP 3. Synthetic Data are Created .....	100
3.9.4.4	STEP 4. Observed Data are Created .....	100

3.9.4.5	STEP 5. Observed Data are Inverted .....	101
3.9.4.6	Standard inversion .....	103
3.9.4.7	Dynamic Response Inversion .....	103
3.9.5	Results.....	104
3.10	Management and Staffing .....	108
4.	Future Demonstrations .....	108
4.1	Full-Scale EMI Noise Characterization Demonstration .....	108
4.1.1	EMI Sensors.....	109
4.1.2	Measurements .....	111
4.1.3	Deliverables .....	111
4.2	EM61 MkII Simulation Tool Demonstration .....	111
4.2.1	EMI Sensors.....	111
4.2.2	Measurements .....	112
4.2.3	Deliverables .....	112
5.	Cost Assessment.....	113
6.	References .....	114
7.	Points of Contact .....	116
Appendix A.	Health and Safety Plan.....	117
Appendix B.	Dipole Model Framework.....	119

## Figures

Figure 2-1 – Geonics EM61 MkII coils on a test platform.....	3
Figure 2-2 – Geonics EM63 with electronics and data logger, on a test platform .....	5
Figure 2-3 – Geophex GEM-3 sensor head (40cm diameter) and electronics.....	6
Figure 2-4 – NRL Low-Frequency Spectrum Analyzer .....	7
Figure 2-5 – Man-portable cart.....	9
Figure 2-6 – Rail system and test tower.....	9
Figure 2-7 – MTADS EM trailer .....	9
Figure 2-8 – Voltage time series from spectrum analyzer.....	10
Figure 2-9 – Relative power spectral density results from horizontal and vertical orientation of external noise monitor.....	11
Figure 2-10 – Rail system deployed at Boat Launch area, shown with Geonics EM-63 in position.....	12
Figure 2-11 – Data collection scheme used at individual stations on the rail system. See text for further description. ....	13
Figure 2-12 – GEM-3 ground response results for the Environmental Area.....	13
Figure 2-13 – EM63 time gate 1 response at Boat Launch.....	14
Figure 3-1 – Location of Army Research Laboratory Blossom Point Facility .....	18
Figure 3-2 – Topographic Map of Blossom Point Research Facility, showing locations of selected EMI Noise Test sites .....	19
Figure 3-3 – Climate data for LaPlata, MD .....	19
Figure 3-4 – Geologic Map and Cross Section (McCartan, 1989) showing Cedar Point Neck .....	20
Figure 3-5 – Environmental Area, view to the East.....	21
Figure 3-6 – Boat Landing Area, view to the southwest .....	22
Figure 3-7 – Active Range Test Location, L-Range, view to the East .....	23

Figure 3-8 – Moisture content profiles for the Boat Launch, Environmental, and L-Range areas .....	27
Figure 3-9 – Magnetic susceptibility profile for the Environmental Area.....	28
Figure 3-10 – Magnetic susceptibility profile for the Boat Launch Area.....	28
Figure 3-11 – Magnetic susceptibility profile for the L-Range traverses.....	29
Figure 3-12 – Power Spectra Results for the GEM-3 Sensor in both Passive and Active Monitoring Modes .....	31
Figure 3-13 – GEM-3 Static Measurements – Lower Frequencies. In-phase signals are shown in black and quadrature signals are shown in red. The lowest white noise level at 3930 Hz is indicated with a dotted line in the right-hand panels. ....	33
Figure 3-14 – GEM-3 Static Measurements – Upper Frequencies. In-phase signals are shown in black and quadrature signals are shown in red. The lowest white noise level at 3930 Hz is indicated with a dotted line in the right-hand panels. ....	34
Figure 3-15 – White Noise Levels for GEM-3 Static Measurements. Measurements at each transmit frequency are shown as symbols (black diamonds – in-phase, red x's – quadrature). A polynomial fit to the data is shown as a dashed line. ....	35
Figure 3-16 – Soil Model Response for the GEM-3 sensor. In-phase response is shown in red and quadrature response is shown in red. The solid lines represent a soil conductivity of 0.01 mho/m, the dashed lines 0.1 mho/m. ....	36
Figure 3-17 – Soil Response for the GEM-3 at the Boat Launch Area. The experimental data are shown as black lines and symbols. The red lines in the left-hand panels represent model fits to each data set (measurement height). The colored lines in the right-hand panels represent model fits at a particular frequency as a function of measurement height. ....	38
Figure 3-18 – Soil Response for the GEM-3 at the Environmental Area. The experimental data are shown as black lines and symbols. The red lines in the left-hand panels represent model fits to each data set (measurement height). The colored lines in the right-hand panels represent model fits at a particular frequency as a function of measurement height. ....	39
Figure 3-19 – Match of frequency dependent susceptibility model (red and green curves) to measured GEM-3 soil response (black curves and symbols) at the Environmental Area. ....	41



Figure 3-20 – MTADS MP Cart Motion Characterization – X,Y,Z, Pitch, and Roll. The upper panel shows the local course-over-ground for several data sets. The data associated with the leg color-coded red was the data source for the following discussion. ....	44
Figure 3-21 – MTADS MP Cart Motion Characterization – IMU Angular Rates and Accelerations.....	45
Figure 3-22 – MTADS MP Cart – GEM-3 In-phase Response. The in-phase data for the five lowest frequencies are presented in the upper panels. The bottom panel presents the in-phase data for the five highest frequencies (black - 2,610 Hz, red – 5,430 Hz, green – 11,430 Hz, blue – 20,010 Hz, and magenta – 44, 370 Hz). ....	46
Figure 3-23 – MTADS MP Cart – GEM-3 Quadrature Response. The quadrature data for the five lowest frequencies are presented in the upper panels. The bottom panel presents the quadrature data for the five highest frequencies (black - 2,610 Hz, red – 5,430 Hz, green – 11,430 Hz, blue – 20,010 Hz, and magenta – 44, 370 Hz). ....	47
Figure 3-24 – MTADS MP Cart – Power spectra of the GEM-3 response and the IMU motion. An individual black line is show for each frequency in the upper panels (see text for discussion). The acceleration and angular rate PSDs are shown in the lower panels (X – black, Y – red, Z – green). The dotted line in the upper panel indicates the lowest white noise level measured in the stationary tests.....	49
Figure 3-25 – MTADS EM Trailer Motion Characterization – X,Y,Z, Pitch, and Roll. The upper panel shows the local course-over-ground for several data sets. The data associated with the leg color-coded red was the data source for the following discussion. ....	50
Figure 3-26 – MTADS EM Trailer Motion Characterization – IMU Angular Rates and Accelerations.....	51
Figure 3-27 – MTADS EM Trailer Motion Characterization – GEM-3 In-phase Response. The in-phase data for the five lowest frequencies are presented in the upper panels. The bottom panel presents the in-phase data for the five highest frequencies (black - 2,610 Hz, red – 5,430 Hz, green – 11,430 Hz, blue – 20,010 Hz, and magenta – 44, 370 Hz). ....	52
Figure 3-28 – MTADS EM Trailer Motion Characterization – GEM-3 Quadrature Response. The quadrature data for the five lowest frequencies are presented in the upper panels. The bottom panel presents the quadrature data for the five highest frequencies (black - 2,610 Hz, red – 5,430 Hz, green – 11,430 Hz, blue – 20,010 Hz, and magenta – 44, 370 Hz). ....	53

Figure 3-29 – MTADS EM Trailer Motion Characterization – Power spectra of the GEM-3 response and the IMU. An individual black line is show for each frequency in the upper panels. The acceleration and angular rate PSDs are shown in the lower panels (X – black, Y – red, Z – green). The dotted line in the upper panel indicates the lowest white noise level measured in the stationary tests.....	54
Figure 3-30 – Tower / Rail System Motion Characterization – X,Y,Z, Pitch, and Roll. ....	56
Figure 3-31 – Tower / Rail System Motion Characterization – IMU Angular Rates and Accelerations.....	57
Figure 3-32 – Tower / Rail System Motion Characterization – GEM-3 In-phase Response. The in-phase data for the five lowest frequencies are presented in the upper panels. The bottom panel presents the in-phase data for the five highest frequencies (black - 2,610 Hz, red – 5,430 Hz, green – 11,430 Hz, blue – 20,010 Hz, and magenta – 44, 370 Hz). ....	58
Figure 3-33 – Tower / Rail System Motion Characterization – GEM-3 Quadrature Response. The quadrature data for the five lowest frequencies are presented in the upper panels. The bottom panel presents the quadrature data for the five highest frequencies (black - 2,610 Hz, red – 5,430 Hz, green – 11,430 Hz, blue – 20,010 Hz, and magenta – 44, 370 Hz). ....	59
Figure 3-34 – Tower / Rail System Motion Characterization – Power spectra of the GEM-3 response and the IMU. An individual black line is show for each frequency in the upper panels. The acceleration and angular rate PSDs are shown in the lower panels (X – black, Y – red, Z – green). The dotted line in the upper panel indicates the lowest white noise level measured in the stationary tests.....	60
Figure 3-35 – GEM-3 RMS Noise (In-phase and Quadrature) by platform. The black curves are the stationary noise levels. The curves for each site are color-coded: Environmental – red, L Range – green, and Boat Launch – blue. ....	62
Figure 3-36 – IMU angular pitch rate versus the 90-Hz GEM-3 Response (In-phase and Quadrature) .....	63
Figure 3-37 – GEM-3 Response – Measured versus IMU-based Model for Noise. Experimental data are shown in black, modeled noise based on IMU data is shown in red. ....	65
Figure 3-38 – GEM-3 RMS Noise Levels as a Function of Transmit Frequency. The measured noise levels are shown as the solid lines and symbols (black – rapid pitching, red – medium pitching, blue – slow pitching, green –	

stationary). The dotted lines represent the expected scaling of the dB/dt noise with transmitter frequency.....	66
Figure 3-39 – Measured GEM-3 Noise and Modeled Noise for the Lower Transmitter Frequencies. The left-hand panels show the experimental data and the right-hand panels show the modeled results. The in-phase and quadrature responses are colored black and red, respectively. ....	68
Figure 3-40 – Measured GEM-3 Noise and Modeled Noise for the Upper Transmitter Frequencies. . The left-hand panels show the experimental data and the right-hand panels show the modeled results. The in-phase and quadrature responses are colored black and red, respectively. ....	69
Figure 3-41 – Three-Second Average RMS Noise for the GEM-3 Response and Models. The measured noise (black), modeled noise from $db/dt$ (red), and modeled noise from estimate motion relative to the ground (green) are shown. The $dB/dt$ model from the upper panel is shown in the lower panel a dashed red line as a reference.....	70
Figure 3-42 – Comparison of Response from Two EM61 MkII Electronics Packages. The response from one set of electronics is shown in red, one in black. The same set of coils were used for both measurements. ....	72
Figure 3-43 – Comparison of Response from EM61 MkII Electronics Packages and Two Sets of EM61 Coils to Several Standard Objects.....	74
Figure 3-44 – Comparison of Time Response from Two EM61 MkII Electronics Packages and Two Sets of EM61 Coils using a Circular Loop of Wire and a Fast Switch .....	75
Figure 3-45 – External Noise Relative Power Spectra as a Function of Detector Orientation at the Test Sites .....	76
Figure 3-46 – Averaged Relative Power Spectra for a Stationary EM61 MkII in a Quiet Location. The dotted lines represent the channel-specific noise floor (bit level). The red curves plot the power spectral response as determined by the sensor’s step response. ....	78
Figure 3-47 – Time-Domain Soil Response Measured using the EM61 MkII in 4-channel mode as a function of measurement height. The experimental data are shown as color-coded symbols and lines. The dashed lines represent the soil model discussed in the text as a function of sensor height. ....	80
Figure 3-48 – Time-domain soil response measured and modeled using single sensor from MM-0601 TEM array as a function of measurement height. The	

black lines are the experimental data and the green lines represent the model results. ....	80
Figure 3-49 – Power and Correlation Spectra for the EM61 MkII / MP Cart Combination at the Environmental Area versus IMU Data. The color-coded dashed lines in the upper-left panel are the time gate-specific bit-level noise for the sensor as found in Figure 3-46. The color-coded dotted lines in the upper-left panel are the time gate-specific stationary noise due to the sensor’s time response function as found in Figure 3-46. ....	82
Figure 3-50 – Time Rasters (left) and Power Spectra (right) for the EM61 MkII / MP Cart Combination at the Environmental Area. The red-dotted lines in the right-hand panels are the time gate-specific bit-level noise for the sensor as found in Figure 3-46. The black-dotted lines are the rms noise levels calculated on short time scales. ....	83
Figure 3-51 – Power and Correlation Spectra for the EM61 MkII / Towed Platform Combination at the Environmental Area versus IMU Data. The color-coded dashed lines in the upper-left panel are the time gate-specific bit-level noise for the sensor as found in Figure 3-46. The color-coded dotted lines in the upper-left panel are the time gate-specific stationary noise due to the sensor’s time response function as found in Figure 3-46. ....	85
Figure 3-52 – Time Rasters (left) and Power Spectra (right) for the EM61 MkII / Towed Platform Combination at the Environmental Area. The red-dotted lines in the right-hand panels are the time gate-specific bit-level noise for the sensor as found in Figure 3-46. The black-dotted lines are the rms noise levels calculated on short time scales. ....	86
Figure 3-53 – Power and Correlation Spectra for the EM61 MkII / Rail System Combination at the Environmental Area versus IMU Data. The color-coded dashed lines in the upper-left panel are the time gate-specific bit-level noise for the sensor as found in Figure 3-46. The color-coded dotted lines in the upper-left panel are the time gate-specific stationary noise due to the sensor’s time response function as found in Figure 3-46. ....	87
Figure 3-54 – Time Rasters (left) and Power Spectra (right) for the EM61 MkII / Rail System Combination at the Environmental Area. The red-dotted lines in the right-hand panels are the time gate-specific bit-level noise for the sensor as found in Figure 3-46. The black-dotted lines are the rms noise levels calculated on short time scales. ....	88
Figure 3-55 – EM61 MkII RMS Noise Levels for Several Platform by Time Gate .....	89
Figure 3-56 – Measured Response from an EM61 MkII while Undergoing Controlled Pitching. The top panel shows the sensor motion as measured by the	

IMU. The channel data are shown in the bottom panel as color-coded lines (time gates 1 – 4, magenta, blue, red, and green, respectively). The black line represents the modeled response using the IMU data. ....	90
Figure 3-57 – Modeled and Measured EM61 MkII Response (for Various Pitching Rates. The channel data are shown as color-coded lines (time gates 3 – red and 4 - green). The black line represents the modeled response using the IMU data. ....	91
Figure 3-58 – Modeled and Measured EM61 MkII Response for the MP Cart / EM61 MkII Combination at the Environmental Area. The experimental data for time gates 1,2,3 are shown in the upper panel. The measured angular rates from the IMU are shown in the middle panel. The bottom panel has the modeled noise results based on the above data.....	93
Figure 3-59 – Contour maps of synthetic EM61-MkII data, first time gate. The raw data (left image) shows the characteristic “chevron” pattern caused by the delayed onset of peak signals due to dynamic response of the sensor, which is moving at walking speed (~1 m/s). In the right image, a time lag is applied to the raw data, effectively shifting positions along-track until contours appear by eye to be aligned properly for further processing.....	102
Figure 3-60 – Output from this Monte Carlo study (left two graphs) compares with corresponding results from Camp Sibert (right two graphs) in which a large number of 4.2-in mortars were processed. The upper set of graphs shows the relationship between fit error and signal to noise ratio (SNR). The lower set shows the spread of recovered beta values. This comparison is imperfect since the man-portable system deployed at the former Camp Sibert is different from the system modeled in this study (Figure 2-5). Still, the broad trends encourage a sense that these results are reasonable representations of reality.....	105
Figure 3-61 – Predicted performance with different lane spacings. The upper panels show the fitted z results and the lower panels plot $\beta_2$ and $\beta_3$ versus $\beta_1$ . The solid line in the upper panels indicates where the fitted z equals the true z value. ....	107
Figure 3-62 – Predicted performance for other survey configurations. The upper panels show the fitted z results and the lower panels plot $\beta_2$ and $\beta_3$ versus $\beta_1$ . The solid line in the upper panels indicates where the fitted z equals the true z value. ....	108
Figure 4-1 – MTADS Discrimination Array Transients for Several Items .....	109
Figure 4-2 – EMI sensor developed during ESTCP MM-0601 .....	110

## Tables

Table 3-1 – Final Schedule for the EMI Noise Demonstration at Blossom Point.....	24
Table 3-2 – Coordinates of First-Order Control Points at Blossom Point.....	24
Table 3-3 – Moisture content measurements for the Boat Launch Area .....	26
Table 3-4 – Moisture content measurements for the Environmental Area.....	26
Table 3-5 – Moisture content measurements for the L-Range Area.....	27
Table 3-6 – Fitted Soil Model Parameters for the Blossom Point Test Areas.....	42
Table 3-7 – Steps of the Stochastic model.....	95
Table 3-8. Beta values for Monte Carlo sphere target. ....	96
Table 3-9 – Summary of sensor xyz travel simulation .....	99
Table 5-1 – Blossom Point Demonstration Costs .....	113

## Acronyms Used

<b>Abbreviation</b>	<b>Definition</b>
(PTNL,)AVR	Time, Yaw, Tilt, Range for Moving Baseline RTK NMEA-0183 message
(PTNL,)GGK	Time, Position, Position Type, DOP NMEA-0183 message
AGL	Above Ground Level
APG	Aberdeen Proving Ground
BP	US Army Research Laboratory Blossom Point Facility, MD
DoD	Department of Defense
DSB	Defense Science Board
DVD-R	Writable digital versatile disc
EM(I)	Electro-magnetic (Induction)
ESTCP	Environmental Security Technology Certification Program
FFT	Fast Fourier Transform
GPS	Global Positioning System
HASP	Health and Safety Plan
Hz	Hertz
IMU	Inertial Measurement Unit
MM	Munitions Management
MP	Man-portable
MTADS	Multi-sensor Towed Array Detection System
NAD83	North American Datum of 1983
NAVD88	North American Vertical Datum of 1988
NMEA	National Marine Electronics Association
NRL	Naval Research Laboratory
ppm	parts-per-million
PSD	Power Spectral Density
RMS	Root Mean Squared
RTK	Real Time Kinematic
SERDP	Strategic Environmental Research and Development Program
SI	International System of Units
SNR	Signal to Noise Ratio
TEM	Time-Domain Electro-magnetic Induction
TFM	Total-Field Magnetometry
UTC	Universal Coordinated Time
UTM	Universal Transverse Mercator
UXO	Unexploded Ordnance
VHF	Very High Frequency

# **Quantification of Noise Sources in EMI Surveys**

**Army Research Laboratory Blossom Point Facility, MD**

## **1. Introduction**

### **1.1 Background**

Unexploded Ordnance (UXO) detection and remediation is a high priority tri-service requirement. As the Defense Science Board wrote in 2003: “Today’s UXO cleanup problem is massive in scale with some 10 million acres of land involved. Estimated cleanup costs are uncertain but are clearly tens of billions of dollars. This cost is driven by the digging of holes in which no UXOs are present. The instruments used to detect UXOs (generally located underground) produce many false alarms, - i.e., detections from scrap metal or other foreign or natural objects -, for every detection of a real unexploded munition found.” [1]

There is general agreement that one solution to the false alarm problem involves the use of Electromagnetic Induction (EMI) sensors which can, in principle, allow the extraction of target shape parameters in addition to the size and depth estimates available from magnetometer measurements. We, and others, have fielded systems with either time-domain or frequency-domain EMI sensors with the goal of extracting reliable target shape parameters and, thus, improving the discrimination capability of our surveys. In practice, the discrimination ability of these sensors has been limited by signal-to-noise limitations. Part of this noise results from sensor design but a large fraction arises from causes external to the sensor such as location uncertainty, motion-induced noise, ground interaction, and external noise sources.

SERDP has funded several groups to develop ordnance-specific EMI sensors. Many of these groups are using simulations to investigate the performance of their prototype sensors in realistic environments. These simulations, along with those being conducted by algorithm developers, are limited by our lack of quantitative knowledge of the magnitude of the various noise sources. In this demonstration, we have obtained quantitative data at the first of a series of sites exhibiting a variety of noise environments. The results of this demonstration can be used to develop a knowledge base of magnitude and variation of the noise budget associated with various EMI sensors, the breadth of potential sites where these sensors might be deployed, and how to guide the design of these surveys.

### **1.2 Objectives of the Demonstration**

- In this demonstration, we have isolated, to the extent possible, and measured quantitatively the individual components of the noise budget for an EMI survey. These components include inherent sensor noise, motion-induced noise, external noise, ground interactions, and location uncertainties. Each of these terms will be discussed in more detail below. This demonstration was conducted at our home facility to accommodate an evolution of data collection schemes and techniques in response to the collected data, with a correspondingly long deployment schedule.



### **1.3 Regulatory Drivers**

DoD directives to develop new techniques and technologies to improve the efficiency of UXO cleanup at military training sites form the impetus for this study. Careful analysis of the sources contributing noise to EMI instrument readings will permit their effects to be anticipated and considered in the development and application of discrimination algorithms. As a result, cost savings will result from improved discrimination of UXO and non-UXO scrap at munitions sites. The primary benefit would be economic. A large portion of a typical UXO remediation involves digging non-ordnance targets. The Defense Science Board has calculated that if the false alarm rate can be reduced to 10:1, the economics of a UXO remediation can be inverted from 75% of the cost devoted to digging false alarms to 75% devoted to digging UXO. To accomplish this will require the development of both advanced sensors and advanced classification algorithms.

We address this issue in two ways. The quantitative measure of EMI noise sources that will result from this project will be an important tool for both sensor and algorithm developers and should enable them to make real progress in classification. More directly, we propose to use our acquired knowledge of EMI noise sources to formulate simple tests that can be performed on-site before an EMI survey and whose result can be used to optimize analysis and classification algorithms to reduce the number of false alarms.

### **1.4 Stakeholder / End User Issues**

End users of the information derived from this study are the site managers and regulators who oversee the nation's Formerly-Used Defense Sites, the contractors who routinely conduct EMI surveys for the purposes of site investigation and clearance, and the algorithm developers working to improve discrimination techniques. The utility of our results to the UXO detection and discrimination community will depend on the extent to which they are disseminated. We will present our results as they are obtained at conferences and symposia (SERDP/ESTCP Partners Symposium, SPIE, UXO/Countermines Forum, etc.) and publish our final results and analyses as NRL Memorandum Reports, which receive wide distribution, and in the archival literature.

## **2. Technology Description**

### **2.1 Technology Development and Application**

#### **2.1.1 Geophysical Instruments**

Three commonly used, commercially-available EMI geophysical instruments were used in this project to evaluate the primary noise sources affecting EMI sensors. The three instruments are the Geonics EM61 MkII and EM63 and the Geopex GEM-3.

### 2.1.1.1 Geonics EM61 MkII

The EM61 MkII is a pulsed-induction sensor which transmits a short electromagnetic pulse (a unipolar rectangular current pulse with a 25% duty cycle) into the Earth. The instrument consists of two air-core 1m x 0.5m coils housed in fiberglass, a backpack containing a battery and processing electronics, and an optional data logging device. The lower coil serves as the transmitter and main receiver. The upper (receiver only) coil lies 30cm above the bottom coil. Metallic objects interact with this transmitted field which induces secondary fields in the object. These secondary fields are detected by the receiver coils that are collocated with and above the transmit coil. An example EM61 MkII sensor mounted on a test platform is shown in Figure 2-1.

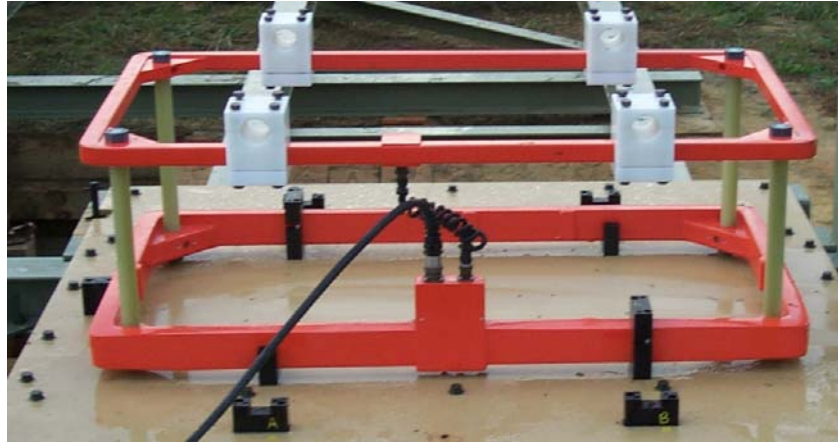


Figure 2-1 – Geonics EM61 MkII coils on a test platform

The transmitter pulse repetition rate is 75 Hz, corresponding to a base period of 13.333 milliseconds. The transmit pulse is 3.333 milliseconds long with a linear ramp off on the order of 100  $\mu$ s. The EM61 MkII electronics can be operated in one of two modes: 1) in 4-channel (“4”) mode with 4 time “gates” (216, 366, 660, and 1266  $\mu$ sec) for the bottom receiver coil or 2) in Differential mode, in which 3 time “gates” are measured from the bottom coil (216, 366, 660  $\mu$ sec), and one is measured from the top coil (at 660  $\mu$ sec). The transient decay voltage profile is sampled in the four time windows (for one or two receiver coils, as is appropriate) and analog integrated. The analog-integrated voltages are then sampled by the instrument’s analog-to-digital (A/D) converter. The analog integration step has a dynamic time response that both shifts and modifies the sensor’s response. The sensor’s step response is given by the manufacturer as:

$$e(t) = 1 - \frac{1}{\sqrt{1 - \tau^2}} \exp(-\tau \Omega t) \sin(\Omega t \sqrt{1 - \tau^2} + \arccos(\tau)),$$

where  $\Omega = 7.5$  rad/sec and  $\tau = 0.9$ .

The output of the pulsed-induction sensor can be sampled at rates up to 15 Hz, resulting in a data station spacing of approximately 10cm at normal walking speeds. The analog integrated voltage is sampled each time the electronics receives a trigger event. The trigger can either be a hardware pulse or a trigger character sent via RS-232 from the data acquisition software. Each

trigger event results in a binary data packet being sent via RS-232 to the data acquisition software. The details of the binary data packet format are given in the EM61 MkII documentation [2]. Briefly, the data packet contains the sampled voltages for the four time windows (or gates), a code indicating the applicable gain range for each time gate, a code indicating the sensor configuration (4/D), a measurement of the transmit current, and a measurement of the battery voltage. For compactness, the sampled voltages and the transmit current are expressed as dimensionless, integer numbers. The response in milliVolts for each time gate is converted from raw counts using the following formula:

$$RESPONSE = \frac{DATA \times 4.8333 \times 2}{RANGE}$$

The channel-specific *RANGE* values are 100, 10, or 1, as indicated in the Scale Factor parameter in the raw data packet. An additional scaling factor is required for the fourth channel when operating in Differential mode. If 1m x 1m coils or the –HH handheld variant are used, different scaling factors are required. This information is detailed in the EM61 MkII Operating Instructions [2].

Time references are provided by the combination of computer/software that triggers and collects the data packets. One important factor is that the transmit current changes in amplitude as the system battery discharges. The measured output voltages should be corrected for this changing current. The nominal transmit current for a standard EM61 MkII will be reported as a value of 3,000 and 1,800 for the –HH variant. The reported current is then used to normalize the voltage outputs to measurements made at the reference transmit current. Both the measured channel output voltages and the measured current are therefore potential sources of noise and error in the final sensor output.

Data are recorded using the vendor-provided Juniper Systems Allegro handheld data logger, or alternatively in a PC, using Geonics or custom PC software. For this demonstration, the EM61 MkII was operated in Differential mode and data was collected at 10 Hz using a custom software package written at NRL on a laptop computer. The facility for recording fiducials or ‘marks’ during the data collection process is provided for the purposes of co-registration data sets as necessary.

### **2.1.1.2 Geonics EM63**

The EM63, shown in Figure 2-2, operates using the same principles as the EM61 MkII, with two major differences, the coil geometry and the number of time gates recorded. The transmitter coil for the EM63 is 1m by 1m in dimension, normally operated at a height of approximately 40cm above the ground surface (wheel mode). The three receiver coils measure 0.5m x 0.5m, with the lowest mounted at the same height as the transmitter coil, and two other coils of the same size mounted at 30cm and 60cm above the lowest coil. Rather than recording a maximum of 4 time gates, the EM63 records data from 26 geometrically spaced time gates, from 180µs to 25ms.

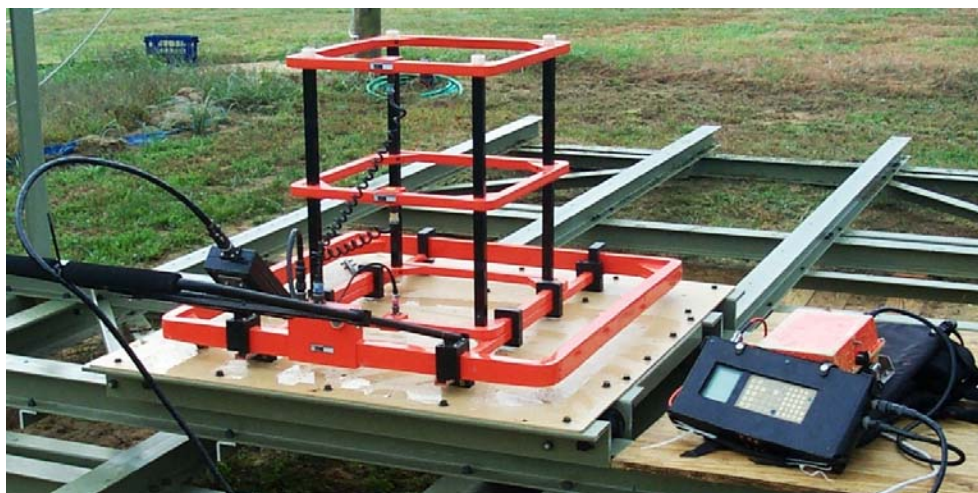


Figure 2-2 – Geonics EM63 with electronics and data logger, on a test platform

Data was collected using the integrated data logger field PC provided by Geonics at approximately 4 Hz and periodically downloaded for analysis.

### 2.1.1.3 Geophex GEM-3

The GEM-3 sensor (Geophex, Ltd.) is a frequency domain electromagnetic instrument, utilizing concentric coils mounted in a fiberglass sensor head. The sensor head is a disk, available in three sizes ranging from 40cm to 1m in diameter. The sensor used in this demonstration is shown in Figure 2-3. This unit was purchased in the Summer of 2006 (S/N: GEM3-0404-04). This sensor's coil head consists of a 40 cm diameter transmit coil with 12 turns, a 23 cm diameter bucking coil with 6 turns, and a 12 cm diameter receive coil with 100 turns. The counter-wound (with respect to the transmitter coil) bucking coil establishes a "magnetic cavity" around the receiver coil. To measure the strength of the transmit field, a reference coil (3 cm in diameter with 22 turns) is positioned between the transmit and bucking coils. The transmit current depends on the set of frequencies used and the battery's charge state; therefore the reference coil measures the transmit field strength directly and is used to convert the received signal in the relative units of parts-per-million (PPM) with respect to the transmitter.

Early versions of the GEM-3 instrument could measure single or stepping frequencies ranging from 30 Hz up to 24 kHz. Newer versions, including the one used in this demonstration, can transmit a composite waveform of up to 10 separate frequencies in a range of 30 Hz to 96 kHz. The sensor's base period is  $1/30^{\text{th}}$  of a second. All transmit frequencies have an integer number of periods within this base period. The sensor's A/D measures the receive coil and reference coil responses over the base period (6400 samples over  $1/30^{\text{th}}$  second). The receive coil output is convolved over one base period with the reference coil to calculate the in-phase and quadrature responses at the transmit frequencies in relative PPM units. This gives a maximum data rate of 30 samples per second. There are software options for averaging over a specified number of base periods. Most of the data presented in this report were averaged over three base periods for a data rate of 10 samples per second. The transmit frequencies are configured in software on the vendor-provided iPAQ mobile PC. For this demonstration, ten frequencies with roughly logarithmic spacing were collected (90, 150, 270, 570, 1230, 2610, 5430, 11430, 20010, 44370

Hz). For the additional measurements discussed in Section 3.7, a broader frequency range was explored (30, 90, 150, 450, 1170, 3930, 13590, 39030, 59010, and 90030 Hz).

Data are wirelessly transmitted (via Bluetooth technology) from the GEM-3 electronics to the iPAQ. The GEM-3 sensor is configured and data collection conducted using the WinGEMce software package (Geophex, Ltd.). In addition to the wireless data link to iPAQ, the sensor electronics package also has a nine-pin RS-232 port for direct PC control using the WinGEM software package. The internal battery was removed and a connector added for the use of external battery packs to extend measurement times. A rigid carbon-fiber pole was provided by the vendor for mounting the coil and electronics into a man-portable configuration but this was not used for most of these measurements.

The WinGEMCe software has a variety of features for further filtering, setting/incrementing survey line number, marking the data with fiducials, and applying frequency dependent phase corrections. Ferrite measurements are used to correct the phase shifted GEM-3 output and the built-in correction factors appear to be good to within a fraction of a percent. A new software feature is the ability to collect the entire A/D output over one base period and save it to a data file. This can be done in both passive (no transmit current) and active (transmit on at configured set of frequencies) modes. This feature was used to assess the effect of external noise on the GEM-3. The facility for recording fiducials, or ‘marks,’ during the data collection process is also provided in addition to the notion of survey line numbers for the purposes of data registration.



Figure 2-3 – Geophex GEM-3 sensor head (40cm diameter) and electronics

#### **2.1.1.4 Position and Orientation**

Position information was recorded using a real time kinematic (RTK) GPS system, updated at a rate of 10 Hz. GPS positions are expected to be accurate within ~ (1-2 cm H, 2-3 cm V) under optimal conditions. The GPS data was recorded using a custom logging software package written at NRL and a laptop computer. All navigation and sensor data are time-stamped with



Universal Coordinated Time (UTC) derived from the satellite clocks and recorded by the data acquisition computer. The facility for recording fiducials or ‘marks’ during the data collection process is provided for the purposes of data co-registration. Some testing conducted during this demonstration did not require the position of the instrument to be recorded, such as the static sensor noise testing. An inertial measurement unit (IMU, Crossbow VG300) was used to collect platform orientation (e.g. roll angle) information at update rates of up to 110 Hz. The same logging software is used to collect and timestamp the data. A higher-bandwidth IMU (Crossbow IMU 400) was used for the additional data collection conducted during the data analysis phase of this demonstration.

### **2.1.2 NRL Low Frequency Spectrum Analyzer**

Sources of external noise of interest to this study included those within the sensor bandwidth such as power lines and those of sufficient power that leakage into the sensor bandwidth is significant such as radar transmitters at airports. Each sensor design has a unique sensitivity to external noise based on factors such as detection bandwidth, pre-filtering, etc. Independent measurement of the external EM radiation impinging on the EMI sensors was made using a custom-build low-frequency spectrum analyzer based on a 0.5 m x 1.0 m EM61 receive coil (top). A custom-build solution was required because commercially-available spectrum analyzers do not have the capability of operating at the low frequencies required to match the operational window of the geophysical sensors being evaluated (DC – 100 kHz nominal).

The output terminals of the receive coil were directly connected to an analog input of a data acquisition card (National Instruments, DAQCard 6036E, 200 kS/sec). A custom data acquisition software package was developed to acquire data over a user-selectable frequency range (0.5 Hz – 100 kHz max). High resolution within the frequency range (0.19 Hz) is provided with a good dynamic range (75 – 100 dB). Data is recorded as a voltage time series. The prototype shown in Figure 2-4 is reasonably rugged. The cable breakout box (shown under the laptop) used is a generic one which could easily be further ruggedized and miniaturized by simply placing the breakout panel in a custom enclosure.

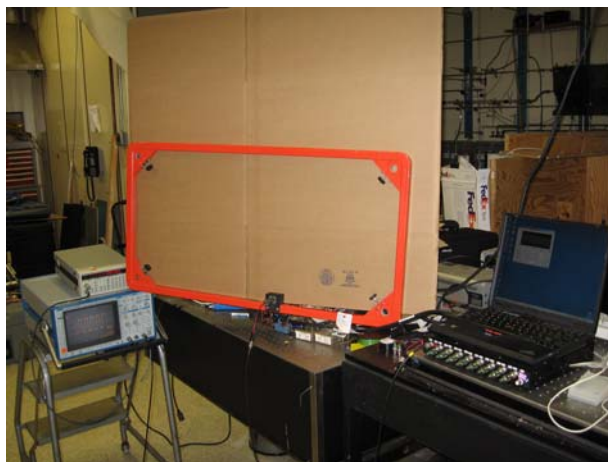


Figure 2-4 – NRL Low-Frequency Spectrum Analyzer

## **2.2 Data Collection and Preprocessing**

### **2.2.1 Inherent Sensor Noise**

Two types of measurements were made to characterize inherent sensor noise levels. First, a single specimen of each sensor type was turned on and allowed to warm up for at least an hour while data were recorded on the first day of the demonstration. To minimize any chance of inter-sensor interference, the sensors were placed at the different test locations (Boat Launch, Environmental Area, L-Range) within the demonstration site. Several sets of EM61 MkII electronics and coil sets were available during the demonstration and this measurement was repeated with different combinations as time allowed. These measurements helped determine the minimum warm-up time for each sensor type and the typical range of inherent sensor noise after the warm-up period.

The second type of measurements was designed to probe the variability between systems of the same sensor type. Several EM61 MkII electronics and coil sets were available for use and formed the test group for these measurements. A pair of fiberglass A-frame ladders was set 3.5m apart with a 2" x 10" dimensional lumber board spanning the distance and hanging over the far sides. The EM61 MkII coil set being tested was placed on the board with the long axis parallel to the board. The entire coil set was at least 1.76m above the ground to remove any ground response. The electronics backpack (with battery) and data logging laptop was placed on a plastic support at the length of the sensor cable. Data were collected using a NRL custom software package to collect the raw data stream from the sensor electronics, bypassing the standard EM61 MkII data logger. After an hour of warm-up data collection (recorded for the first type of measurements when possible), data were collected for approximately one hour. A 2" diameter chrome steel sphere was placed on the board 15 cm away from the coil in a circular depression to insure reproducible placement. The sphere was introduced for three cycles of 30 seconds in and 30 seconds out every ten minutes. The sphere was removed for the remaining seven minutes of each cycle. The EM61 MkII data were then corrected for transmit current and converted to mV using the manufacturer-recommended procedure.

### **2.2.2 Motion-Induced Noise**

The magnitude and effect of motion-induced noise in EMI sensor measurements was studied for a range of survey modes. The EM61 MkII and the GEM-3 EMI sensors and the RTK GPS / IMU telemetry combination described in Section 2.1.1.4 was installed on each platform evaluated. The platforms tested were a man-portable cart, the test tower moving down the rail system at both a slow and fast walking speed, and the MTADS EM trailer. These platforms are pictured in Figure 2-5, Figure 2-6, and Figure 2-7. Data were collected using the logging software package custom-built at NRL and a laptop computer. For the GEM-3 sensor, the sensor data were recorded using the provided iPAQ and combined after the fact using fiducial markers common to both data sets for timing alignment.



Figure 2-5 – Man-portable cart



Figure 2-6 – Rail system and test tower



Figure 2-7 – MTADS EM trailer



### 2.2.3 External Noise

Two of the available systems are capable of monitoring external noise sources, the NRL low frequency spectrum analyzer and the GEM-3. During the demonstration, the NRL system was used. Measurements were made with the GEM-3 during the data analysis period to further deconvolve the noise sources. The GEM-3 measurements are discussed in Section 3.7. A voltage time series was collected at the location of each traverse using the NRL low-frequency spectrum analyzer in each of three orthogonal directions, typically North, East, and pointed up. An example time series is shown in Figure 2-8. Four seconds of data are typically collected and can be stacked to improve the signal-to-noise ratio if required, at the sacrifice of the sub-Hertz response. The power spectral density (PSD) of the time series are then calculated and compared between orientations and locations. Example relative PSDs are shown in Figure 2-9. One common feature in all PSDs that was potentially an instrument artifact is a 2.2 millisecond (450Hz) pulse of 50kHz sine wave.

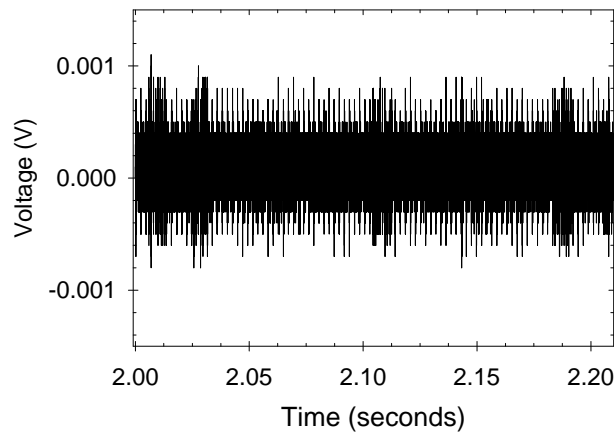


Figure 2-8 – Voltage time series from spectrum analyzer

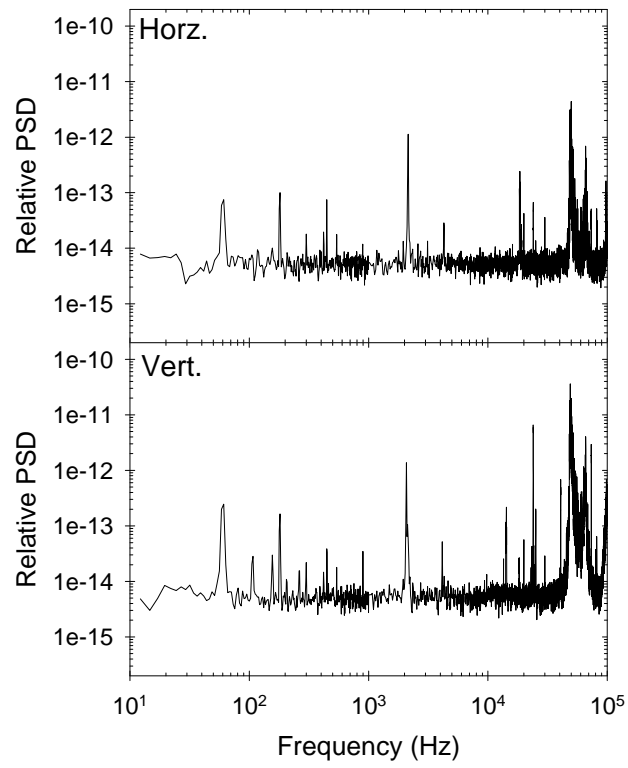


Figure 2-9 – Relative power spectral density results from horizontal and vertical orientation of external noise monitor

## 2.2.4 Geologic Response

Each sensor in turn was installed in the test tower / rail system shown in Figure 2-10. The rail system and test tower allow successive measurements to be made under reproducible conditions. The rail system provides positive positioning via a series of machined holes in the rail surface placed at 0.5m intervals on both rail tracks. The test tower contains matching locating pins to index the tower into position. The sensor platform on the test tower has 10 vertical positions spaced 0.25m apart for a total vertical range of 2.5m. The rail system and test tower are shown in Figure 2-10. At each station (position) along a traverse the output of the sensor was recorded in a cyclical pattern as shown in Figure 2-11. A height well outside the influence of geologic noise (roughly a meter and a half) was used as a reference standard. Measurements were then made cycling through the lower stations with the top station as a continued reference, reaching the lowest position which is at, or below, normal survey height (~25 to 30 cm). Measurements made at the reference position were used to apply a simple polynomial correction to the data to remove the effects of sensor drift. These measurements are repeated along portions of the traverse at intervals to capture the geological response on the length scales of interest for UXO (5 stations each, 0.5m spacing). The GEM-3 sensor is used initially for these measurements. An example of the typical results is shown in Figure 2-12 where the in-phase and quadrature response from the GEM-3 are shown for two frequencies as a function of sensor height at the Environmental Area. The in-phase profile appears to be frequency independent while the quadrature profile is frequency dependent. The quadrature ground effect is stronger at higher frequencies and the shape of the profile appears to depend on frequency.



Figure 2-10 – Rail system deployed at Boat Launch area, shown with Geonics EM-63 in position

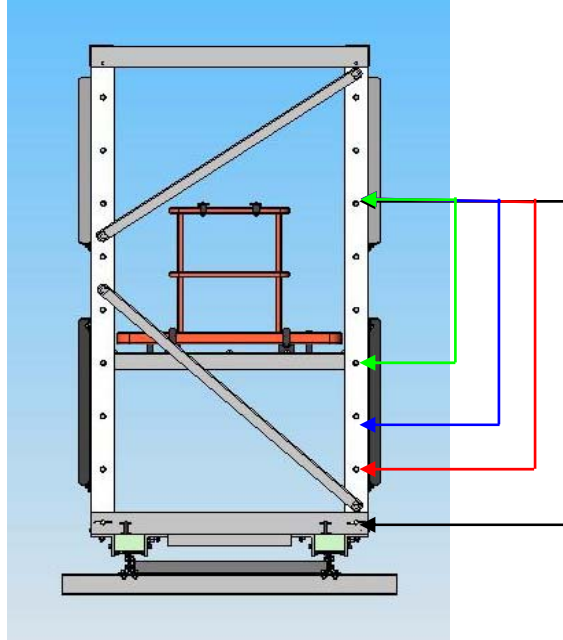


Figure 2-11 – Data collection scheme used at individual stations on the rail system. See text for further description.

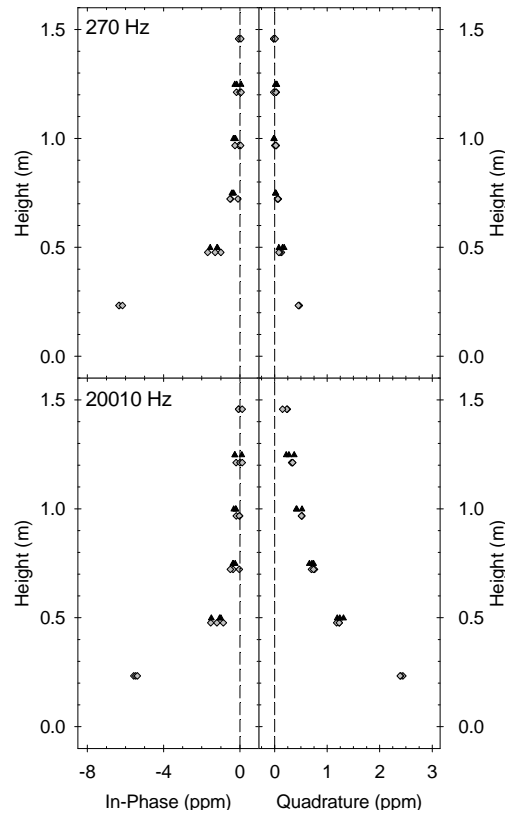


Figure 2-12 – GEM-3 ground response results for the Environmental Area

It was the case at Blossom Point that the low-frequency response was quite small for the GEM-3 and spot measurements with the EM63 yielded no measurable ground response. In Figure 2-13, a vertical profile of the ground response as measured using the EM63 is shown for the first time gate, 177  $\mu$ s, which roughly corresponds to a GEM frequency of 1 kHz. Later time gates correspond to even lower frequencies. No ground response was evident in the data.

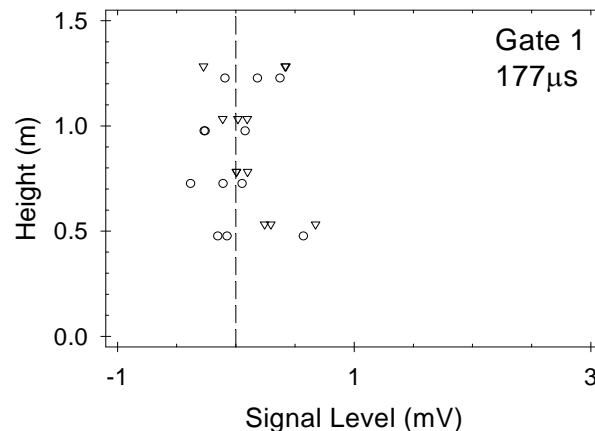


Figure 2-13 – EM63 time gate 1 response at Boat Launch

One station from each portion of the traverse was selected for further measurements once usage of the rail system at that location was complete. The test tower is placed on the ground and the measurement cycle repeated. In this case, the reference measurement may not have been high enough to be completely outside the ground response but could be referenced to the data collected on the rail system.

At the location of each traverse the magnetic susceptibility and moisture content were measured to correlate with the EMI sensor measurements. The exact measurement interval varied but typically captured 2-3 measurements along each traverse for moisture content and the magnetic susceptibility measurements were made every 0.75m for the Environmental and Boat Launch Areas (30m transects) and every 1m for the L-Range Area (100m transects). The Bartington instrument exhibits a drift rate which must be compensated for due to the long time frame (30 minutes to 1 hour) required to complete a measurement cycle but otherwise provides a direct reading of the magnetic susceptibility. The moisture content measurements are used without modification.

### 2.2.5 Location Uncertainties

The primary instrumentation for these measurements was our RTK GPS system with the IMU and the EMI sensors providing additional reference information. In an open field with good sky view, carefully measured GPS sensor locations can be as precise as 1-2 cm. A series of measurements of GPS error in conditions ranging from open fields to at the tree line were made. The rail system and test tower, described in Section 2.2.4, was used in which we could translate the GPS antenna and other sensors precisely along a known, reproducible path as we recorded the data. We performed these measurements during a variety of GPS constellation conditions

and at each location. Measurements included static measurements at each station down the rail system with the test tower pinned in place and dynamic traverses along the rail system with the IMU and EMI sensors active. Measurements made using the man-portable cart and MTADS trailer provided similar data for the effects of sensor platform orientation on EMI surveys. All GPS data were collected as National Marine Electronics Association (NMEA) sentences from the receiver and converted using standard tools from the Latitude / Longitude / true north reference frame to the UTM Easting / Northing / grid north reference frame. IMU outputs were parsed directly from the unit's binary output format and recorded without modification. The EMI sensor data were collected and processed as discussed above.

### **2.3 Data Analysis**

The data analysis methods employed for this demonstration are developed and discussed in the later sections of Section 3. The discussion is deferred to those sections.

### **2.4 Previous Testing of the Technology**

Numerous tests have been performed with the Geonics and Geophex instruments for detection and characterization of unexploded ordnance. Numerous projects sponsored by SERDP, ESTCP, and other government agencies have explored the relative value of these instruments in detection and discrimination scenarios. There are several lines of ongoing research to thoroughly characterize the potential performance of EMI sensors for the detection and discrimination of UXO. ESTCP Project MM-0506 is investigating the repeatability of EMI and total field magnetometry (TFM) detection of currently-fielded sensor systems. The effort is focused on the monitoring the operating characteristics of commonly used EMI and TFM units and collecting data over five separate standardized items under identical conditions. Projects such as the ESTCP Overlapping Signatures Data Collection (by both NRL and ERDC) have focused on characterizing the response of these sensors to standard UXO and clutter items and combinations thereof and how to extract the UXO signature from the clutter signatures. Projects such as SERDP MM-1313 have inventoried the inherent variability with a given ordnance class based on a large number of recovered items from remediation sites.

This project investigated a different aspect of the application of these instruments, by focusing on the quantification of the sources and magnitudes of background signal and noise for EMI UXO measurements, and the practical limits placed on the use of classification algorithms by this noise.

### **2.5 Factors Affecting Cost and Performance**

Costs for the Blossom Point demonstration consisted primarily of labor costs. Lodging and per diem costs for the staff were minimal as the demonstration site is local to most of the staff. Labor costs were summarized in the Final Full Proposal. Equipment costs were limited, as NRL already has acquired most of the equipment to be tested. Equipment rental fees applied to the soils testing equipment which was returned after the initial measurements were made. Travel costs were low for this demonstration, again due to the proximity of the offices of all participants.

Factors negatively affecting performance included weather conditions, mostly from the extreme heat and humidity. Scheduling conflicts for use of Blossom Point facilities was minimal with issues only on the L-Range. Even with an overlapping usage of the L-Range, impact on the testing schedule was minimal. The exact dates of the demonstration had some effect on the GPS testing (location uncertainty), from leaf canopy in the deciduous forest at Blossom Point. Winter and early spring offer very different conditions than those seen after the appearance of leaves. Also GPS satellite geometries are a continuously evolving reality.

## **2.6 Advantages and Limitations of the Technology**

Ultimately, the advantage of understanding the magnitudes and sources of noise for EMI sensor, the components of the error budget, and using this knowledge will be the ability to characterize a site quickly and identify what technologies can be successfully implemented for the detection and discrimination of UXO. A successful choice should lead to a reduction in the number of false positives, and therefore the costs of remediation in UXO contaminated areas. By conducting these demonstrations in a variety of environments, one could obtain information applicable to UXO sites in similar terrains and noise environments across the continental United States.

# **3. Demonstration Design**

## **3.1 Performance Objectives**

This demonstration consisted of testing the three EMI instruments (EM61 MkII, EM63, GEM-3) at three different locations at Blossom Point. Site conditions at each location during the demonstration were documented in writing, with photographs, and with standard geophysical instruments (magnetic susceptibility and moisture content). Data were collected with the EMI instruments, a GPS system, an IMU, and with a spectrum analyzer.

In the following paragraphs, we describe in more detail the predominant noise sources in an EMI survey.

**Inherent Sensor Noise:** Any actual EMI sensor contains a certain level of inherent noise. This noise is manifest as the response values reported by an instrument that cannot be accounted for by any outside source. Difficult to remove through post-processing techniques, inherent noise must be expected and accounted for during all EMI surveys. The results of these measurements, while only valuable to the sensor design community as a benchmark against which to measure their development efforts, can be expected to be very valuable to those developing classification algorithms and systems.

**Motion-Induced Noise:** The role of motion-induced noise in the degradation of UXO classification ability has been well documented by us and others [3]. The two facets of what is commonly understood as motion-induced noise are noise resulting from motion of the receive coil of the sensor in the Earth's field [4] and the variation in the observed signal resulting from orientation changes of the sensor as it bounces and twists over rough ground.

**External Noise:** External noise results from the presence of ambient EM signals that are detectable by the sensor. Typical sources include those within the sensor bandwidth such as power lines and those of sufficient power that leakage into the sensor bandwidth is significant such as with radar transmitters at airports. External noise has also been observed as a result of GPS equipment, data loggers, and batteries that are placed too close to the sensor during data collection. Each sensor design will have a unique sensitivity to external noise based on factors such as detection bandwidth, pre-filtering, etc.

**Geologic Response:** Non-metallic features in the subsurface have been documented as causing anomalous response in EMI instruments. While more correctly called background rather than noise as it is defined above, variations in this background response that occur on the scale length of UXO targets obscure the true target anomaly and complicate the discrimination decision. The geologic responses found in areas containing strongly ferromagnetic soils or bedrock have been well documented [5]. Fresh basaltic bedrock, like that found in Hawaii, appears to have the greatest impact on EM data, though similar responses were recently observed in iron-rich soils in northern California

**Location Uncertainties:** Even in the absence of any background variation or sensor noise, sensor location uncertainties can degrade the discrimination performance of a sensor by degrading the quality of fitted parameter estimation of the survey data. In the majority of the discrimination approaches under investigation today, the resultant feature vectors are the inputs to the classification scheme. Increased uncertainty in these parameters directly translates into decreased classification performance.

## **3.2 Test Site Selection**

Blossom Point was selected by NRL as the first demonstration site. It provides the obvious benefit of being where NRL's equipment, tools, offices, etc. are located so that we could efficiently develop our procedures and standards for testing. Beyond that, however, it provides many of the features we would look for in a "typical" survey site in the Eastern United States. A variety of areas are available ranging from open field areas, heavily treed sites, to transition zones. One might expect the geologic interference to be at a minimum at a site such as this but we have shown in previous testing for other programs that there is a surprising amount of short-scale geologic variation present even at Blossom Point. In this, it is analogous to what we have observed at the Standardized UXO Test Site at Aberdeen Proving Ground, another prototypical Eastern site. Finally, the Blossom Point Site is an active test range and is adjacent to the NRL Tracking Station which houses a number of communications facilities, providing a meaningful measurement of external noise.

### **3.2.1 Test Site History / Characteristics**

The Army Research Laboratory's Blossom Point Research Facility is comprised of 1,600 acres, approximately 50 miles south of Washington DC, in rural Charles County, Maryland, Figure 3-1. The facility is located on Cedar Point Neck, between the Nanjemoy Creek and the Port Tobacco River on the northern shore of the Potomac River. Open, grassy fields, as well as areas of deciduous and mixed deciduous and conifer forest are found on the property. Low elevation,



swampy areas are present in the central and eastern portions of the property, and along the southern edge, adjacent to the Potomac River, Figure 3-2.

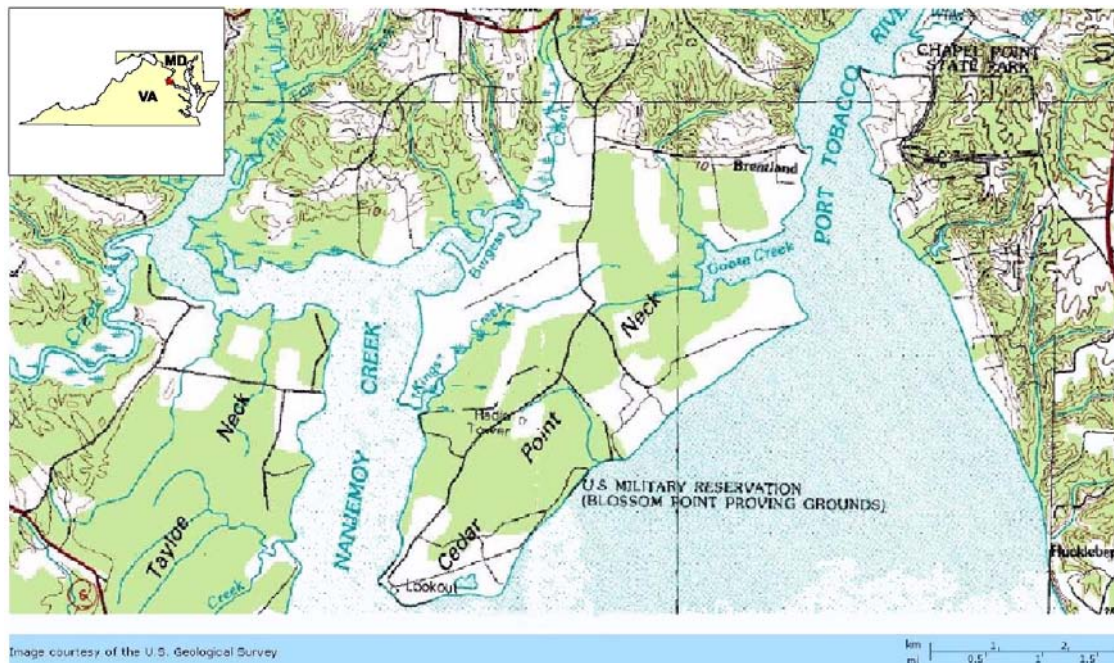


Figure 3-1 – Location of Army Research Laboratory Blossom Point Facility

### 3.2.2 Climate

Blossom Point has a climate typical of the Mid-Atlantic States, with moderately cold, damp winters and hot, humid summers. Temperature and precipitation for nearby LaPlata, MD (10.5 miles to the NE) are presented in Figure 3-3, from the Southeast Regional Climate Center.

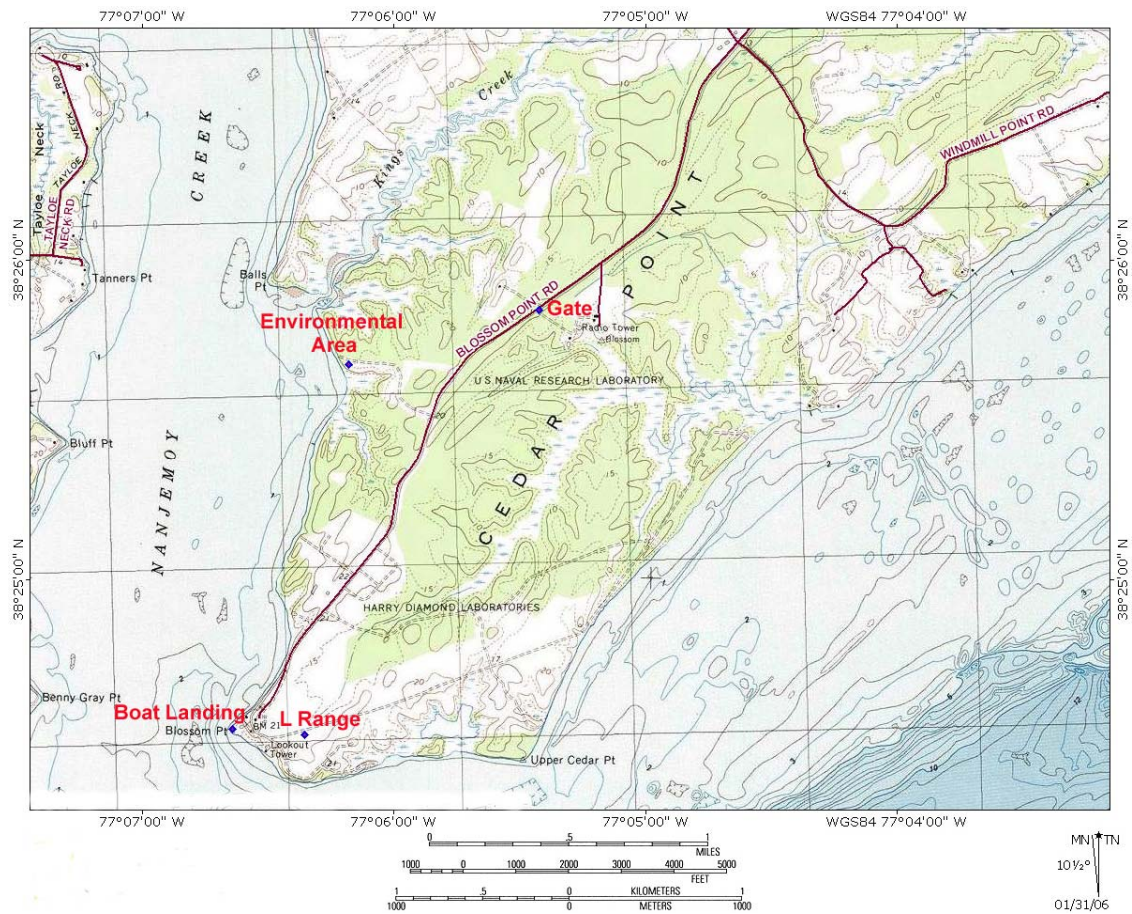


Figure 3-2 – Topographic Map of Blossom Point Research Facility, showing locations of selected EMI Noise Test sites

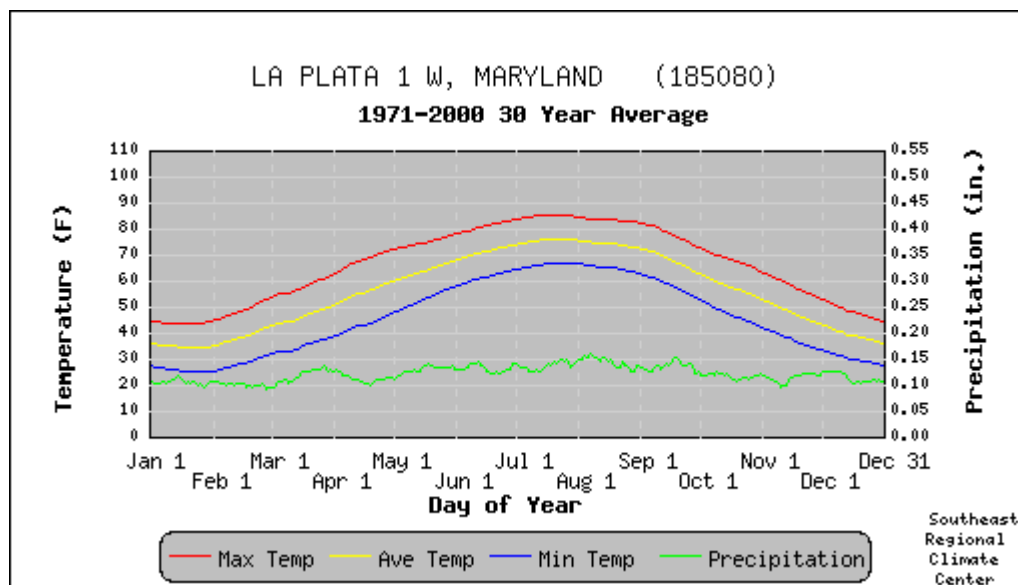


Figure 3-3 – Climate data for LaPlata, MD



### 3.2.3 Geology

Charles County, MD is situated within the Coastal Plain Province. This province is underlain by an eastward thickening wedge of unconsolidated marine sediments including gravel, sand, silt, and clay. Cedar Neck Point is mapped in the 1989 Maryland Geological Survey Charles County Geologic Map (see Figure 3-4) almost entirely in the Upper Pleistocene-aged Maryland Point Formation (Qm). The Maryland Point Formation is described as fine to coarse grained sand, well to poorly sorted in the upper third, with poorly sorted silty clay in the lower part, with a pebbly sand at the base. [6]

Two other mapped units occur on Cedar Point Neck, Qk, and Qh, each occupying small areas. On Cedar Point Neck, the Upper Pleistocene-aged Kent Island Formation (Qk) occurs only on a peninsula south of Goose Creek. This unit overlies the Maryland Point Formation, and consists of fine to medium grained, moderate to poorly sorted silty sand. Minor silty to sandy clay is also present. The most recent mapped unit is Holocene deposits, undivided, which occur only in low lying areas adjacent to swamps and drainages at the Blossom Point Research Facility. These deposits include poorly sorted sand and gravel, as well as well sorted sand, silt and clay.

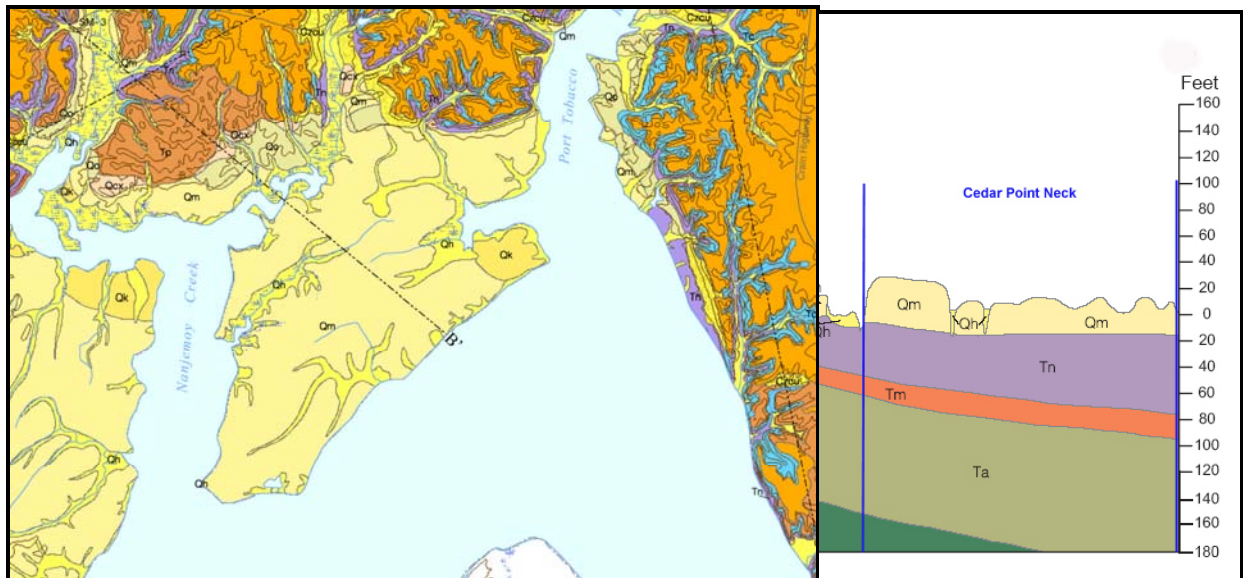


Figure 3-4 – Geologic Map and Cross Section (McCartan, 1989) showing Cedar Point Neck

The cross section presented in Figure 3-4 shows a maximum thickness of the Maryland Point Formation on Cedar Point Neck of approximately 40 feet. The formation is absent where the cross section traverses two small streams, filled with Holocene sediments.

Geologic responses observed in electromagnetic surveys are often caused by magnetic minerals, primarily magnetite and maghemite. These minerals are very likely present in the marine sediments at Blossom Point, though it is expected that they are generally dispersed, and that concentrations high enough to affect EM response are limited in area.

Two soil properties, moisture content and magnetic susceptibility were measured at the test sites surveyed in Blossom Point using traditional instruments. Moisture content was measured using

an ESI soil moisture probe at locations along the test lanes. Magnetic susceptibility data was collected using a Bartington MS2/D instrument and the results are described in Section 3.6. The conductivity parameters for the three test sites were extracted from the GEM-3 sensor data, as described in Section 3.7.

### **3.2.4 Test Locations within Blossom Point**

Three selected locations at Blossom Point were used to replicate conditions typical of live UXO sites located in the Eastern US, the Boat Launch, the Environmental Area, and a selected portion of the L-Range, Figure 3-2. At each of the sites, described below, a series of measurements were made as described in Section 2.2 including data collection with the EMI instruments at various heights, the use of the rails system / test tower, traverses with various sensor combinations, and standard geophysical measurements of the soil properties. The specific tests conducted are described in Sections 2.2 and 3.5.

#### **3.2.4.1 Environmental Area**

A transitional area leading into dense woods with a thick foliage cover was used as one test site at Blossom Point and is shown in Figure 3-5. The encroaching tree line did cause degradation of the GPS fix quality which proved useful for examining the effects of GPS satellite constellation geometry.



Figure 3-5 – Environmental Area, view to the East

#### **3.2.4.2 Boat Launch**

The Boat Launch Area was a test location at the southern tip of the Blossom Point facility with a low elevation and corresponding saturated soils. The location is also known as the former Munitions Storage Area. This area was selected for this demonstration and is shown in Figure

3-6. The effects of the wetter soils were compared to unsaturated sediments in the other test locations. This site offered open, unobstructed sky view, for ideal GPS satellite reception. Due to the low elevation, the Boat Launch site experienced the most variation on soil moisture during the course of the demonstration. After an episode of rain on site, the ground became saturated with water to the point that standing water was observed. See Section 3.7.3 for a discussion of the effect of soil moisture on the data collected.



Figure 3-6 – Boat Landing Area, view to the southwest

### **3.2.4.3 L Range**

A site was selected on the L Range, an active range, in an area which generally did not interfere with the ongoing usage of the range. The site, shown in Figure 3-7, exhibited a background typical for a former firing range, with buried ordnance and ordnance scrap underlying the survey area. The surface had been cleared of any munitions or debris, and the vegetation (grass) was mowed prior to our demonstration.



Figure 3-7 – Active Range Test Location, L-Range, view to the East

### **3.3 Present Operations**

The Army Research Laboratory Blossom Point Facility is classified as a Range, and is closed to the public. Testing occurs at the facility throughout the year, but it sees heaviest use during the spring, summer, and fall months. The NRL Tracking Station is located in the northern portion of the property and provides a source of ambient cultural noise. NRL maintains their Baseline Ordnance Classification Test Site at Blossom Point, constructed in 2000 in an area known as Steivers Field [7].

### **3.4 Pre-Demonstration Testing and Analysis**

Glenn Harbaugh, along with Dan Steinhurst and Mark Howard, visited locations at Blossom Point on January 24, 2006 to select the test areas for the wooded, low elevation, and active range test sites at Blossom Point. Construction of the rail system and test tower was completed prior to the demonstration. Mobilization of equipment was not necessary for most of the instruments to be tested, as they are stored at Blossom Point. All logistics and facilities needed for the demonstration were already in place.

### **3.5 Testing and Evaluation Plan**

#### **3.5.1 Demonstration Set-Up and Start-Ups**

Mobilization of team members required only a drive of one to 3 hours to reach Blossom Point.

#### **3.5.2 Period of Operation**

The Demonstration at Blossom Point commenced on July 31, 2006. The final schedule for this survey is detailed in Table 3-1. All dates have been updated from the original planned times to reflect the actual schedule. As this demonstration was locally located, the schedule was extended

to allow for flexibility in testing and diagnosis of emergent issues while the test methodology was refined.

Table 3-1 – Final Schedule for the EMI Noise Demonstration at Blossom Point.

Date	Planned Action
January 24, 2006	Selection of test areas at Blossom Point
July, 2006	Completion of test rails and instrument platform
July 31, 2006	Begin field work at Blossom Point
September 14, 2006	Complete field work at Blossom Point
July 31, 2006 – May, 2008	Data analysis of demonstration data
October, 2008	Draft Demonstration Report submitted
February, 2009	Revised Demonstration Report submitted

### 3.5.3 Scope of Demonstration

Three small areas (each containing < 0.2 Ha) were used in the Blossom Point Demonstration. Actual survey coverage was even smaller, with the rail system survey areas limited to a one meter wide strip along a 30m long line.

### 3.5.4 Residuals Handling

No range scrap, munitions or chemicals were handled during this Demonstration.

### 3.5.5 GPS Control Monuments

A network of four GPS first-order control points was established for use in the NRL Baseline Ordnance Classification Test Site. These locations remain as possible base station monuments for the RTK GPS system. Coordinates for the points are listed below in Table 3-2. NRL MTR is the monument nearest the MTADS Test Field and the one typically used. This control monument was used exclusively during this demonstration.

Table 3-2 – Coordinates of First-Order Control Points at Blossom Point.

Station	Latitude	Longitude	Elevation (m)	Ellipsoidal Height (m)
BPPG 1	38° 24' 43.96335" N	77° 06' 18.24048" W	4.882	-28.053
BPPG 5	38° 24' 34.76902" N	77° 06' 09.16849" W	5.889	-27.058
BPPG 6	38° 24' 31.91542" N	77° 06' 21.25664" W	5.111	-27.829
NRL MTR	38° 24' 01.21759" N	77° 06' 10.31694" W	6.317	-26.615

### **3.5.6 Operational Parameters for the Technology**

The relevant operational parameters for each technology and their overall impact on the detection and discrimination of UXO by EMI instruments is presented in the remaining subsections (Sections 3.6 - 3.9) of this Section of this report.

### **3.5.7 Demobilization**

Staff for the project de-mobilized on September 14, 2006, the last day of data collection. Most equipment remains at Blossom Point, for use in other projects or for storage. Rental equipment was shipped back following data collection in August 2006.

### **3.5.8 Health and Safety Plan (HASP)**

The Health and Safety Plan for this project followed the United States Army Blossom Point Research Facility Standard Operating Procedures for Range Operations. The plan is outlined in Appendix A of this Demonstration Plan.

## **3.6 Characterization of the Soil by Standard Techniques**

At each location, characteristics of the soils, including moisture content, magnetic susceptibility, and conductivity were measured. Soil moisture content was measured at three stations within each test location. Magnetic susceptibility was measured by recording values at intervals, of approximately 0.75m for the Environmental and Boat Launch Areas and 1.0m for the L-Range Area, along the same path as the test rails. Soil conductivity measurements were extracted from the GEM-3 data. More detail is provided below in Section 3.7.3.

### **3.6.1 Soil Moisture**

At each station, the soil moisture content was measured simultaneously at five depths (7.5, 22.5, 37.5, 60, and 90 cm). Soil moisture influences conductivity, which is expected to have a greater impact on frequency domain EMI instruments than on time domain instruments. Soil moisture was measured using a “Moisture Point” probe and electronics from Environmental Sensors Inc. (ESI). The results for the Boat Launch Area collected on 07/31/2006 are given in Table 3-3. The results for the Environmental Area and the L-Range are given in Table 3-4 and Table 3-5 and were collected on July 31 and August 03, 2006, respectively. The variation between the locations was found to be larger than that between individual stations. To illustrate this, the results are presented in Figure 3-8 where an average value for each depth / location pair is shown with the range expressed as a horizontal error bar. As one might expect, the moisture content tracked with elevation above the river, with the highest content for the Boat Launch, lower at the L-Range, and a minimum at the Environmental Area. Interestingly, for depths of less than 40 cm, the moisture content was the same for all areas as shown in Figure 3-8.



Table 3-3 – Moisture content measurements for the Boat Launch Area

Center Depth (cm)	Measurement #1	Measurement #2	Measurement #3
Center of traverse			
7.5	7.4%	7.4%	8.5%
22.5	11.3%	10.7%	11.8%
37.5	27.9%	28.0%	28.2%
60	34.6%	34.5%	34.7%
90	34.6%	34.2%	34.2%
West end of traverse			
7.5	-	0.8%	0.6%
22.5	4.8%	4.6%	4.8%
37.5	13.3%	13.6%	16.2%
60	34.2%	34.2%	33.8%
90	34.4%	34.4%	34.4%
East end of traverse			
7.5	7.7%	7.1%	7.7%
22.5	9.6%	12.4%	12.1%
37.5	36.7%	36.8%	36.8%
60	35.7%	35.4%	35.3%
90	40.6%	40.7%	41.0%
Summary			
	Avg	Max	Min
7.5	5.9%	8.5%	0.6%
22.5	9.1%	12.4%	4.6%
37.5	26.4%	36.8%	13.3%
60	34.7%	35.7%	33.8%
90	36.5%	41.0%	34.2%

Table 3-4 – Moisture content measurements for the Environmental Area

Center Depth (cm)	Measurement #1	Measurement #2	Measurement #3
East end of traverse			
7.5	10.2%	9.9%	9.9%
22.5	13.8%	13.5%	13.2%
37.5	21.1%	21.5%	21.5%
60	1.6%	17.8%	17.8%
90	25.8%	26.0%	25.9%
West end of traverse			
7.5	13.1%	13.1%	13.6%
22.5	12.4%	12.4%	12.4%
37.5	15.0%	15.0%	15.0%
60	19.6%	19.2%	19.7%
90	27.4%	28.1%	27.4%
Summary			
	Avg	Max	Min
7.5	11.6%	13.6%	9.9%
22.5	13.0%	13.8%	12.4%
37.5	18.2%	21.5%	15.0%
60	16.0%	19.7%	1.6%
90	26.8%	28.1%	25.8%

Table 3-5 – Moisture content measurements for the L-Range Area

Center Depth (cm)	Measurement #1	Measurement #2	Measurement #3
West end of southern traverse			
7.5	5.7%	6.5%	6.0%
22.5	12.1%	12.1%	11.8%
37.5	23.4%	23.1%	23.4%
60	29.5%	29.3%	29.2%
90	31.2%	31.0%	31.3%
150 ft. east of first point			
	6.2%	6.5%	6.8%
	12.1%	12.1%	12.4%
	11.1%	11.4%	11.3%
	26.5%	26.8%	26.8%
	28.0%	28.3%	28.3%
300 feet east of first point			
	6.2%	6.5%	6.8%
	12.1%	12.1%	12.4%
	11.1%	11.4%	11.3%
	26.5%	26.8%	26.8%
	28.0%	28.3%	28.3%
Summary			
	Avg	Max	Min
	6.6%	7.1%	6.2%
	10.5%	13.8%	5.7%
	16.1%	25.3%	11.1%
	26.3%	29.1%	23.1%
	28.8%	29.5%	28.0%

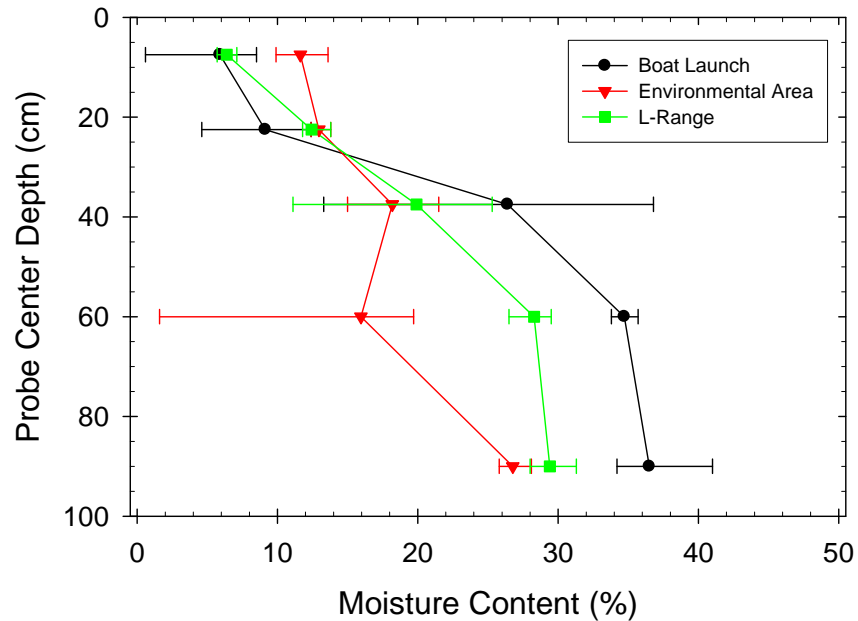


Figure 3-8 – Moisture content profiles for the Boat Launch, Environmental, and L-Range areas

### 3.6.2 Magnetic susceptibility of soils

Magnetic minerals (especially magnetite and maghemite) in soil or shallow bedrock may have pronounced effects on EMI measurements. The Bartington MS2 Magnetic Susceptibility system is designed to measure soil magnetic susceptibility in the field. For this demonstration, we used the Bartington MS2D search loop, 185mm in diameter, to measure differences in magnetic susceptibility of the soils underlying the traverse at each test location. Measurements were made at 0.75m intervals along the measurement traverse path for the Environmental and Boat Launch Areas. In the case of the L-Range measurements, measurements were made along two 92-meter long paths placed within a few meters of the rail system traverse at 1m intervals. The results are shown in Figure 3-9, Figure 3-10, and Figure 3-11.

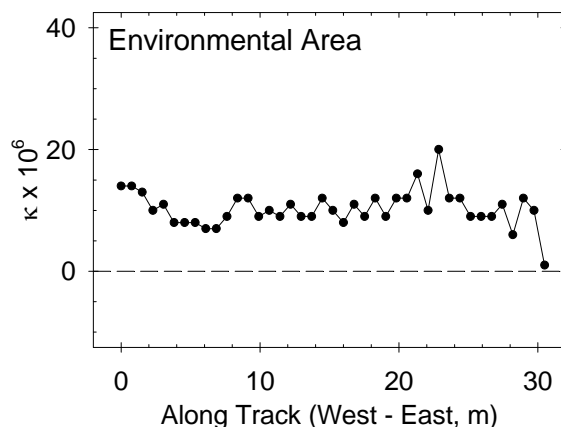


Figure 3-9 – Magnetic susceptibility profile for the Environmental Area

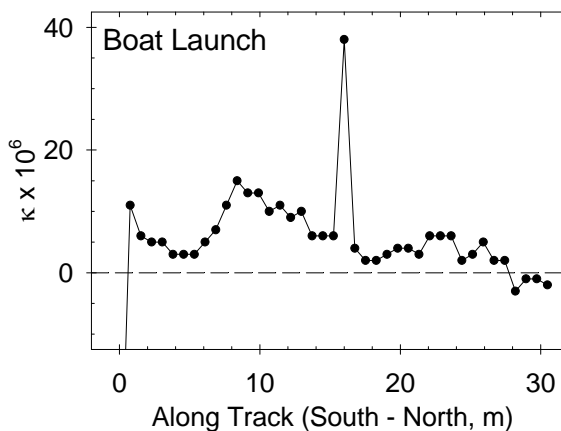


Figure 3-10 – Magnetic susceptibility profile for the Boat Launch Area

In general the magnetic susceptibility of the soils at Blossom Point is quite low, on the order of  $5 \times 10^{-6} \kappa$  (cgs units). For reference, pure magnetite has a  $\kappa$  of 1 and the  $\kappa$  for solid iron can be on the order of 100 in the same units. The Bartington instrument exhibited a manufacturer-acknowledged a drift rate that is particularly observable in Figure 3-11 due to the length of time

involved in the measurement series (half an hour or so). The manufacturer provides enhanced data collection procedures (frequent, intermediate zeroing of instrument in air) and data-processing techniques for removing this drift which would be more rigorously applied in future demonstrations.

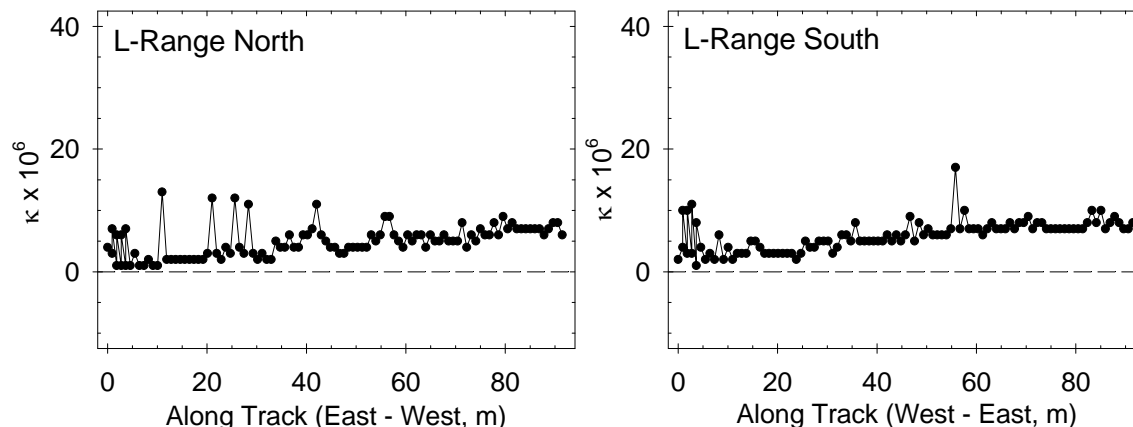


Figure 3-11 – Magnetic susceptibility profile for the L-Range traverses

### 3.7 Analysis of the GEM-3 Data

This section presents the analysis of the data collected for the GEM-3 frequency-domain EMI geophysical instrument. A significant amount of additional data collection was conducted with the GEM-3 sensor after the field work was completed. These measurements were made based on issues which arose during the data analysis effort. These additional measurements are presented in the course of the following analyses. For the measurements made after the conclusion of the main demonstration, LabView code written by SAIC was used to collect the data in a manner similar to that of the NRL software. (NOTE: Time synchronization of the GEM with the other two data sets was not possible with the iPAQ GEM software. Fiducials and trial and error had to be used to synchronize the GEM with the recorded GPS and IMU data.)

#### 3.7.1 External Noise

To assess the external noise picked up by the GEM-3's receiver coil, data were collected with the GEM-3 sensor in its monitoring mode. This mode dumps out the receive coil voltage measured by the A/D system over one 1/30<sup>th</sup> of a second base period (6,400 samples collected at 192,000 samples per second). When in passive mode, the transmitter is turned off; and when in active mode, the transmitter is turned on. These data were collected with the GEM-3 roughly 2 meters above the ground. Data were taken with the GEM-3 coil in three orthogonal orientations: horizontal, on edge facing north-south, and on edge facing east-west. In each orientation, data were collected while passive, while active with 10 transmit frequencies, and while active with three transmit frequencies.

Relative power spectra from these data sets are shown in Figure 3-12. The top three graphs are the results from data collected in the passive mode. It clearly shows 60 Hz and a number of harmonics dominating the output. After this, there are some broad spectral peaks in the 10 to 100 kHz region. When the coil was oriented on edge, it picked up VLF transmission lines at 24 and

24.8 kHz. Active spectra with ten transmit frequencies are shown in the middle plots and three transmit frequencies in the lower plots. The spectra are dominated by the transmit frequencies. While the receive coil is located in a magnetic cavity created by the bucking coil, the primary field is not completely canceled. These peaks plus the general active background are much greater in amplitude than the passive spectra; only the lower 60 Hz harmonics appear to rival the active noise. Curiously, the general active background is similar whether there are three or ten transmit frequencies. Based on these results, external noise is not a dominant factor for the GEM-3 sensor.

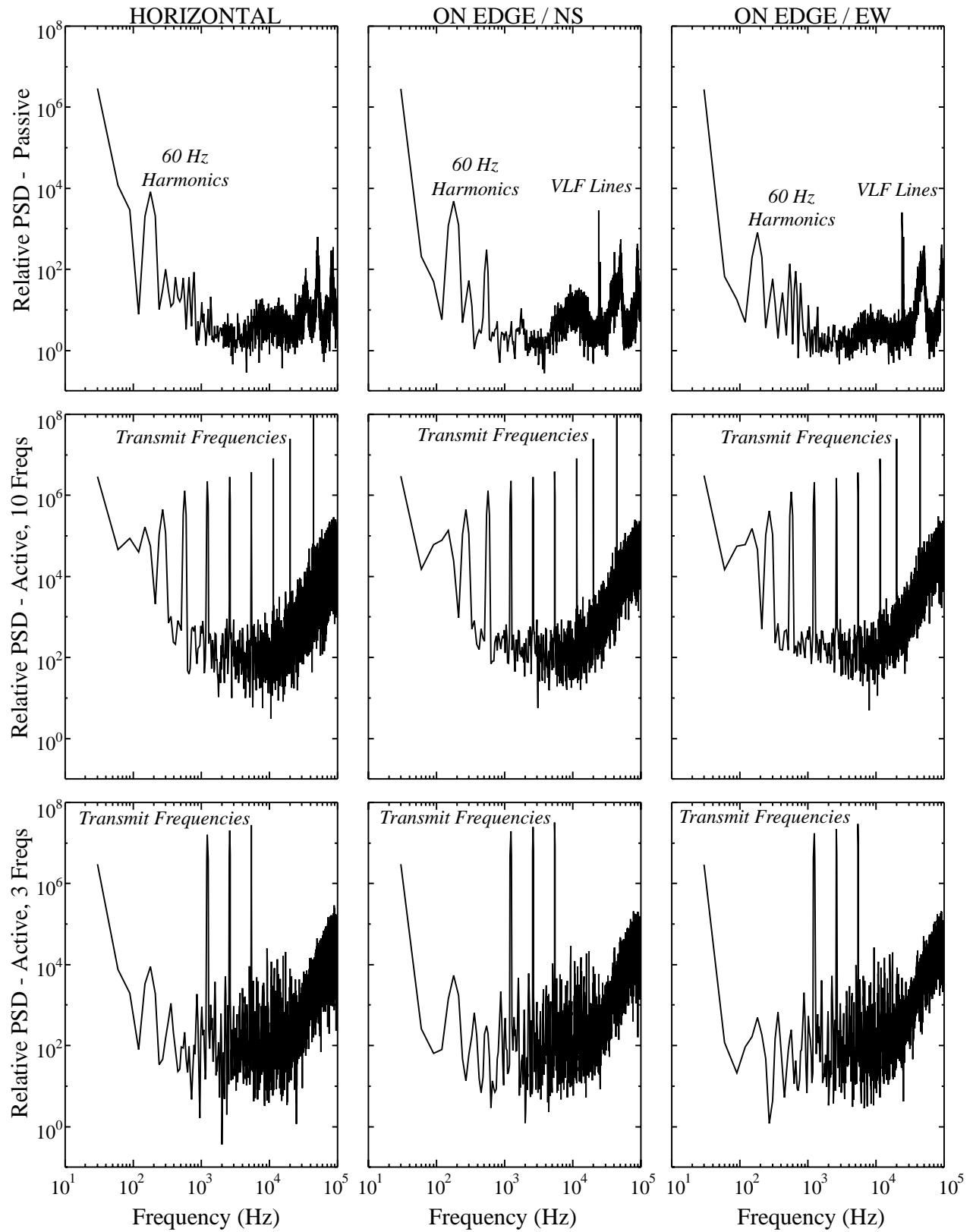


Figure 3-12 – Power Spectra Results for the GEM-3 Sensor in both Passive and Active Monitoring Modes

### 3.7.2 Inherent Noise

To measure the basic electronic noise levels of the GEM-3, the sensor was placed stationary on a test stand, in a field far removed from any radiating object. After warming the sensor up for 15 to 30 minutes, data was collected for another 30 minutes. The GEM-3 was run with ten transmit frequencies from 30 to 90,030 Hz. The sensor was set to average over three base periods; so, data were collected at ten samples per second. Time rasters and averaged power spectra are plotted for all ten frequencies in Figure 3-13 and Figure 3-14. In-phase is shown in black and quadrature in red. At each transmit frequency, there is a basic white noise level for both in-phase and quadrature. The white spectra roll off above 1-2 Hz because of the base period averaging. On time scales greater than 10 seconds, there is significant drift in the in-phase signal. This is possibly due to changing conditions in the imperfectly bucked primary field. At high frequencies, this drift is present in the quadrature signal as well. Figure 3-15 plots the white noise floor as a function of transmit frequency. From these results, the optimal transmit range for the GEM-3 is from 1 to 10 kHz.

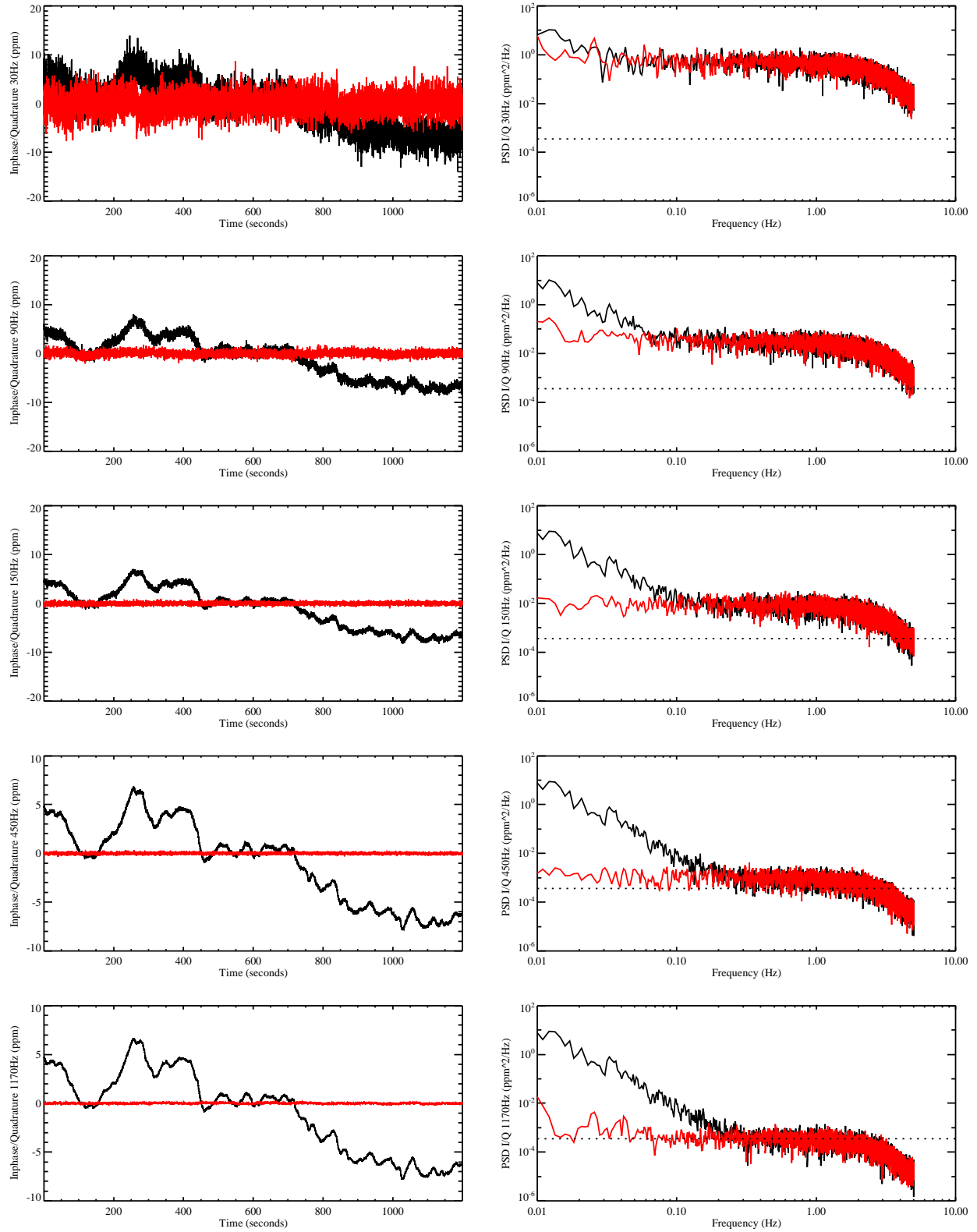


Figure 3-13 – GEM-3 Static Measurements – Lower Frequencies. In-phase signals are shown in black and quadrature signals are shown in red. The lowest white noise level at 3930 Hz is indicated with a dotted line in the right-hand panels.



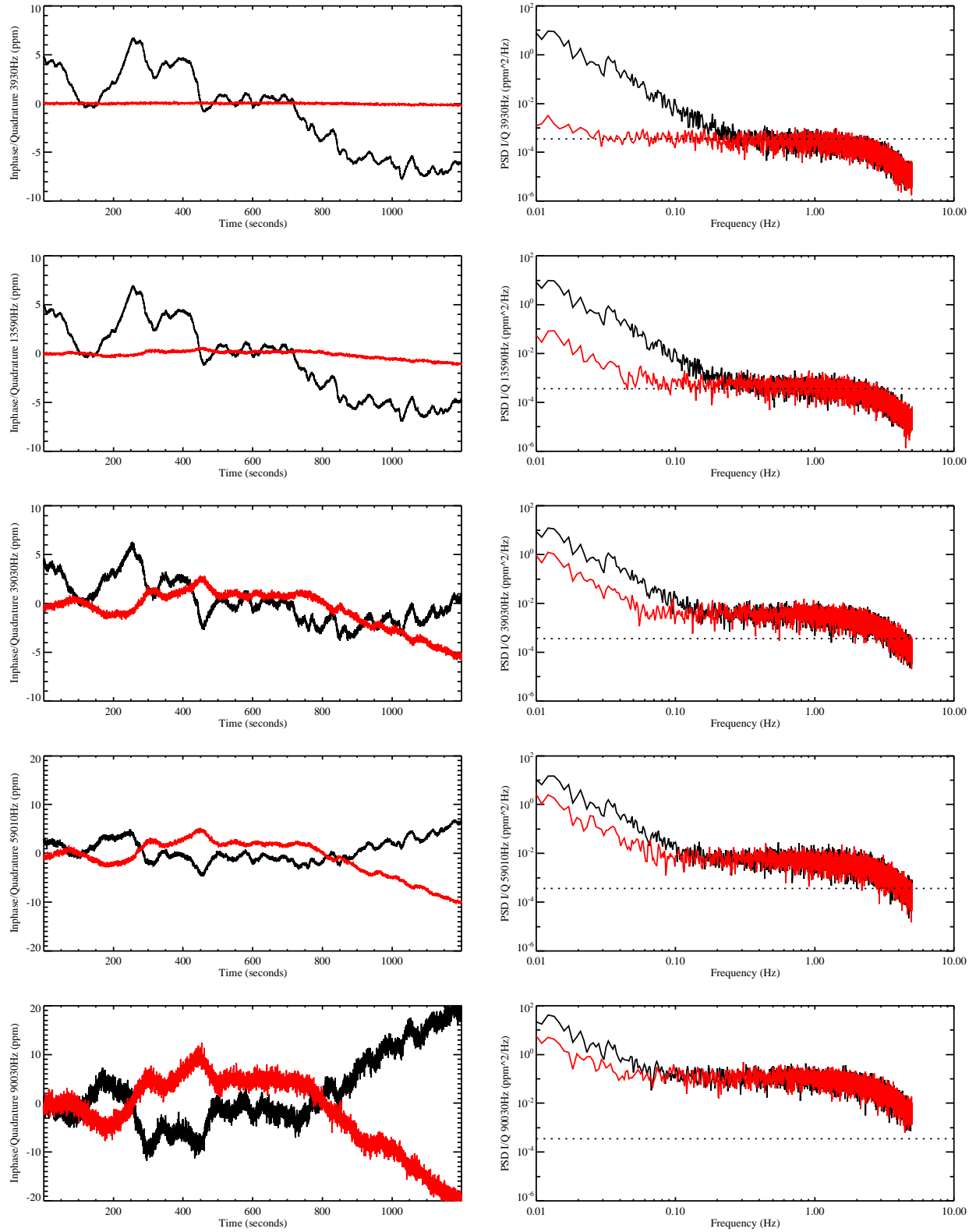


Figure 3-14 – GEM-3 Static Measurements – Upper Frequencies. In-phase signals are shown in black and quadrature signals are shown in red. The lowest white noise level at 3930 Hz is indicated with a dotted line in the right-hand panels.

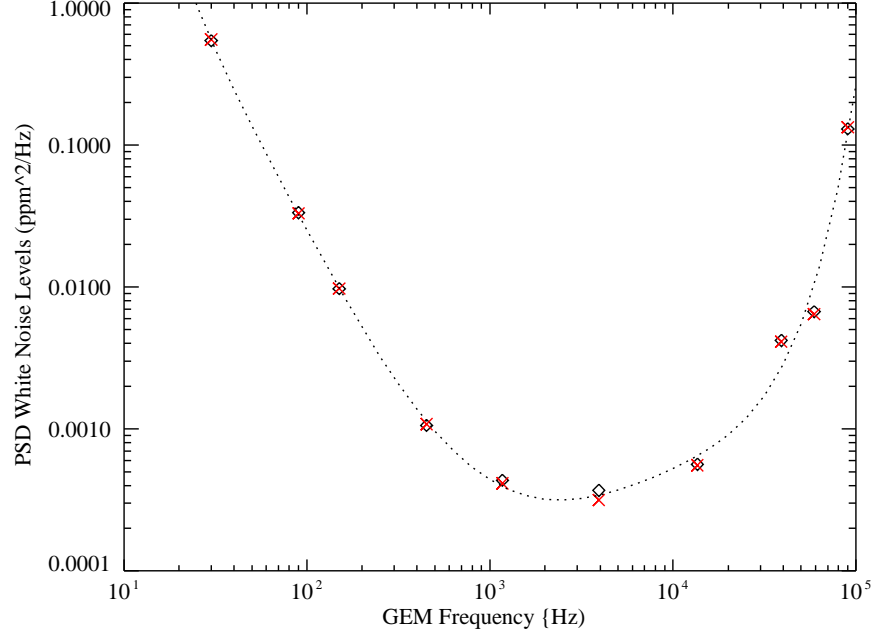


Figure 3-15 – White Noise Levels for GEM-3 Static Measurements. Measurements at each transmit frequency are shown as symbols (black diamonds – in-phase, red x's – quadrature). A polynomial fit to the data is shown as a dashed line.

### 3.7.3 Geological Response

The response of EMI sensors to soil has been investigated and modeled extensively in both geophysical and landmine situations [8-11]. The soil can be considered as a half space with both electrical conductivity,  $\sigma$ , and magnetic susceptibility,  $\chi$ . For a coaxial sensor with a circular transmit coil of radius  $a$  and circular receive coil of radius  $b$ , the voltage induced by a sinusoidal transmit field of frequency  $\omega$  can be expressed as:

$$v = i\mu_0\omega\pi ab \int_0^\infty \Gamma(\lambda, u_1, \chi) \times J_1(\lambda a) J_1(\lambda b) \exp(-2\lambda h) d\lambda,$$

where  $h$  is the height above ground,  $u_1 = \sqrt{\lambda^2 + i\sigma\mu_0\omega}$ , and:

$$\Gamma(\lambda, u_1, \chi) = \frac{\lambda(1 + \chi) - u_1}{\lambda(1 + \chi) + u_1}.$$

$J_1$  is a Bessel function of the first kind and of order 1.  $\lambda$  is the variable of integration. For the GEM-3 sensor, the voltage induced can be calculated by differencing the voltages induced for the transmit/receive and the bucking/receive radii combinations. To express the result in GEM-3 units of parts-per-million (ppm), one can calculate and divide by the voltage that would be induced directly in the receive coil by the transmit coil if the bucking coil were not there given by:

$$v = i\mu_0\omega\pi ab \int_0^{\infty} J_1(\lambda a)J_1(\lambda b)d\lambda.$$

The soil conductivity can be represented with a frequency independent real constant. In general, it has been found to be necessary to represent the soil magnetic susceptibility with a complex, frequency dependent term [8,12,13]. While various forms of this frequency dependence have been proposed, we have chosen to start out fitting GEM-3 measurements of the soil with a complex frequency-independent susceptibility of the form:  $\chi = \chi_R + i\chi_I$ . Numerical integration was used to evaluate these equations.

Figure 3-16 plots the results of the GEM-3 response based on this model. The sensor height input is 0.15 m. The solid curve soil parameters are: conductivity of 0.01 mho/m, real susceptibility of  $5.0 \times 10^{-4}$ , and imaginary susceptibility of  $-0.5 \times 10^{-4}$ . The dotted curve soil parameters are the same for susceptibility, but an increased conductivity of 0.1 mho/m. The black curves are in-phase and the red curves quadrature. The in-phase response (black curve) is negative and constant up to frequencies of 10 kHz. The amplitude of this response is driven by the magnitude of the real susceptibility term. As soil conductivity increases, the high frequency in-phase response begins to curve towards zero. The quadrature response has a small positive offset at low frequencies that is a result of the small, negative, imaginary term for the susceptibility. At higher frequencies, the quadrature response increases and has larger values for higher soil conductivities.

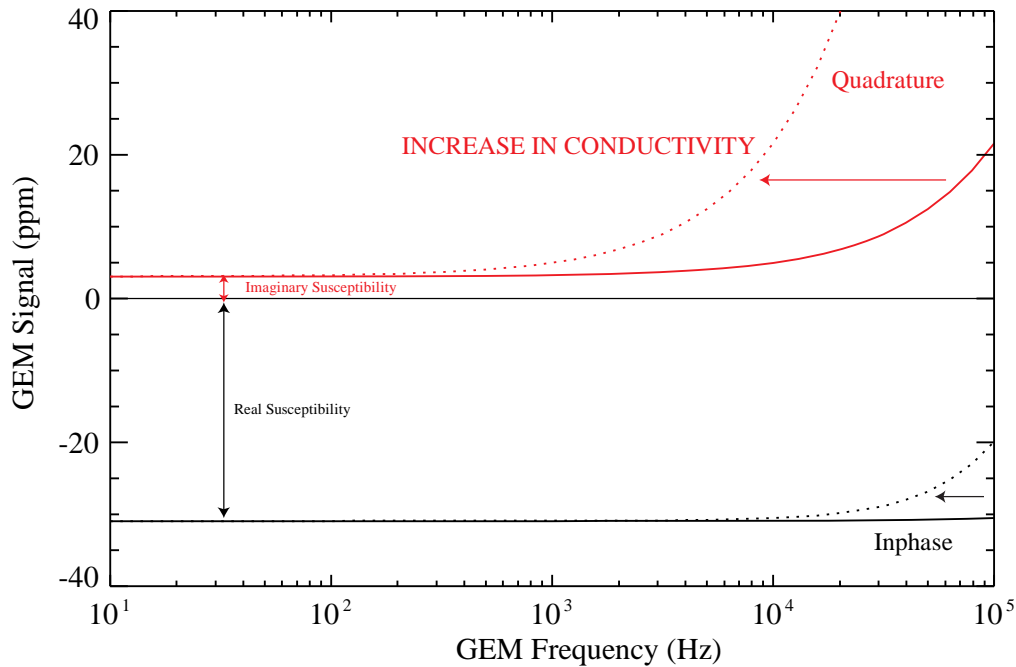


Figure 3-16 – Soil Model Response for the GEM-3 sensor. In-phase response is shown in black and quadrature response is shown in red. The solid lines represent a soil conductivity of 0.01 mho/m, the dashed lines 0.1 mho/m.

For expected soil parameters, the model for the GEM-3 indicates that strong signals are at heights of 0.25 m and less. The tower/rail system could not measure soil response below 0.25 m with the GEM-3 and recorded signal amplitudes less than ten ppm (see Figure 2-12). To better resolve the soil response, the three Blossom Point sites were re-visited in the summer of 2007 with the GEM-3 attached to its standard support stick. The rail track locations were re-located with GPS. For each site, two arbitrary locations were selected along the track. To obtain the drifting GEM-3 zero levels, the GEM-3 was held high in the air between measurements. To obtain measurements at controlled heights a set of eight plastic shelves (0.06 m thick) were piled on the ground consecutively. The procedure was to measure ten seconds in the air, ten seconds at a given shelf height, back in the air, and then add another shelf. To check for reproducibility, data was collected twice, piling the shelves up and then taking the shelves away.

Figure 3-17 and Figure 3-18 plot the results from the “Boat Launch” track and the “Environmental Area” track. The plots on the top are in-phase and the plots on the bottom are quadrature. The plots on the left are data from all heights as a function of frequency. The plots on the right are data at two frequencies as a function of height. Measured data are plotted with symbols connected with black curves. Fits of the data to the simple model are plotted as colored curves. The data were fit to the model with four parameters: conductivity, real susceptibility, imaginary susceptibility, and a fixed shift in height to account for uneven ground. The quadrature measurements were reproducible to within a fraction of a ppm and could be closely matched by the model both as a function of height and frequency.

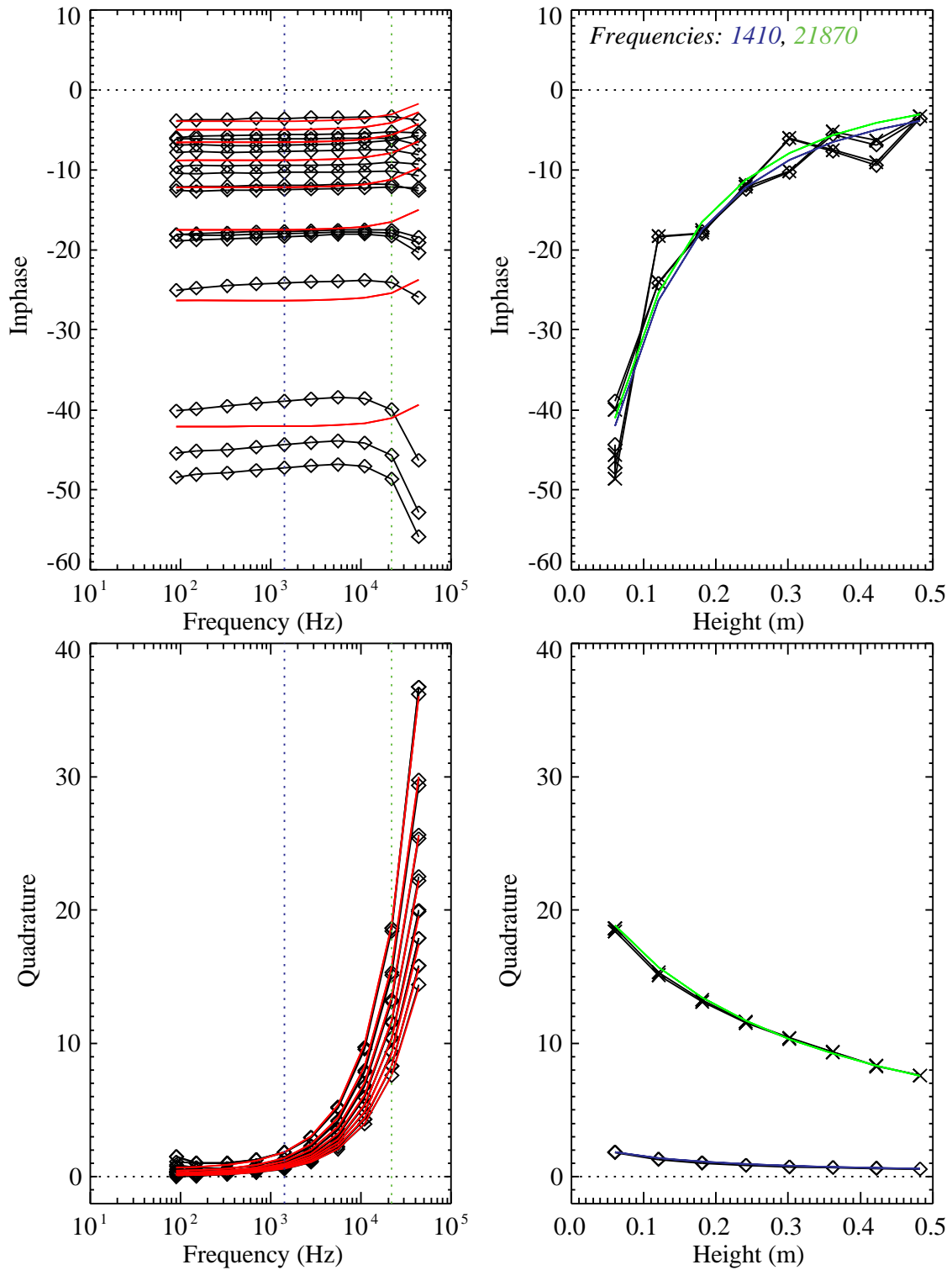


Figure 3-17 – Soil Response for the GEM-3 at the Boat Launch Area. The experimental data are shown as black lines and symbols. The red lines in the left-hand panels represent model fits to each data set (measurement height). The colored lines in the right-hand panels represent model fits at a particular frequency as a function of measurement height.

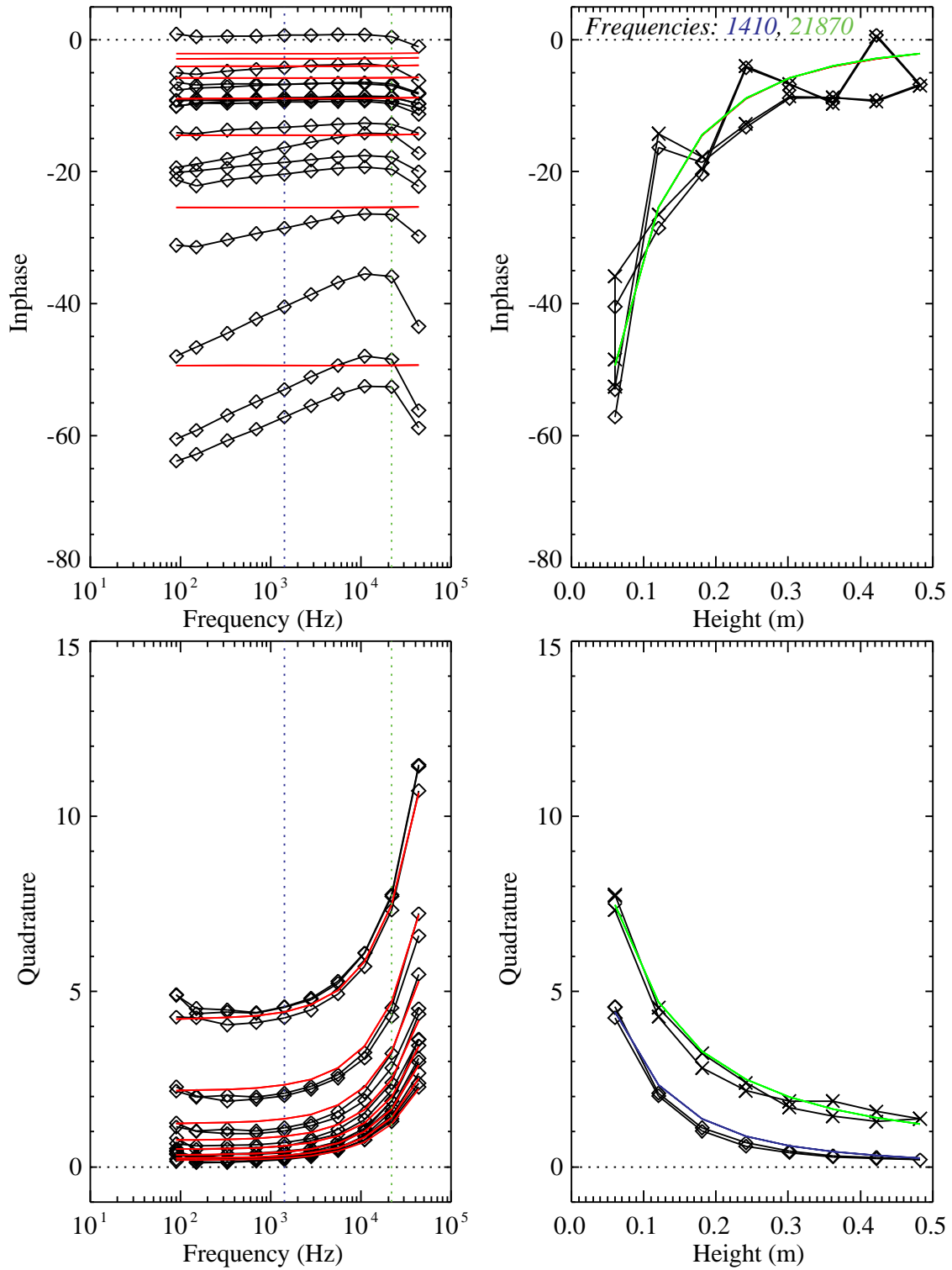


Figure 3-18 – Soil Response for the GEM-3 at the Environmental Area. The experimental data are shown as black lines and symbols. The red lines in the left-hand panels represent model fits to each data set (measurement height). The colored lines in the right-hand panels represent model fits at a particular frequency as a function of measurement height.

The in-phase measurements were not completely reproducible. There appears to be a general trend in height and frequency dependence, but the subtraction of the zero level does not appear to be working. One possibility is that the process of moving the GEM-3 from high in the air down to the shelf causes the in-phase zero level to shift irregularly. It is possible that small flexes in the sensor coil head is shifting the zero. For future measurements, it will be necessary to test this and see if the GEM-3 can be supported in some fashion to eliminate these shifts.

The measured in-phase signal is also not constant as a function of frequency below 10 kHz. There is a constant small slope across this frequency span. This frequency dependence is consistent with some proposed models for the behavior of soil magnetic susceptibility [8,12,13]. This model is described as a log-uniform distribution of magnetic relaxation times. The range of relaxation times is given by the model parameters of  $\tau_1$  and  $\tau_2$ . The frequency dependence of the susceptibility is given as:

$$\chi(\omega) = \chi_0 \left( 1 - \frac{1}{\ln(\tau_2/\tau_1)} \cdot \ln\left(\frac{i\omega\tau_2 + 1}{i\omega\tau_1 + 1}\right) \right)$$

If one assumes that the relaxation times are significantly above and below the bandwidth of the GEM-3 ( $\tau_1 < 10^{-7}$  s and  $\tau_2 > 0.1$  s) and apply this equation to the soil response calculation, one can match the sloped inphase responses observed. Figure 3-19 plots the measured “Environmental Area” data versus model-based fits to the data (red and green curves). The slope in the inphase is reasonably matched. Above 10 kHz, the in-phase signals tend to curve downwards. Currently, there is no explanation of this. It will have to be explored further in future work.

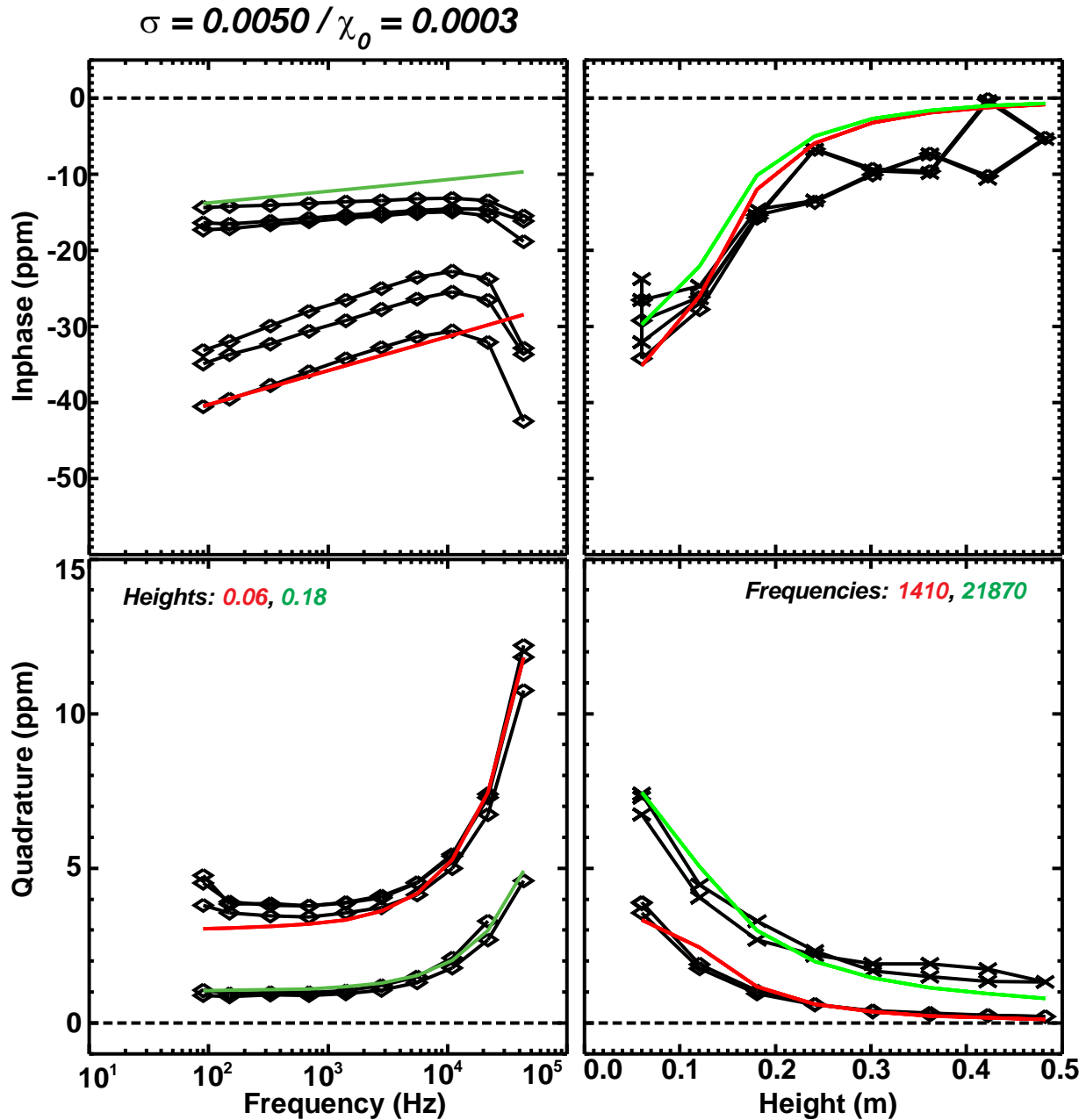


Figure 3-19 – Match of frequency dependent susceptibility model (red and green curves) to measured GEM-3 soil response (black curves and symbols) at the Environmental Area.

Overall soil parameters are presented in Table 3-6. Fitted soil conductivities are driven by the more stable quadrature measurement and range from 0.002 to 0.093 mho/m with the track measurements. The larger conductivities were at the “Boat Launch” site which was located next to and at a small elevation (less than 1 m) above the tidal Potomac River. Two additional measurements were taken on a sandy beach near the track; one at the waters edge in saturated sand and one halfway up the beach on dry sand. As expected, increasing levels of conductivity were found. An unexpected result was noted in the surface offset parameter. Table entries flagged in red could only fit the quadrature data if the surface was shifted significantly lower



than it really was. It appears that the model fits the data best based on the water level in the soil. The top dry layer of soil is ignored. Because of this, the fitted susceptibility parameters are larger than expected; since magnetic minerals are probably present in the top dry layer, but the model is trying to fit them deeper. The “Boat Launch” offsets of roughly 0.3 m are consistent with the soil moisture profiles in Figure 3-8. To fit this data more accurately, the data should be fit to a layered model. This may be attempted with future measurements. It may also be useful to take soil cores to note depths where changes in soil type take place.

Table 3-6 – Fitted Soil Model Parameters for the Blossom Point Test Areas

	Conductivity (mho/m)	Real Susceptibility (SI)	Imaginary Susceptibility (SI)	Surface Offset (m)	COMMENTS
<b>Boat Launch</b>		$\times 10^{-4}$	$\times 10^{-4}$		
1	0.093	<b>42</b>	<b>-0.59</b>	<b>0.262</b>	High Ground Along Rail Track
2	0.069	<b>44</b>	<b>-0.68</b>	<b>0.315</b>	High Ground Along Rail Track
3	0.32	7.9	-0.02	0.004	On Beach at Waterline
4	0.21	<b>12</b>	-0.04	<b>0.102</b>	On Beach above Waterline
<b>Environmental Area</b>					
1	0.005	2	-0.2	0.02	
2	0.0096	<b>12</b>	<b>-0.1</b>	<b>0.125</b>	
<b>L Range</b>					
1	0.0026	1.7	-0.085	0.01	
2	0.0021	0.9	-0.063	0.02	

Locations with a small fitted surface offset have real susceptibility values in the range of  $1 - 8 \times 10^{-4}$  and negative imaginary values that are 5-10% of the real value. The Bartington sensor measured real values in the range of  $10.0 \times 10^{-6} \text{ cgs}$  which corresponds to  $1.2 \times 10^{-4} \text{ SI}$  (units of soil model). The match is reasonable. The Bartington model used measures only the real susceptibility at a single frequency (0.958 kHz) and will not help with the indications from the GEM-3 of frequency dependent, complex values.

### 3.7.4 Motion-Induced Noise

As discussed above, three different platforms were used to try and characterize motion-related EMI noise: the man-portable cart, the MTADS EM towed trailer platform, and specially constructed rail/tower system (Figure 2-5, Figure 2-7, Figure 2-6 respectively). The first two were chosen as typical survey systems and the third was meant to contrast as an example of very smooth motion. Besides the GEM-3, each system had a GPS antenna attached to a tripod and an IMU box bolted down in order to measure to nature of the platform's motion. At each of the three sites, these systems were moved back and forth along approximately the same track.

Figure 3-20 and Figure 3-21 plot the measured motion of the cart at the Environmental Area. The top graph in Figure 3-20 shows the X, Y track as measured by the GPS antenna. For all three platforms, local X and Y are derived from the GPS output in UTM Easting and Northing (meters) with an arbitrary offset ( $X_0$ ,  $Y_0$ ) subtracted. When required, the local X,Y would be rotated to make X roughly aligned along-track and Y roughly cross-track. Positive Z is up in all cases. The red section of the track was an individual pass selected out and shown in subsequent plots. The walking speed of the cart was just over one meter per second. The dominant motion of this wheel barrow-styled cart was a pitching motion at the frequency of a person's stride. This shows up most clearly in the pitch in Figure 3-20 and the  $\omega_y$  angular rate in Figure 3-21. There are related components of this steady bouncing/walking motion in both the roll angle and the x-direction angular rate ( $\omega_x$ ), as well as the accelerations in the x and z directions ( $a_x, a_z$ ) but they are not so clear or consistent. Presumably much of the broad spectrum of motion is from the platform rolling side-to-side and moving up/down as the wheels roll over the uneven ground surface. Figure 3-22 and Figure 3-23 raster the in-phase and quadrature response of the GEM-3 over the same time interval. From top to bottom, the plots progress from low (90 Hz) to high (44.37 kHz) GEM-3 transmitter frequency. The bottom plot combines the highest five frequencies (black - 2,610 Hz, red - 5,430 Hz, green - 11,430 Hz, blue - 20,010 Hz, and magenta - 44,370 Hz). The large signal at the start is from a test sphere placed along the track. At low transmitter frequencies, the in-phase and quadrature signals are much noisier and not very coherent between frequencies. At high frequencies (2,610-20,010 Hz), the in-phase noise becomes almost perfectly coherent. The quadrature noise in this frequency range is moderately coherent, but growing in amplitude. At the highest frequency, it appears that the in-phase and quadrature signals maybe mixed by an uncorrected phase shift.

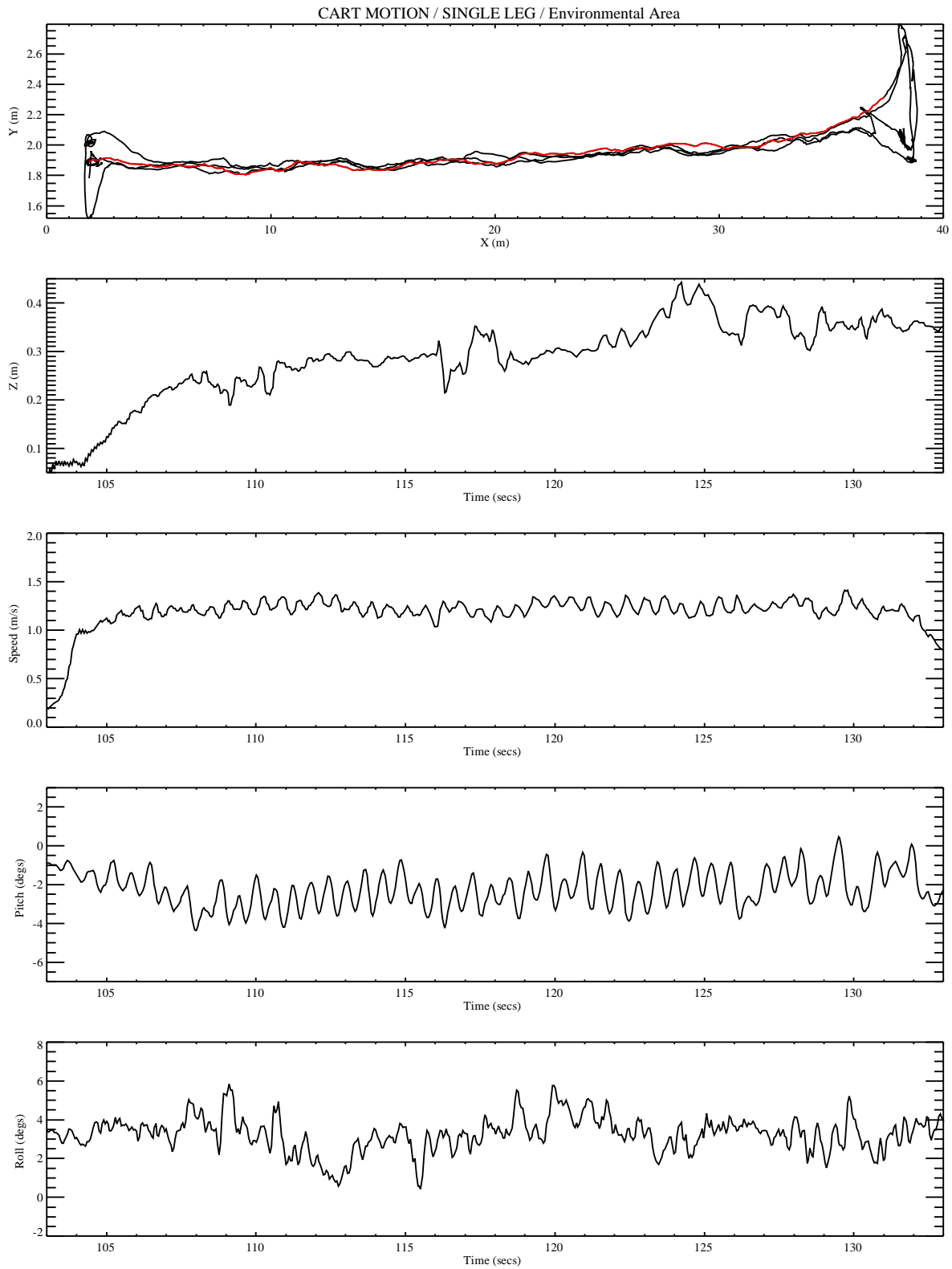


Figure 3-20 – MTADS MP Cart Motion Characterization – X,Y,Z, Pitch, and Roll. The upper panel shows the local course-over-ground for several data sets. The data associated with the leg color-coded red was the data source for the following discussion.

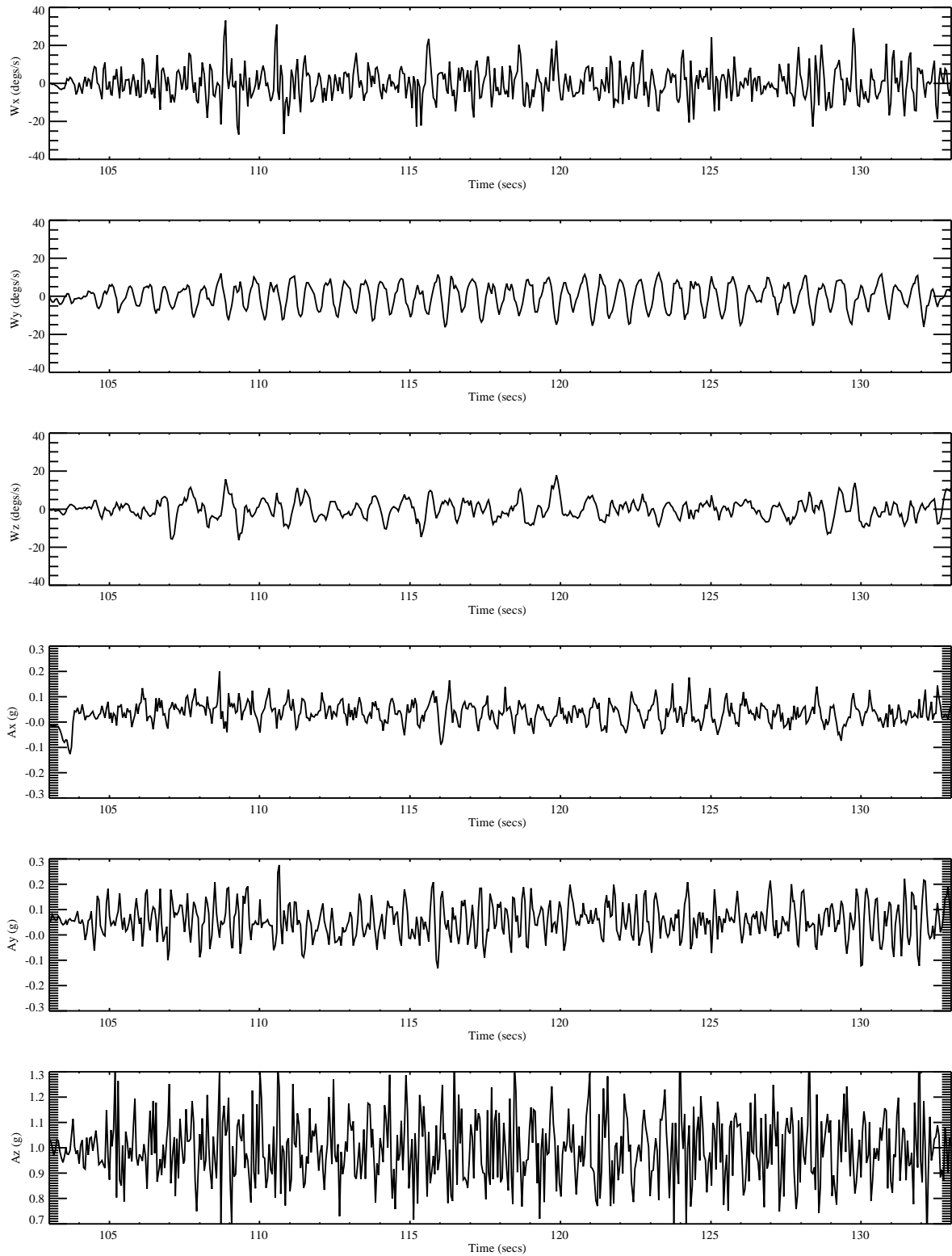


Figure 3-21 – MTADS MP Cart Motion Characterization – IMU Angular Rates and Accelerations

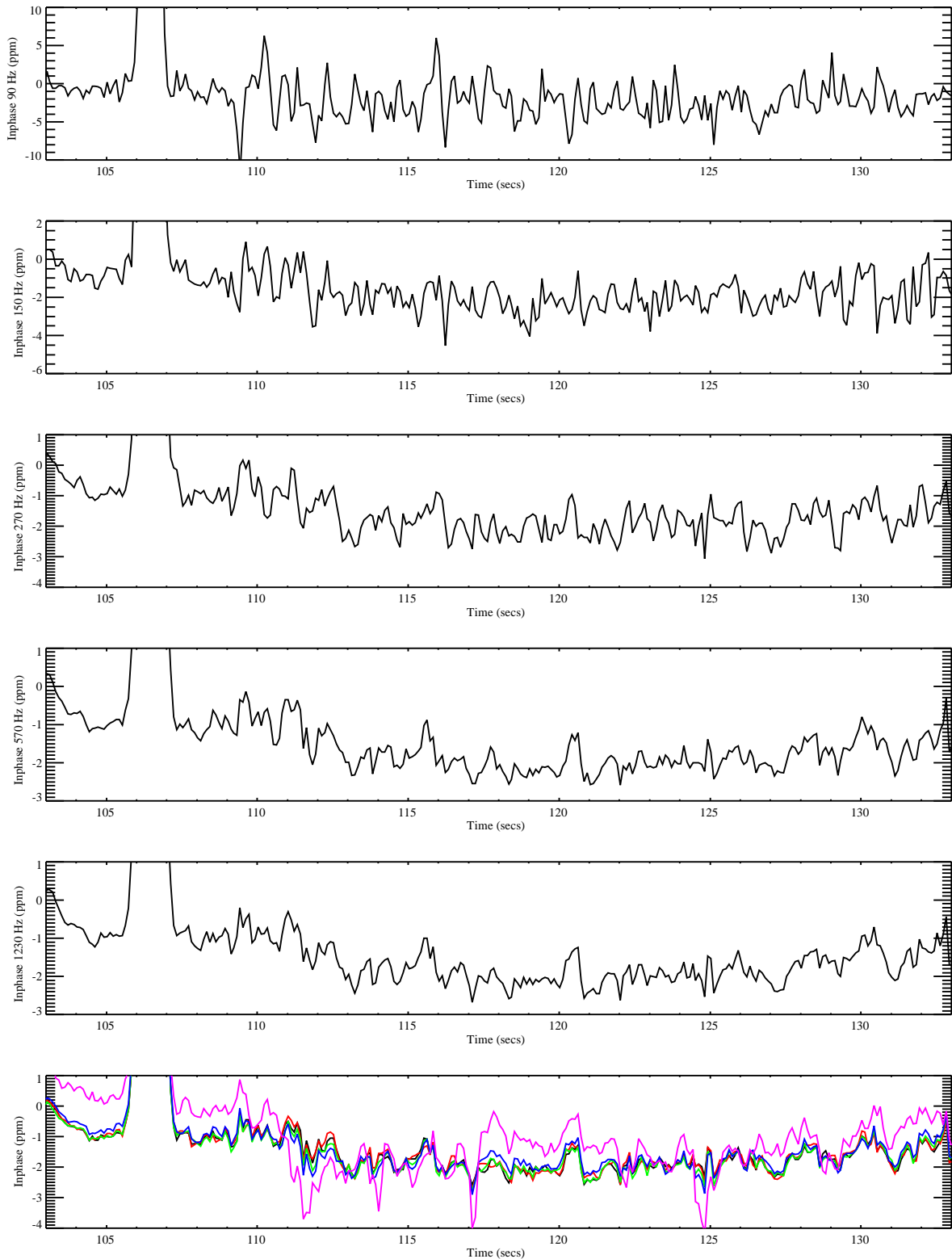


Figure 3-22 – MTADS MP Cart – GEM-3 In-phase Response. The in-phase data for the five lowest frequencies are presented in the upper panels. The bottom panel presents the in-phase data for the five highest frequencies (black - 2,610 Hz, red – 5,430 Hz, green – 11,430 Hz, blue – 20,010 Hz, and magenta – 44,370 Hz).

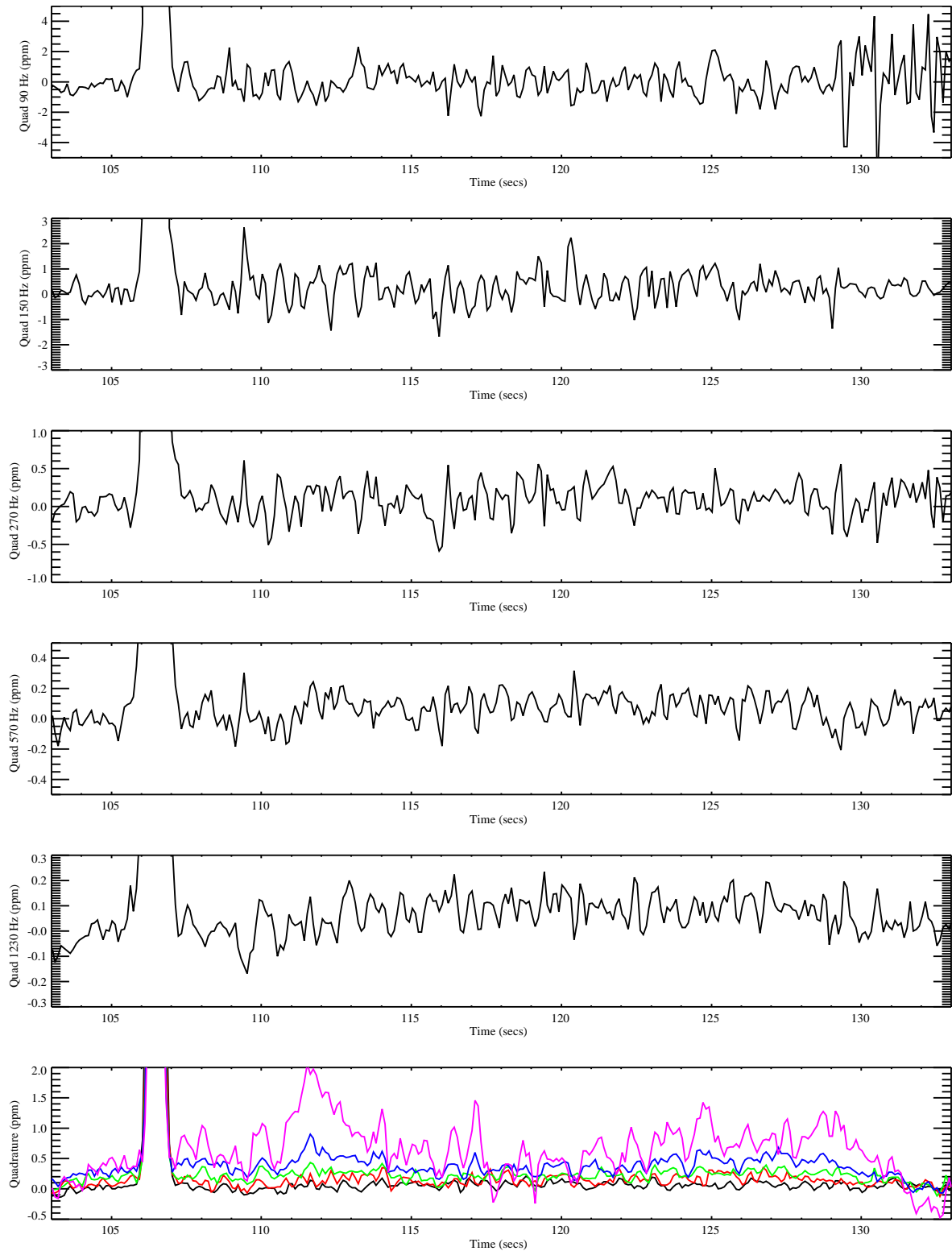


Figure 3-23 – MTADS MP Cart – GEM-3 Quadrature Response. The quadrature data for the five lowest frequencies are presented in the upper panels. The bottom panel presents the quadrature data for the five highest frequencies (black - 2,610 Hz, red – 5,430 Hz, green – 11,430 Hz, blue – 20,010 Hz, and magenta – 44,370 Hz).

Figure 3-24 plots averaged spectra of the GEM response and IMU motion. These spectra were calculated and averaged from short time intervals of data where no obvious signal was present. The top two plots are PSD's of the in-phase and quadrature responses. The curves from top to bottom are mostly low to high transmit frequency with the highest GEM-3 frequencies shifting back up again. The dotted line indicates the lowest white noise level measured in the stationary tests. Only the quadrature signals at mid-frequencies approach the stationary sensor noise. The lower two plots are PSD's of the accelerations and angular rates measured by the IMU (black -  $a_x/\omega_x$ , red -  $a_y/\omega_y$ , green -  $a_z/\omega_z$ ). The angular rate,  $\omega_y$ , peaks at 0.8, 1.6, 2.4, and 3.2 Hz. The second harmonic dominates. The lower two peaks are also apparent in the GEM-3 PSD, particularly in the in-phase.

Figure 3-25 through Figure 3-29 show similar plots using the MTADS EMI tow platform on the L Range. The red section of the track in the upper panel of Figure 3-25 is an individual pass selected out and shown in the subsequent plots. The measured motion is very different in character. The platform is a large composite A-frame shape connected to the vehicle trailer hitch and two large tires. The GEM-3 is centered on a large flat board that normally holds an array of three EMI sensors. The platform speed is around 1.5 m/s. Pitch, roll, and the angular rates are much smaller in amplitude compared to the man-portable cart. The dominant motion appears to be in  $a_z$  with a broad PSD peaked at 5 Hz. It is assumed that this is some flexing/vibrating mode of the trailer frame. The IMU was only sampled at 20 Hz and the VG300 model has a 3dB response roll off at 10 Hz. In future work, an IMU with a broader response range and sampled at a higher data rate should be used. The GEM-3 was sampled at 10 Hz (3 base period averaging applied) resulting in a 5 Hz Nyquist frequency. The in-phase signal shows a broad peak in the 3 Hz range. The quadrature signal does not show any dominant peak. The overall noise levels are highest at low GEM-3 frequencies and lowest in the mid-frequency range. Further measurements should be made with the GEM-3 running at its highest (30 Hz) data rate.

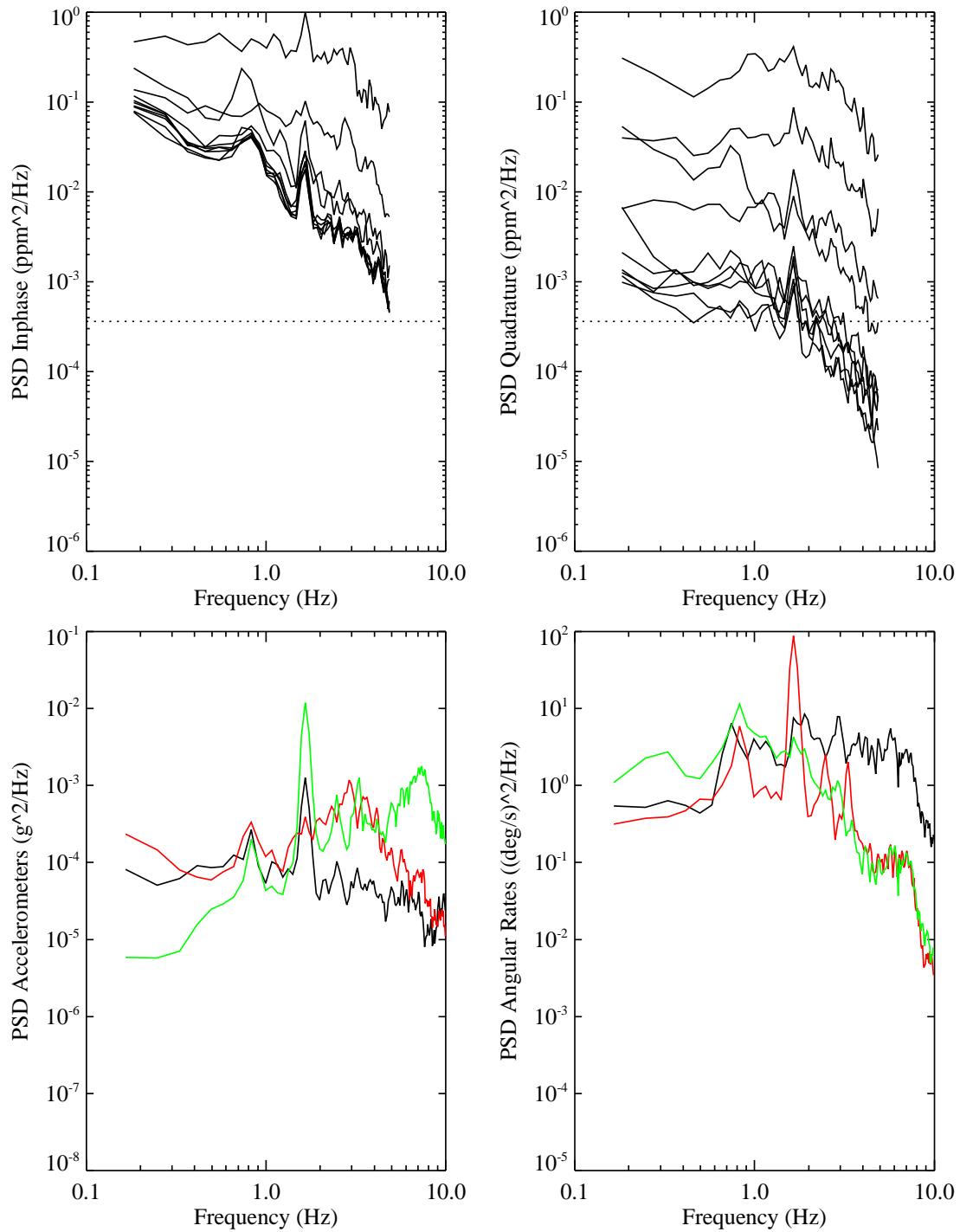


Figure 3-24 – MTADS MP Cart – Power spectra of the GEM-3 response and the IMU motion. An individual black line is show for each frequency in the upper panels (see text for discussion). The acceleration and angular rate PSDs are shown in the lower panels (X – black, Y – red, Z – green). The dotted line in the upper panel indicates the lowest white noise level measured in the stationary tests.



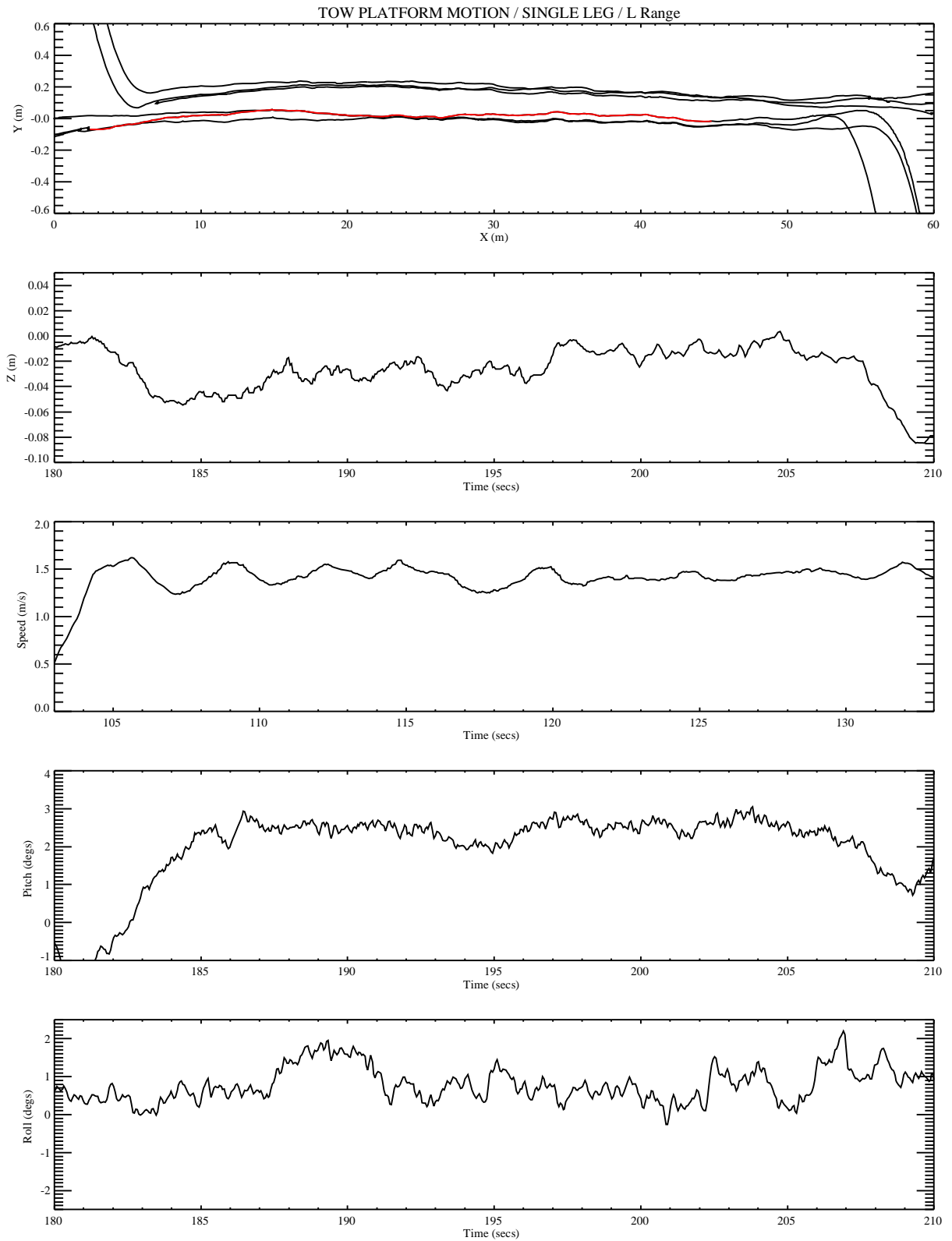


Figure 3-25 – MTADS EM Trailer Motion Characterization – X,Y,Z, Pitch, and Roll. The upper panel shows the local course-over-ground for several data sets. The data associated with the leg color-coded red was the data source for the following discussion.

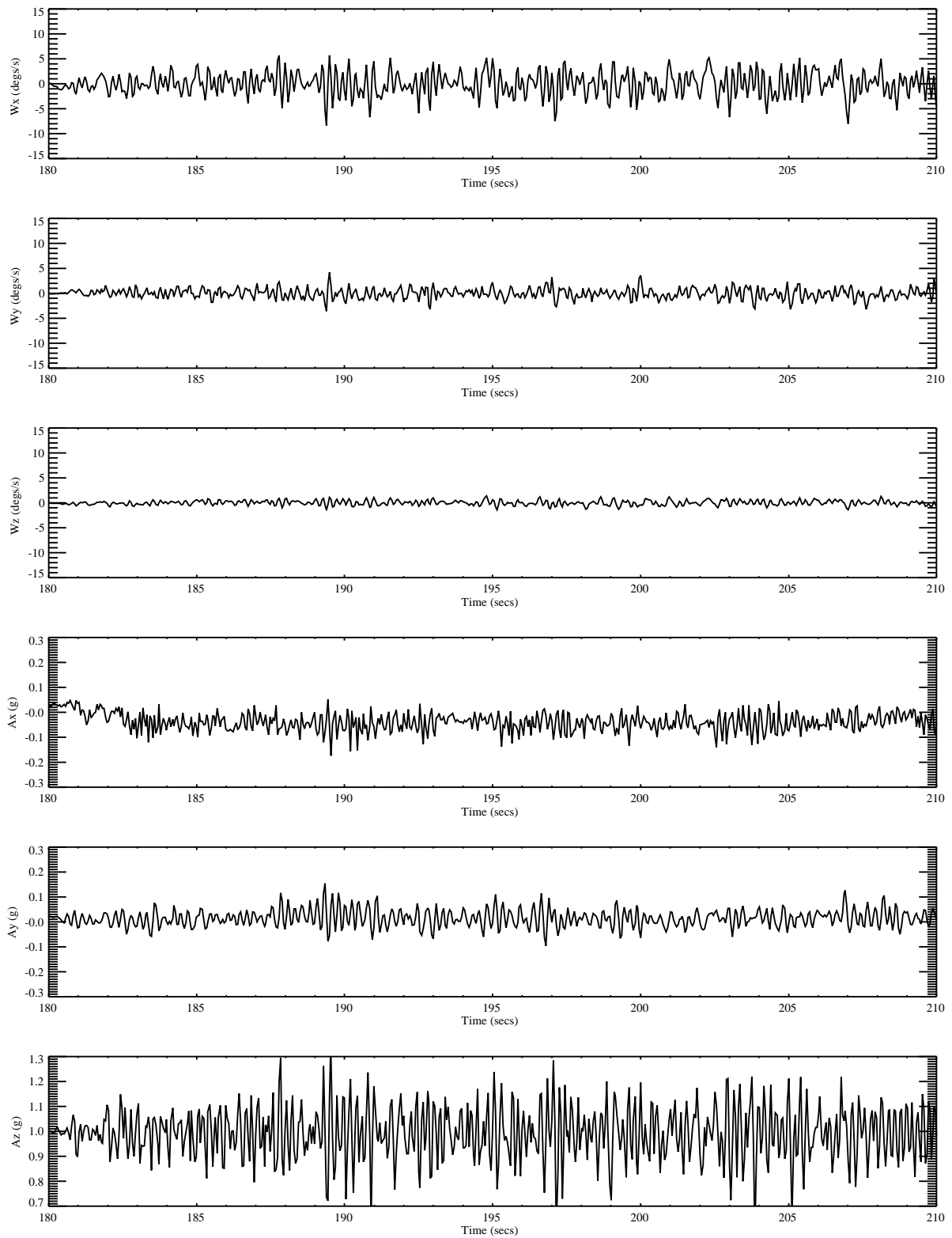


Figure 3-26 – MTADS EM Trailer Motion Characterization – IMU Angular Rates and Accelerations

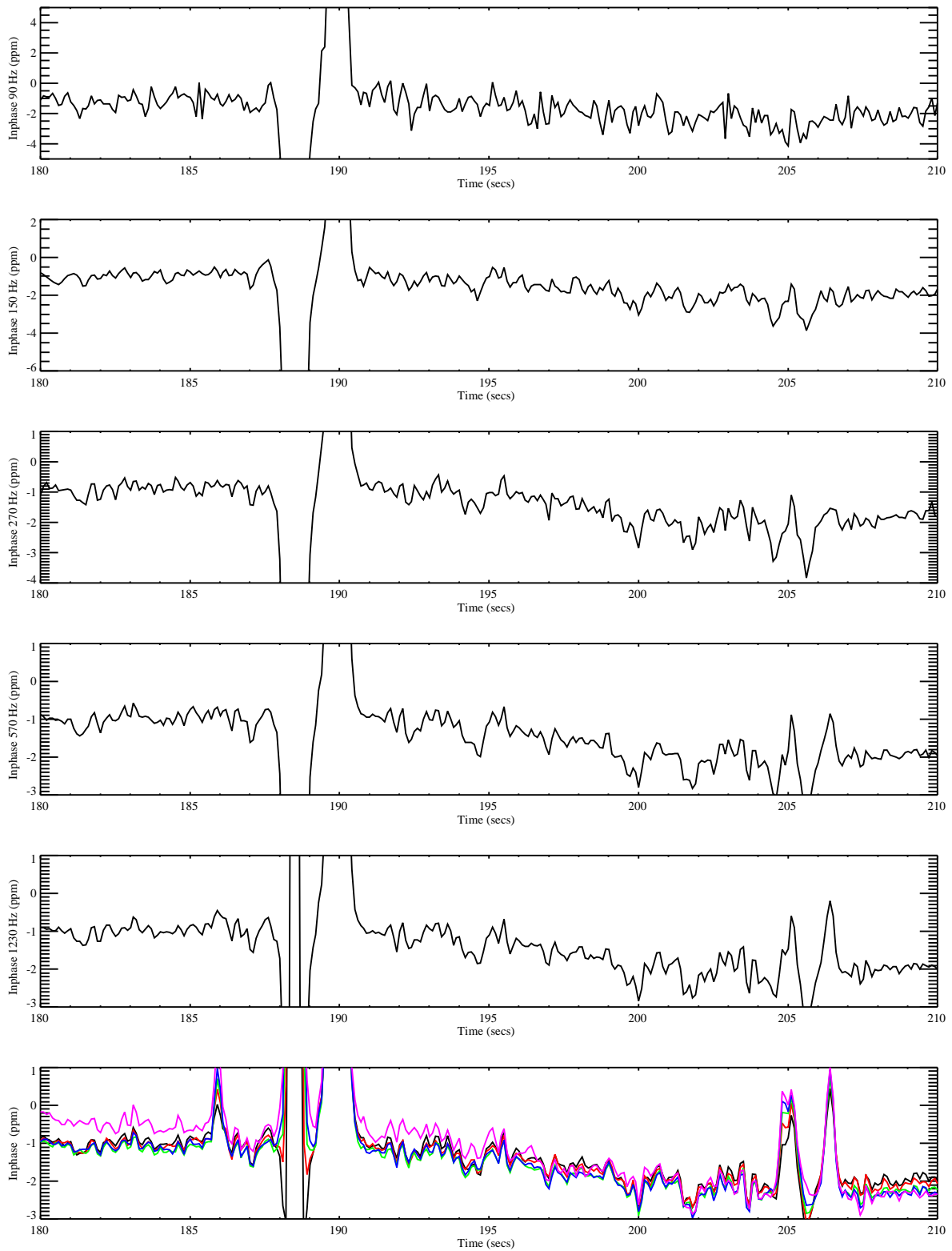


Figure 3-27 – MTADS EM Trailer Motion Characterization – GEM-3 In-phase Response. The in-phase data for the five lowest frequencies are presented in the upper panels. The bottom panel presents the in-phase data for the five highest frequencies (black - 2,610 Hz, red - 5,430 Hz, green - 11,430 Hz, blue - 20,010 Hz, and magenta - 44,370 Hz).

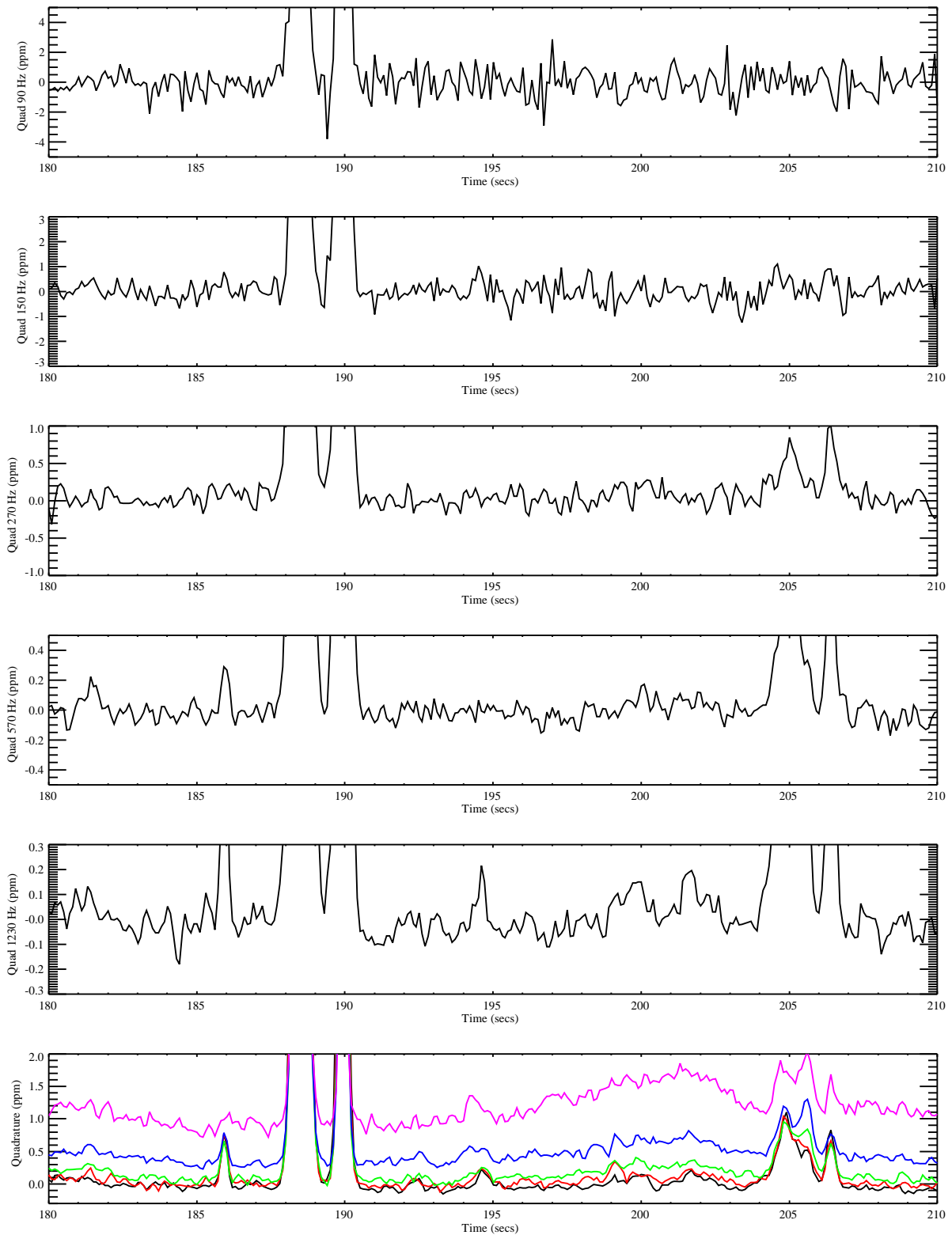


Figure 3-28 – MTADS EM Trailer Motion Characterization – GEM-3 Quadrature Response. The quadrature data for the five lowest frequencies are presented in the upper panels. The bottom panel presents the quadrature data for the five highest frequencies (black - 2,610 Hz, red – 5,430 Hz, green – 11,430 Hz, blue – 20,010 Hz, and magenta – 44,370 Hz).

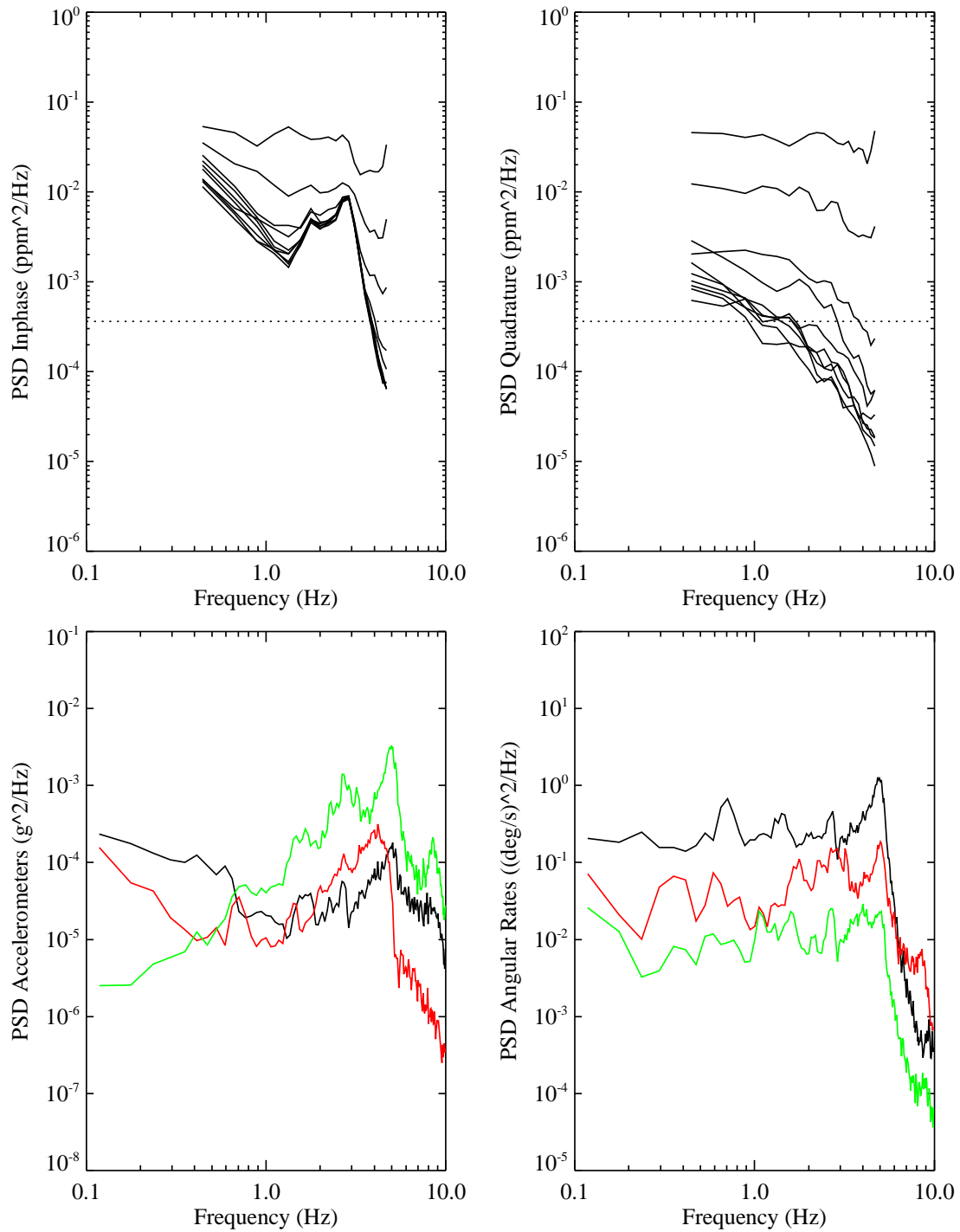


Figure 3-29 – MTADS EM Trailer Motion Characterization – Power spectra of the GEM-3 response and the IMU. An individual black line is show for each frequency in the upper panels. The acceleration and angular rate PSDs are shown in the lower panels (X – black, Y – red, Z – green). The dotted line in the upper panel indicates the lowest white noise level measured in the stationary tests.

Figure 3-30 through Figure 3-34 graph the results of moving the GEM-3 with the rail/tower system on the Environmental Area track. The intent was to have a platform that would move smoothly and presumably with little induced EMI sensor noise for comparison to the realistic survey platforms. Surprisingly, the results were the opposite. While the overall motion was relatively smoother, the tower structure had a high frequency, back and forth pitching vibration peaked around 7 Hz. Even though this vibration was small it had a significant effect on sensor noise. The in-phase signal shows a clear peak around 2 Hz. Like the L Range, these measurements would be clearer using an IMU with a greater bandwidth and the GEM-3 run at 30 Hz.

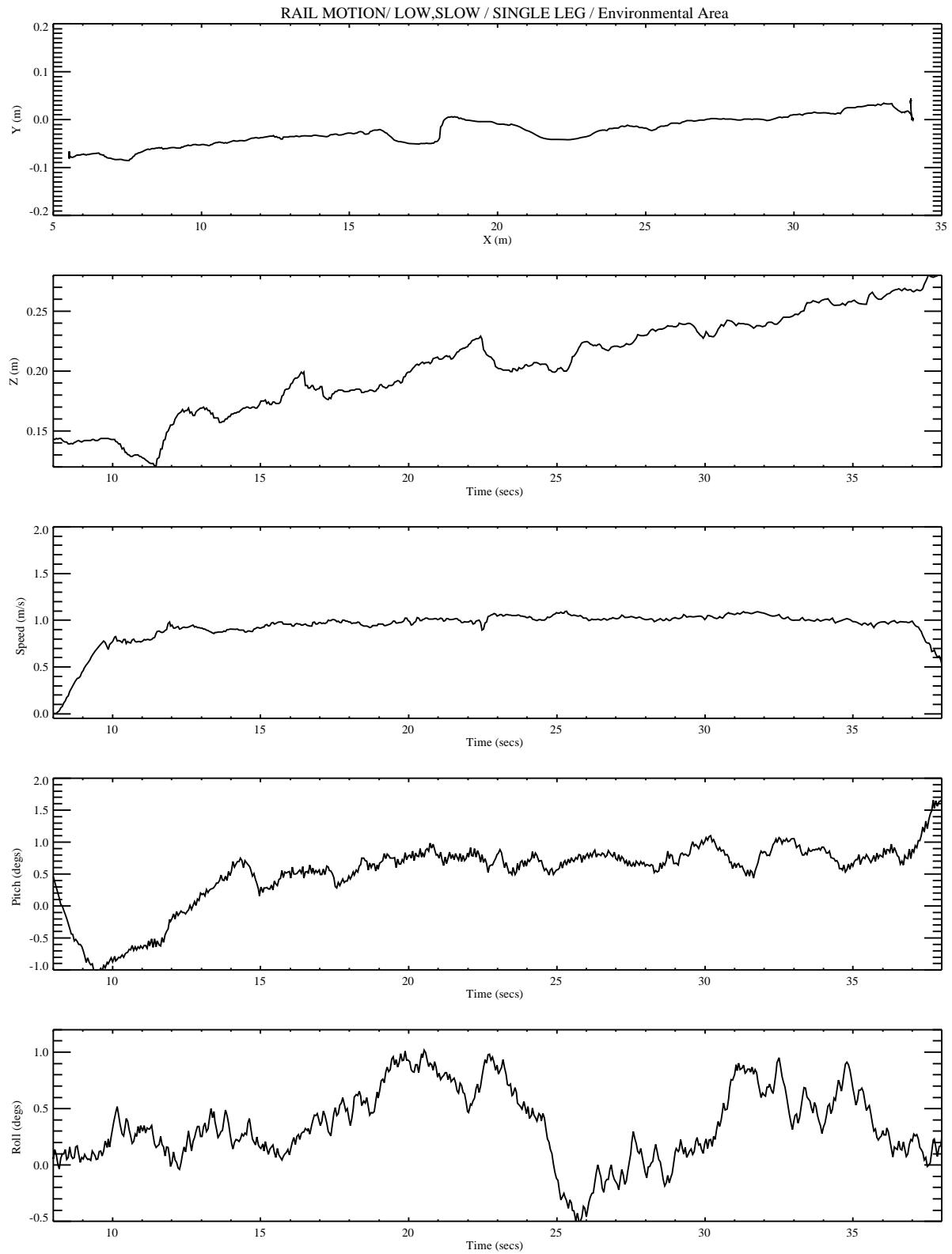


Figure 3-30 – Tower / Rail System Motion Characterization – X,Y,Z, Pitch, and Roll.

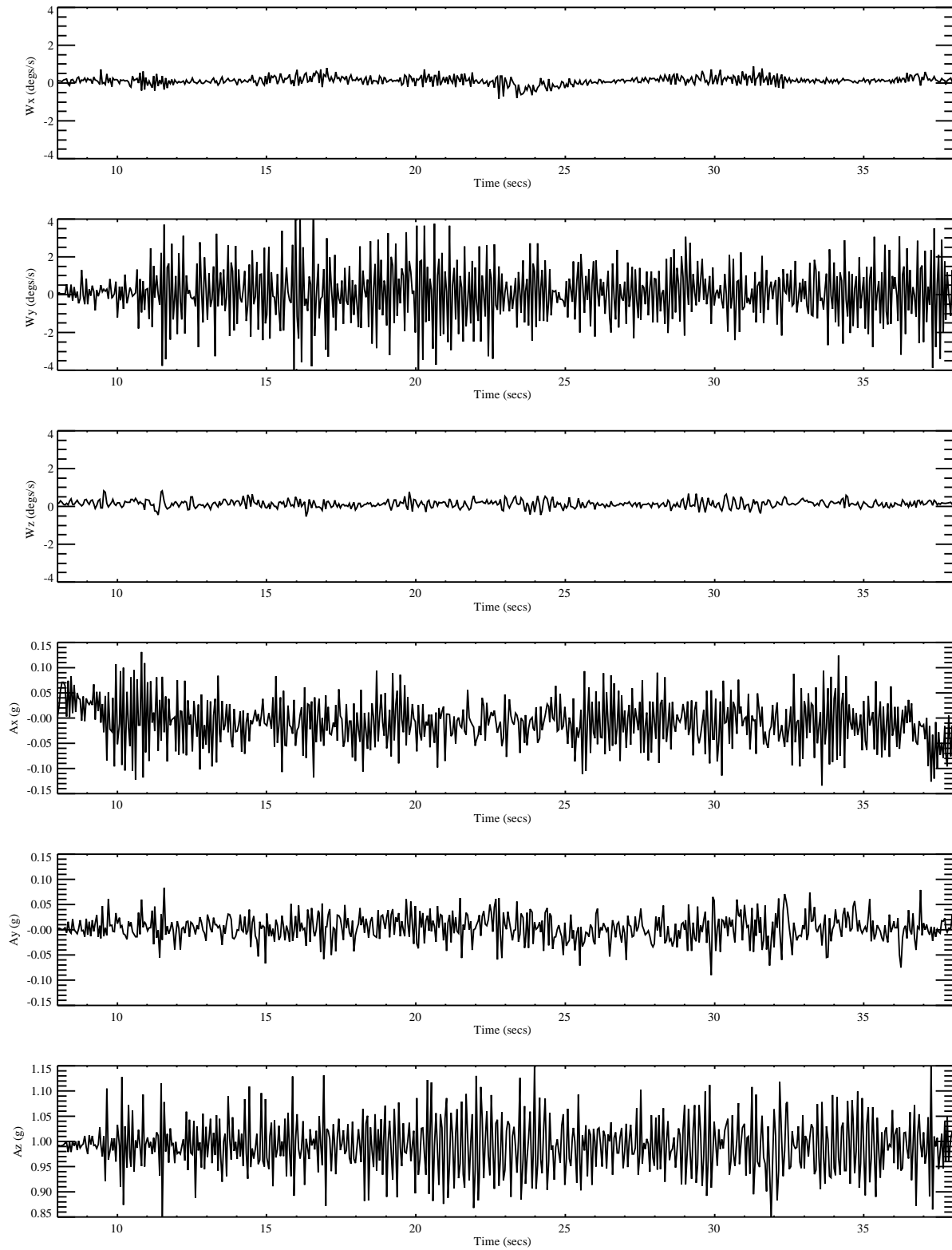


Figure 3-31 – Tower / Rail System Motion Characterization – IMU Angular Rates and Accelerations



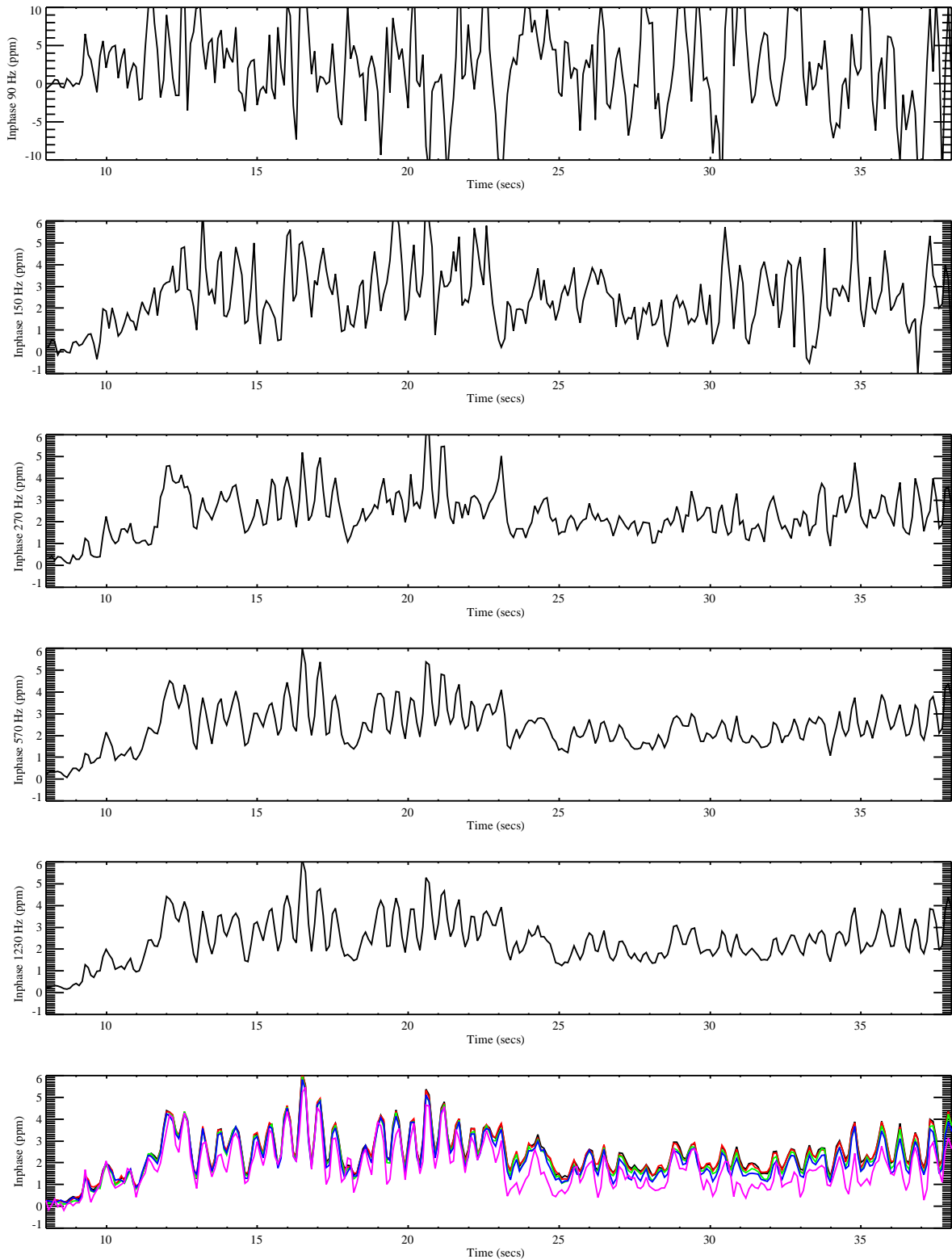


Figure 3-32 – Tower / Rail System Motion Characterization – GEM-3 In-phase Response. The in-phase data for the five lowest frequencies are presented in the upper panels. The bottom panel presents the in-phase data for the five highest frequencies (black - 2,610 Hz, red – 5,430 Hz, green – 11,430 Hz, blue – 20,010 Hz, and magenta – 44,370 Hz).

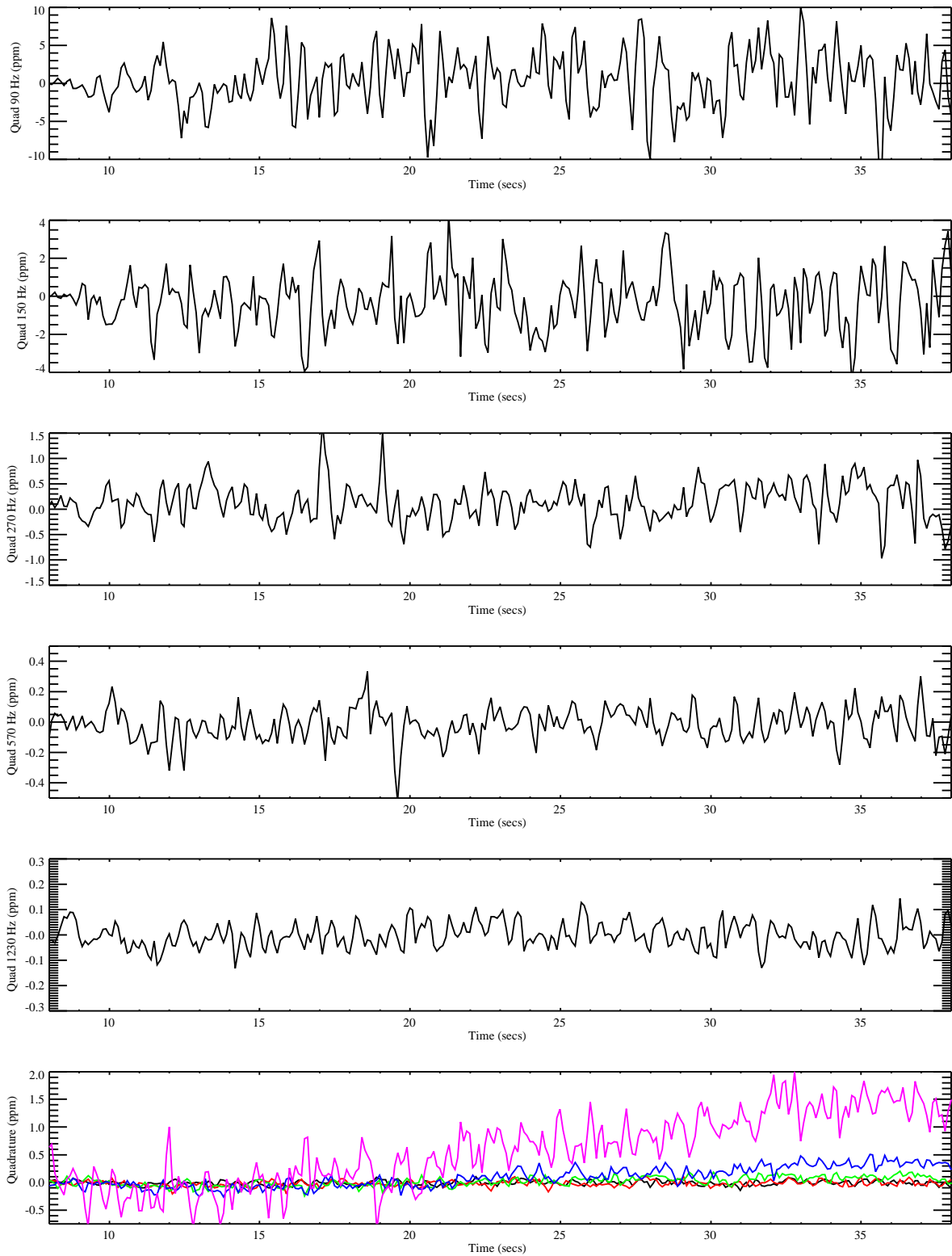


Figure 3-33 – Tower / Rail System Motion Characterization – GEM-3 Quadrature Response. The quadrature data for the five lowest frequencies are presented in the upper panels. The bottom panel presents the quadrature data for the five highest frequencies (black - 2,610 Hz, red – 5,430 Hz, green – 11,430 Hz, blue – 20,010 Hz, and magenta – 44,370 Hz).

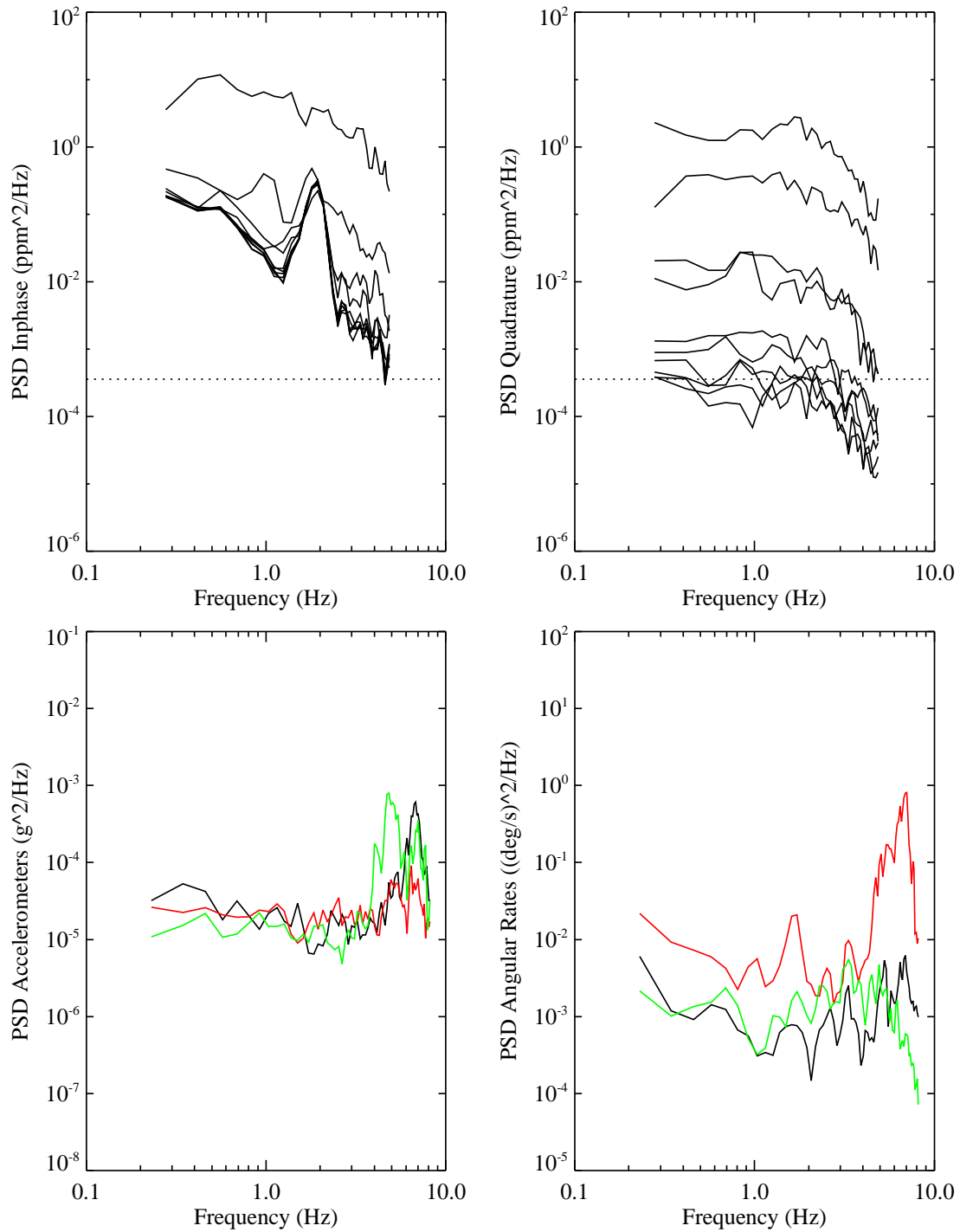


Figure 3-34 – Tower / Rail System Motion Characterization – Power spectra of the GEM-3 response and the IMU. An individual black line is show for each frequency in the upper panels. The acceleration and angular rate PSDs are shown in the lower panels (X – black, Y – red, Z – green). The dotted line in the upper panel indicates the lowest white noise level measured in the stationary tests.

As an overall comparison between platforms and sites, the standard deviation of the noise has been calculated on short (3 second) time scales and averaged over the “quiet” data collected (regions of no actual signal from discrete metallic objects). This time scale is shorter than the GEM-3 drift rate and slightly larger than the footprint of an actual signal (at speeds of ~1 m/s). Figure 3-35 plots the overall results. The black curves are the stationary noise levels. The curves for each site are: Environmental – red, L Range – green, and Boat Launch – blue. For a given platform, the noise levels are relatively consistent across the three sites. The biggest exception to this is the towed platform at the Boat Launch. The quadrature noise at high frequencies is much larger. This data was collected after torrential rains and the site was close to being flooded and the soil saturated. The noise is presumably due to increased soil conductivity. By platform, the rail system is the noisiest. The in-phase and quadrature signals are raised significantly at low GEM-3 transmit frequencies. It is thought that this is a result of voltages induced in the receive coil by vibrating motion in the earth’s magnetic field. At high GEM-3 frequencies, the quadrature signal reduces to stationary levels; the in-phase response stays high and flat. The in-phase noise is possibly due to motion relative to the magnetic soil and/or flexing of the coil head resulting in poor cancellation of the transmit field. The man-portable cart also has significant motion induced noise at low GEM-3 frequencies. While the frequency content of the cart motion is lower than the rail system, the amplitude of the motion is higher. The cart is also closer to the ground than the rail system. At high GEM-3 frequencies, both the quadrature and in-phase are responding to height changes relative to the ground. The lowest motion induced noise was found on the towed platform.

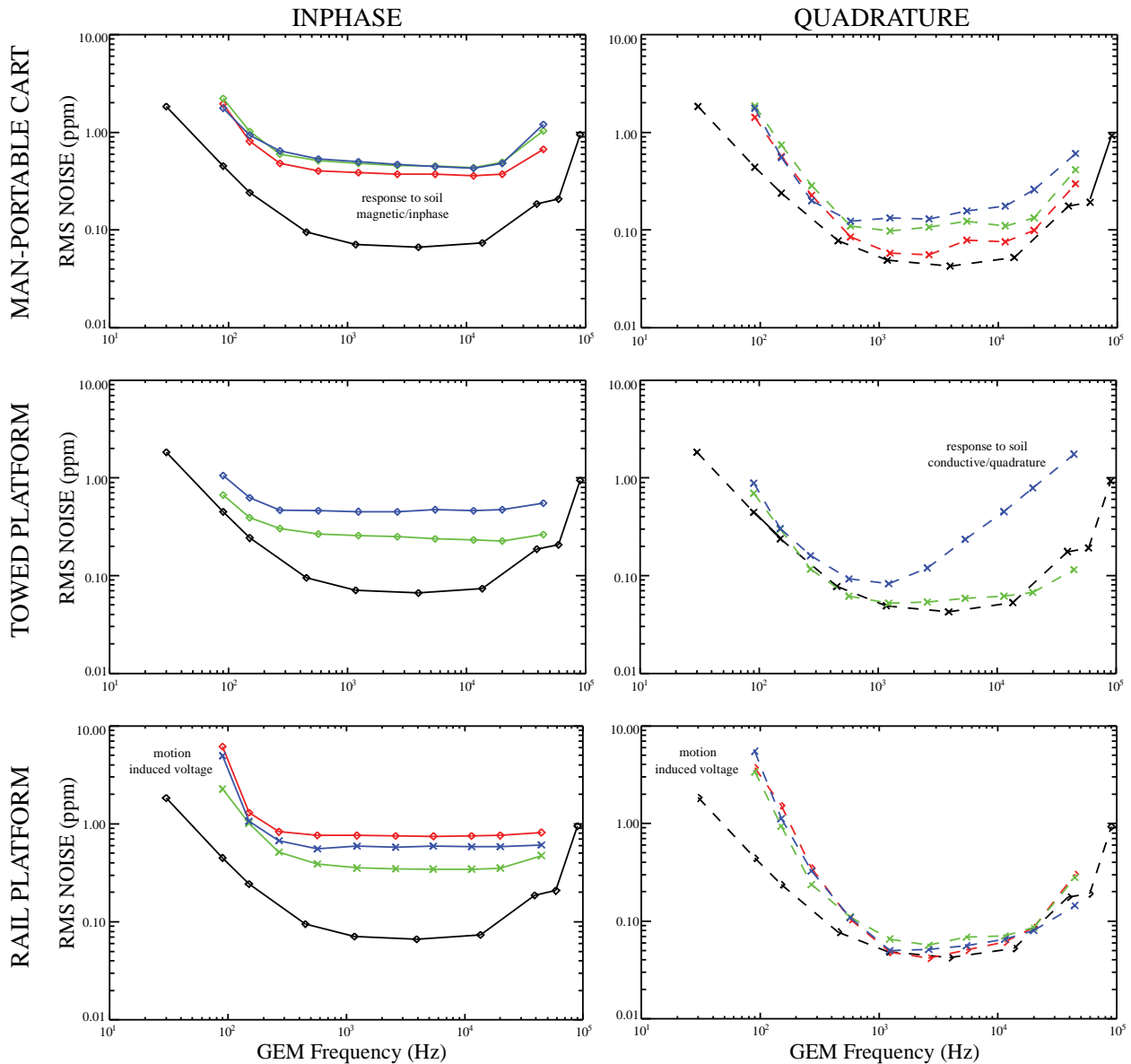


Figure 3-35 – GEM-3 RMS Noise (In-phase and Quadrature) by platform. The black curves are the stationary noise levels. The curves for each site are color-coded: Environmental – red, L Range – green, and Boat Launch – blue.

In an effort to better understand noise induced by motion in the earth's field, the GEM-3 was placed high on a test stand and moved in a controlled fashion. The sensor was placed at the end of a long board that could be pivoted off the edge of the test stand. The board was aligned along magnetic north. An IMU (Crossbow IMU-400) with a higher data rate (130 Hz) and a wider bandwidth (3dB roll-off at 30 Hz for angular rates) was attached to the board. The GEM-3 was set to collect data at 30 Hz. With both GEM-3 and IMU running, data was collected with the board stationary, pitching slowly, faster, and fastest. Figure 3-36 presents the IMU measured angular pitch rate,  $\omega_y$ , the in-phase response at 90 Hz and the quadrature response at 90 Hz. At the slow pitch rate, there was no measurable GEM-3 response. The response increased with pitch rate.

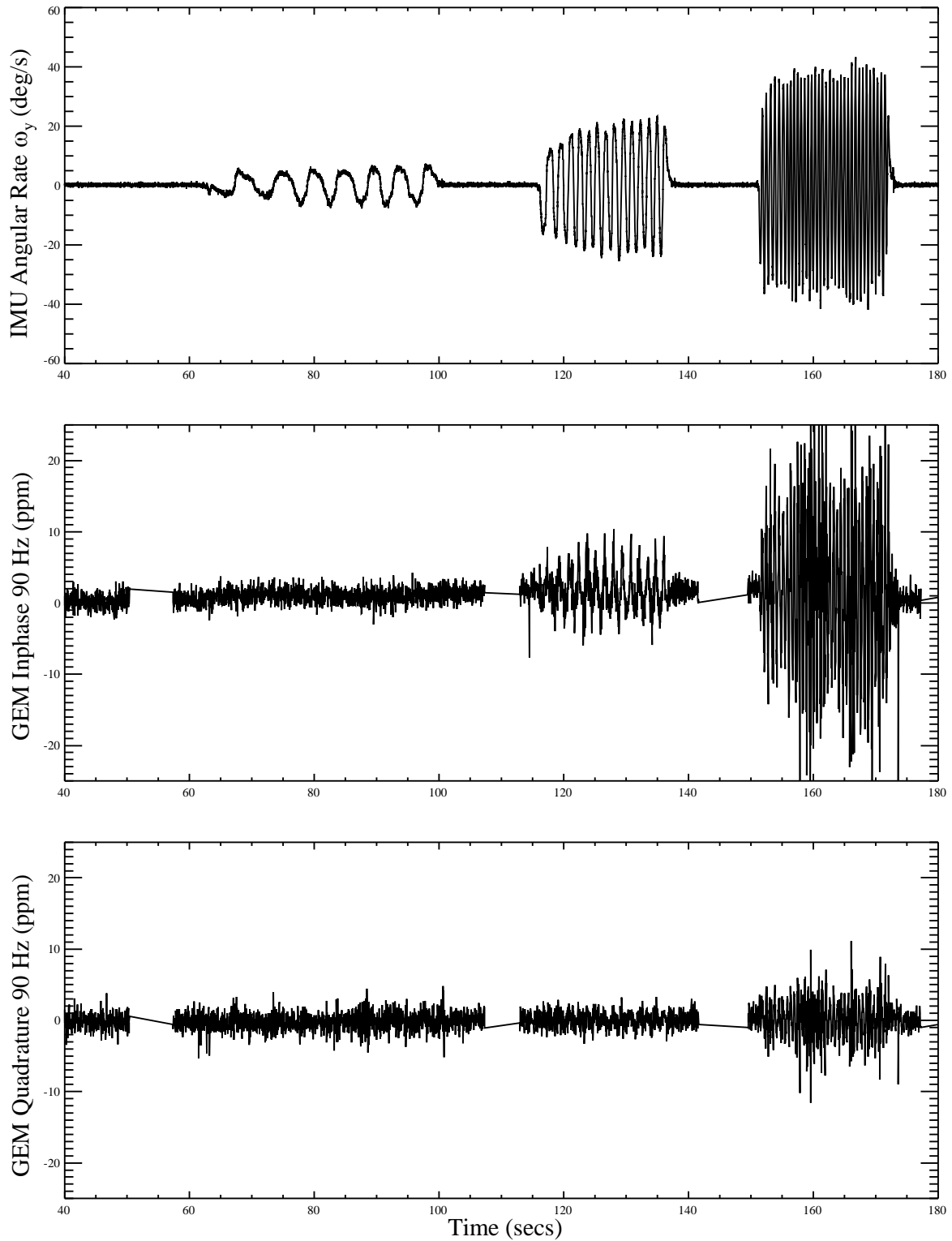


Figure 3-36 – IMU angular pitch rate versus the 90-Hz GEM-3 Response (In-phase and Quadrature)

From the IMU measurements, it should be possible to calculate the expected GEM-3 response. The voltage induced in the receive coil as a function of time equals the time rate of change of the

magnetic field going through the receive coil. Given this voltage as a function of time, one can divide it into  $1/30^{\text{th}}$  of a second base periods and convolve it with the sine and cosine of the GEM-3 transmit frequencies. With a rough idea of the GEM-3 A/D conversion of volts into ppm, the actual GEM-3 response can be predicted from the IMU measurements.

For calculating the induced voltage in a receive coil with N turns,

$$V(t) = -N \int_A \vec{B}_E^e \cdot \frac{d}{dt} \hat{n}^e(t) da ,$$

where  $\vec{B}_E^e$  is the earth's field and  $\hat{n}^e$  is the normal unit vector of the coil, both in the earth reference frame. Assuming a uniform field across the coil, this can be written out in terms of orientation angles (roll- $\psi$ , pitch- $\theta$ , yaw- $\phi$ ), angular rates ( $\omega_x, \omega_y, \omega_z$ ), and the components of the earth's field. For the simplified case of a coil pitching in the north-south direction, this can be written as:

$$V(t) = NA\omega_y [B_y \cos(\theta) - B_z \sin(\theta)],$$

where north is along the y axis, ( $B_y, B_z$ ) are the Cartesian components of the earth's field,  $\theta$  is the pitch angle, and  $\omega_y$  is the pitch rate. In general, the expression involves all three B components, all three angles and the roll/pitch rates.

Given  $V(t)$ , the GEM-3 response for transmit frequency  $\omega$  is given by convolving it with  $\sin(\omega t)$  for in-phase and  $\cos(\omega t)$  for quadrature over the GEM-3 base period of  $1/30^{\text{th}}$  of a second. For this short time scale, the induced voltage is to first order a linear function over the base period. The result is the integration of  $t \times \sin(\omega t)$  or  $t \times \cos(\omega t)$  over an integral number of transmit periods. The first integration produces a non-zero solution and the second solution is zero. The result to first order should be a large amount of sensor noise in the in-phase and a small amount in quadrature. This was not observed; some part of the induced voltage noise always leaked into the other channel. The manufacturer indicates that all of the noise should be in the quadrature response. After making measurements to convert voltages into ppm and accounting for other aspects of the GEM-3, the mixture of motion noise could not be adequately accounted for. To match the measured GEM-3 response from simple pitching motion, the voltage integration required an arbitrary phase shift of the form  $V(t) \times \sin(\omega t + \phi)$  or  $V(t) \times \cos(\omega t + \phi)$  where  $\phi$  is a fixed phase shift of the transmit wave form relative to the measured base period. For the pitching experiment, a shift on the order of  $\pi/5$  radians was needed. Given this extra phase shift, the IMU measured motion can be used to closely model the measured GEM-3 response. Figure 3-37 plots the results from the pitching experiment. The black curve is the measured GEM-3 response and the red curve is the response calculated from the IMU motion. With the phase shift, the in-phase and quadrature measurements could be closely matched at low GEM-3 transmit frequencies. At higher frequencies, the noise continued to decrease as expected for the quadrature, but the in-phase noise leveled out. It is thought that this residual noise maybe associated with flexing in the sensor coil head. Figure 3-38 plots average noise levels over three second intervals as a function of GEM-3 transmit frequency. The black curve is for rapid pitching, red curve for medium pitching, the blue curve is for slow pitching, and the green is stationary noise. For rapid motion in the earth's field, the noise for in-phase and quadrature scale roughly to the negative two power with transmit frequency. At GEM frequencies of 1 kHz, this noise becomes negligible relative to

the sensor's inherent noise. As noted above, the in-phase noise levels appear to level off above 1 kHz.

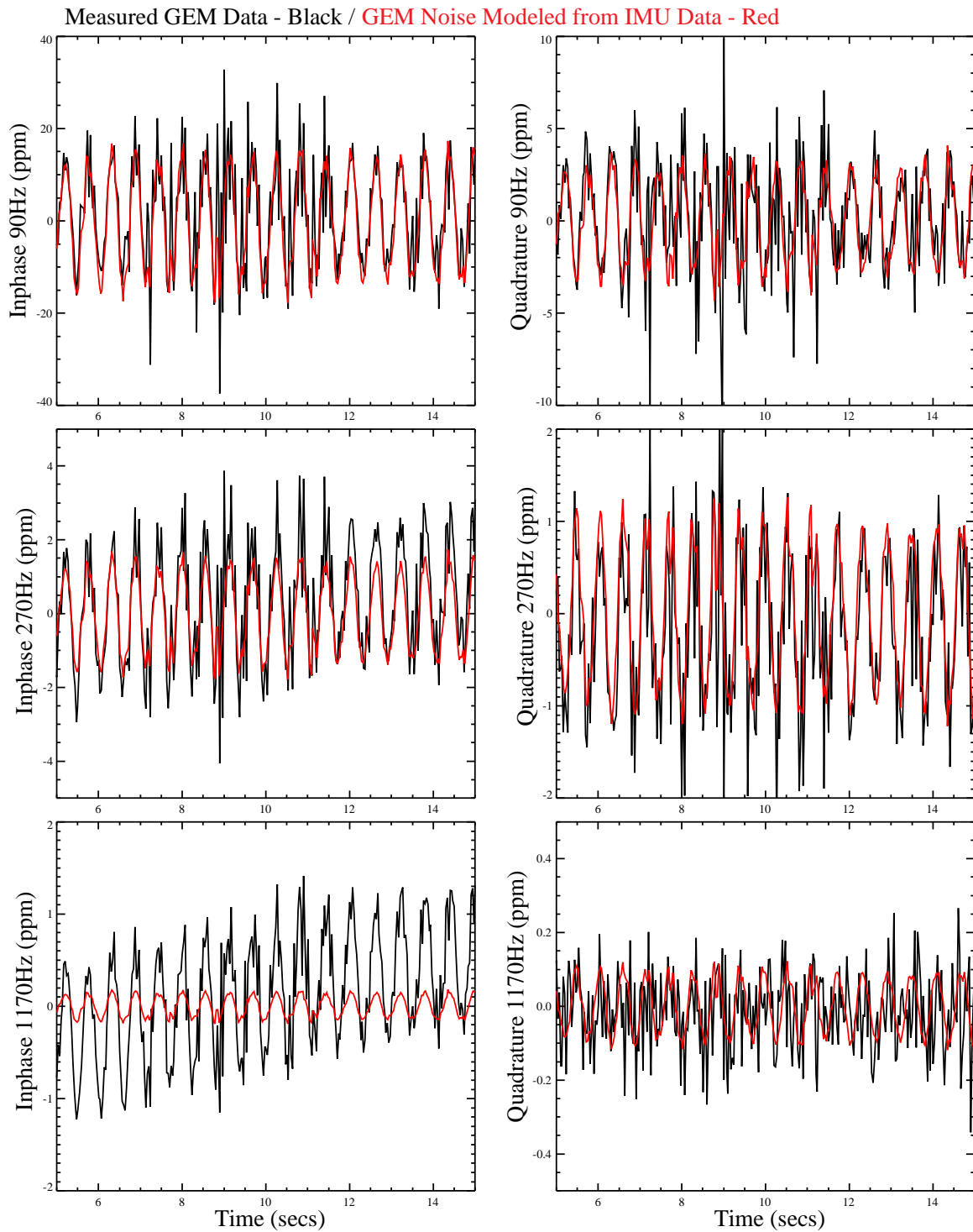


Figure 3-37 – GEM-3 Response – Measured versus IMU-based Model for Noise. Experimental data are shown in black, modeled noise based on IMU data is shown in red.



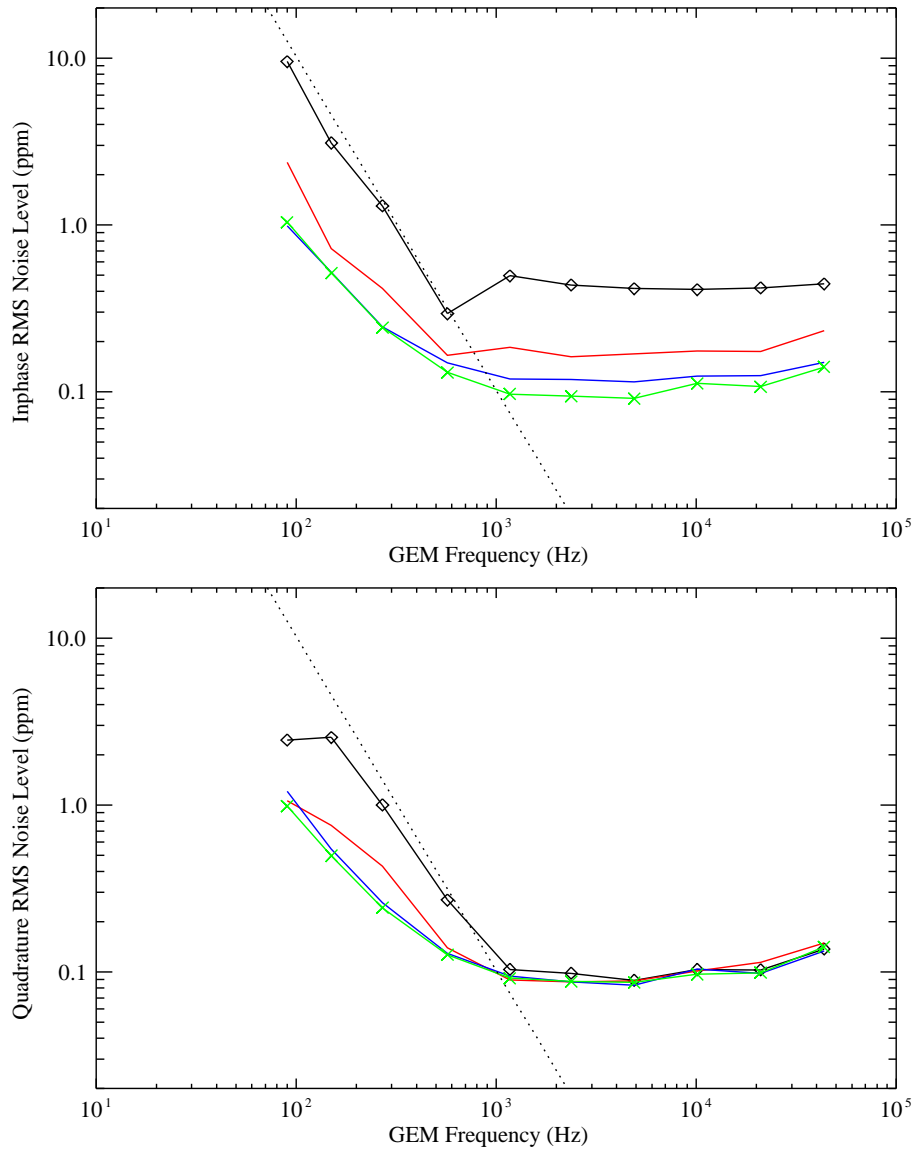


Figure 3-38 – GEM-3 RMS Noise Levels as a Function of Transmit Frequency. The measured noise levels are shown as the solid lines and symbols (black – rapid pitching, red – medium pitching, blue – slow pitching, green – stationary). The dotted lines represent the expected scaling of the dB/dt noise with transmitter frequency.

The GPS and IMU measurements made at each site can be used to estimate the relative contributions of motion induced noise. While the GPS positions are only good to a few centimeters, the IMU angles are only good to several degrees, and the bandwidth doesn't capture higher frequency motion, this should be sufficient to calculate the noise expected and compare it to what was measured. An example from the man-portable cart moving along track at the Environmental Area follows. The GPS heading, the IMU angles and angular rates plus an estimate of the Earth's field vector were used to calculate the noise contribution caused by induced voltage in the receive coil. Ground signal strength was based on the measurements and modeling done in Section 3.7.3. Changes in the coil's position relative to ground are needed to calculate the "soil" noise. Exact changes would require measuring height above ground (GPS Z

measures height relative to the GPS ellipsoid), coil orientation, and ground orientation (in the case of sloped ground). The Blossom Point sites are relatively flat. The pitching of the cart probably accounts for much of the changing sensor height above ground. Since the GPS antenna is pitching along with the coil on the cart, it was decided to use GPS Z as a rough estimate of sensor height above ground. Figure 3-39 plots curves of measured and calculated GEM-3 noise at low GEM-3 transmitter frequencies. The black curves are in-phase and the red are quadrature. The noise in this range is dominated by induced voltages. No attempt was made in the calculated noise to account for the apparent phase shift in the GEM-3 convolution described above. Because of this, all of the modeled noise is in the in-phase channel, when some it should actually be mixed into the quadrature. In amplitude and rough characteristics, the calculated noise comes close to what was measured. Figure 3-40 plots the noise from the high GEM-3 transmit frequencies. The modeled signal is dominated by motion relative to the ground. The in-phase soil signal is constant with frequency from the soil's magnetic susceptibility. The quadrature soil signal increases with frequency due to the soil conductivity. The measured noise has these basic characteristics, but at its highest transmit frequency, the GEM-3 appears to be mixing the in-phase and quadrature signals. In Figure 3-41, the 3 second averaged noise is plotted for this data set. The black curves are the measured GEM-3 data. The red curve is the voltage induced noise calculated from the IMU measurements. The green curve plots the noise from estimated motion relative to ground. These two sources of motion related noise seem to account for the noise seen by the GEM on the man-portable cart.

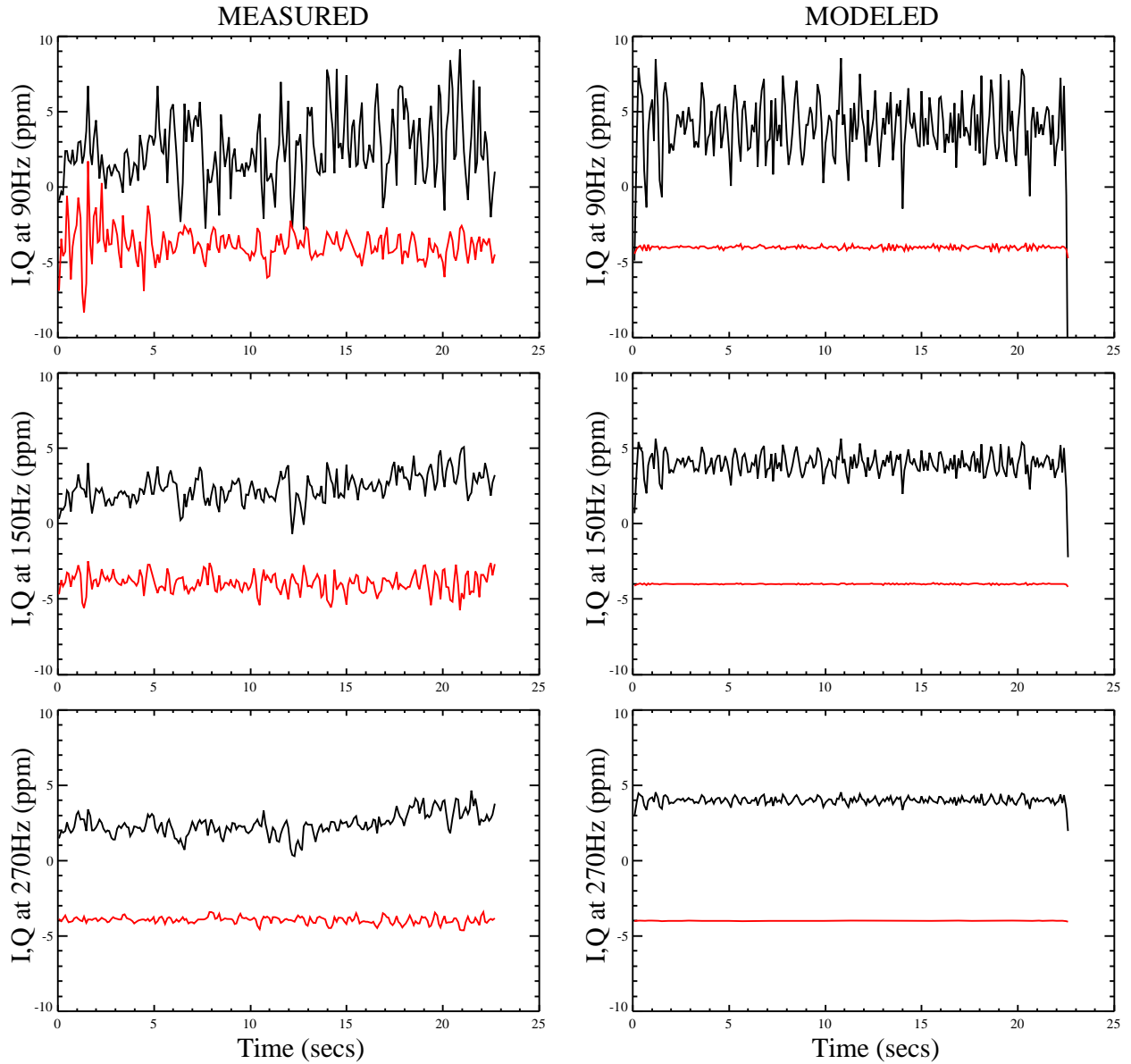


Figure 3-39 – Measured GEM-3 Noise and Modeled Noise for the Lower Transmitter Frequencies. The left-hand panels show the experimental data and the right-hand panels show the modeled results. The in-phase and quadrature responses are colored black and red, respectively.

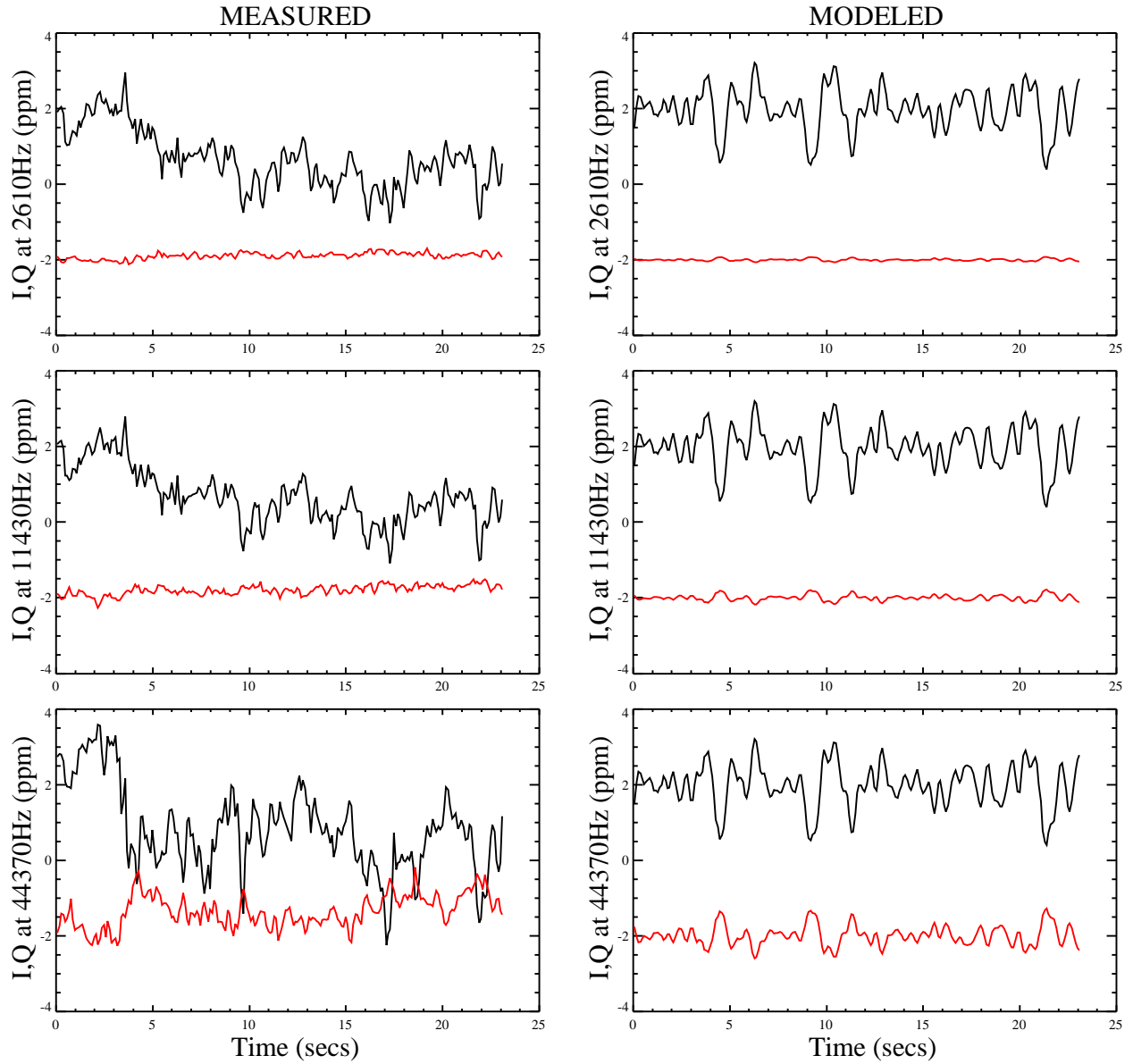


Figure 3-40 – Measured GEM-3 Noise and Modeled Noise for the Upper Transmitter Frequencies. . The left-hand panels show the experimental data and the right-hand panels show the modeled results. The in-phase and quadrature responses are colored black and red, respectively.

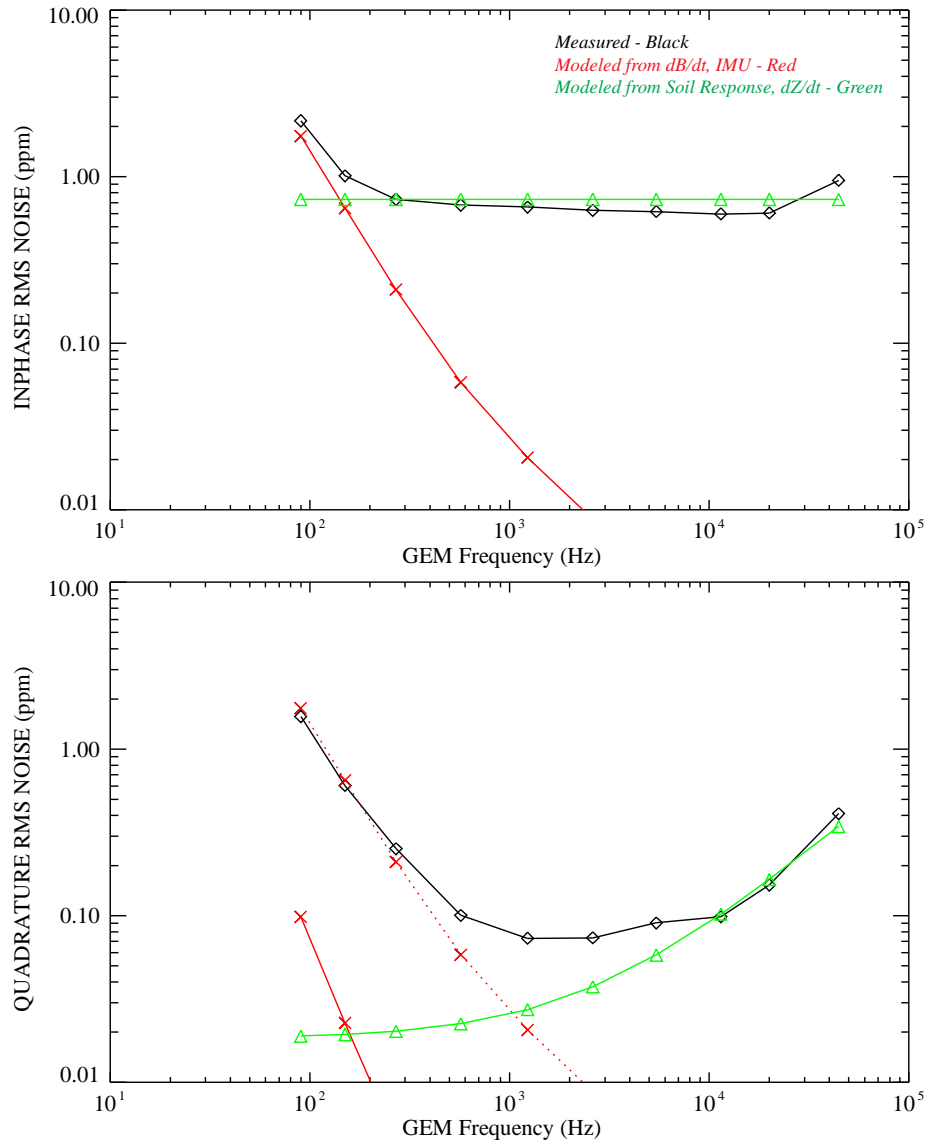


Figure 3-41 – Three-Second Average RMS Noise for the GEM-3 Response and Models. The measured noise (black), modeled noise from  $dB/dt$  (red), and modeled noise from estimate motion relative to the ground (green) are shown. The  $dB/dt$  model from the upper panel is shown in the lower panel a dashed red line as a reference.

### 3.8 Analysis of the EM61 MkII Data

This section presents the analysis of the data collected for the EM61 MkII time-domain EMI geophysical instrument. Some additional data collection was conducted with the EM61 MkII sensor after the field work was completed. These measurements were made based on issues which arose during the data analysis effort. These additional measurements will be presented in the course of the following analyses.

Testing was done with several different sets of electronics packages and coil sets. Coil sets owned by NAEVA Geophysics and NRL were used (S/N's 0418, 0530, and 0201). Electronics packages owned by NAEVA Geophysics, NRL, and SAIC were tested (S/N's 022024, 011839-3, 011812-3). For the measurements made after the conclusion of the main demonstration, LabView code written by SAIC was used to collect the data in a manner similar to that of the NRL software.

#### 3.8.1 Sensor Variability

The EM61 MkII is the *de facto* standard commercial instrument used in UXO surveying. A large number of them have been both purchased and made available for rental. The question arises as to how carefully they are calibrated and how consistent their response will be to a given UXO item. To test this, two sets of electronics and two sets of coils were used to take a set of controlled measurements for comparison.

Figure 3-42 presents the results of two different sets of EM61 MkII electronics attached to the same set of coils. The coils were kept stationary. For each set of electronics, a standard 2" diameter steel ball was repeatedly placed and removed from a fixed location a few centimeters from the bottom coil. Data was collected using the NRL software. The top graph shows the measured transmit current as reported by each set of electronics (one set in black, the other in red). The standard transmit current is 3000 and the final voltage outputs are scaled by the ratio of the standard transmit current to the measured current ( $3000/\text{Tx Current}$ ); as the current decreases, the signal is boosted. In both cases, the transmit current is slowly decaying as the battery discharges. The noise levels in the two measurements were comparable. Typically, the measured current would be smoothed over hundreds of samples before using it to normalize the final signal to remove any reported current transients. Each configuration shown used a different system battery and a different current magnitude was measured. ESTCP Project MM-0506, Performance Baseline of Geophysical Sensors: Detection Limits, Repeatability and Inter-Instrument Comparisons, further examines this issues for a range of fielded units. As part of their efforts, constant voltage power supplies are used to remove the effect of the battery.

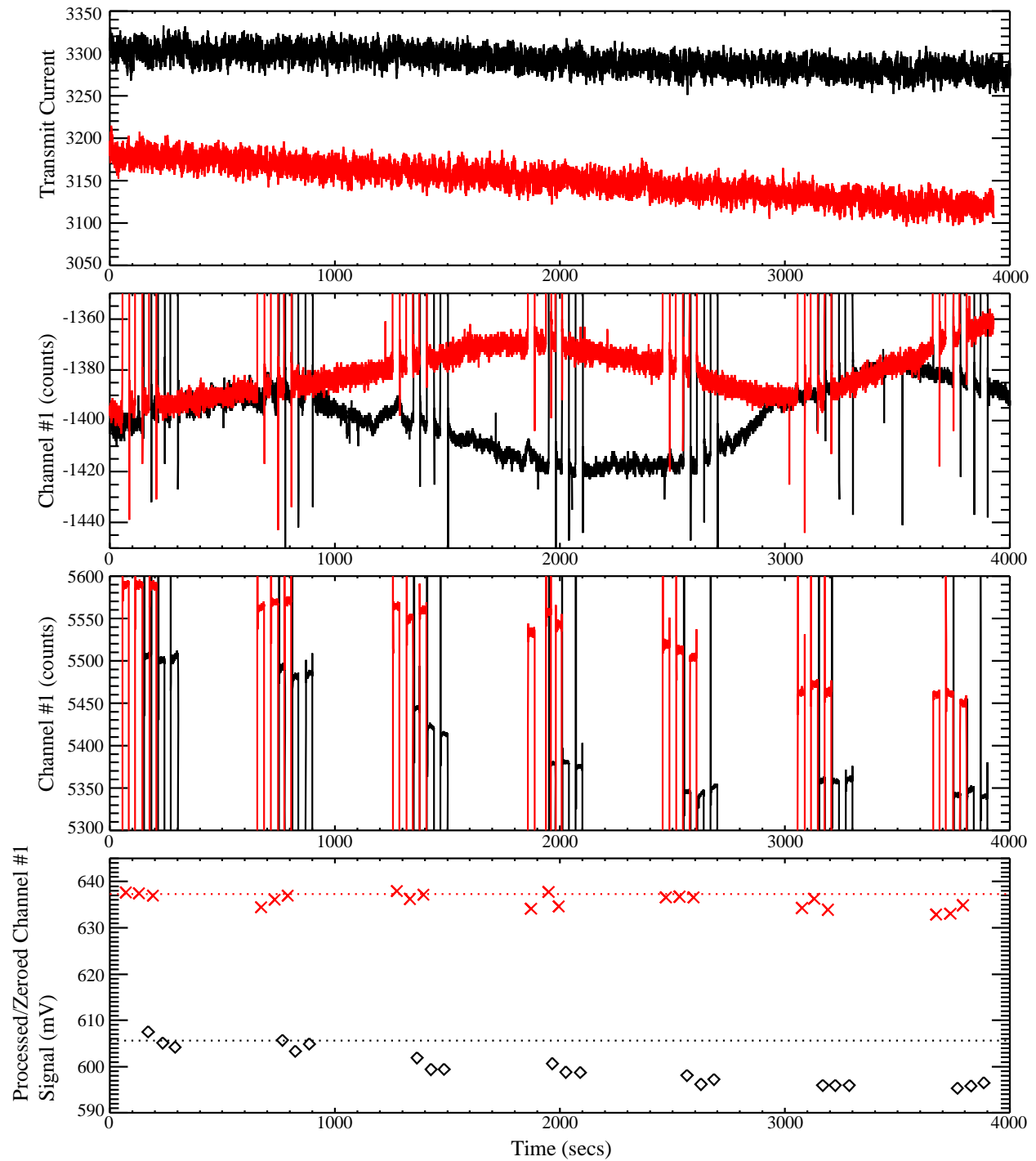


Figure 3-42 – Comparison of Response from Two EM61 MkII Electronics Packages. The response from one set of electronics is shown in red, one in black. The same set of coils were used for both measurements.

The next graph plots the counts recorded by channel #1 (lower coil, earliest time gate). This plot focuses on the zero level measured when the sphere is not present. The counts recorded as zero signal level is obviously not near zero and drifts over time. The two sets of electronics measured comparable zero levels and had similar drift rates. The third plot shows counts when the sphere is present. Despite having a lower measured transmit current, the electronics plotted in red has a larger count level when the sphere is present. The last plot applies the necessary instrument gain factors, normalizes by current, and subtracts the drifting background off of the signal levels. The red set shows a fairly consistent response around 637 mV. The black set is slowly decreasing in amplitude despite the current correction. It is also off in amplitude from the other sensor. The differences are on the order of 5 to 10%. Most of this difference appears to be in the measured current.

Figure 3-43 plots the results of measuring four different objects with four different combinations of electronics and coils. The results plotted are for the three time gates on the lower coil. The measurements were taken by placing the object in and out to subtract off any drifting, non-zero background. The data has been normalized by current and converted into the manufacturer's milliVolts. The X symbols are from one set of electronics and the diamonds from another. The solid lines indicate one coil set and the dotted lines another. There is a difference in amplitude between the two electronics comparable to what was seen in Figure 3-42. There is a smaller difference in amplitude and time decay rates between the different coil combinations.

Figure 3-44 plots the temporal response of the four electronics/coil combinations. The EM61 MkII response to a step function can be measured with a circular loop of wire and a fast switch. By opening and closing the switch every ten seconds, the on/off sensor response to the circular loop can be recorded. The two symbols represent different electronics packages, the two line types represent different coils. Each case has been lined up in time with the wire loop circuit being opened at  $t = -0.3$  seconds. The EM61 MkII output does not reach zero until  $t = 0.4$  seconds. The data was collected using the Geonic's DOS-based data logger software. The timing of the data is only good to roughly 50 milliseconds. To within this timing accuracy, the four combinations appear to have very similar temporal responses. To first order, this temporal response fits the equation and values provided by the manufacturer discussed in Section 2.1.1.1.



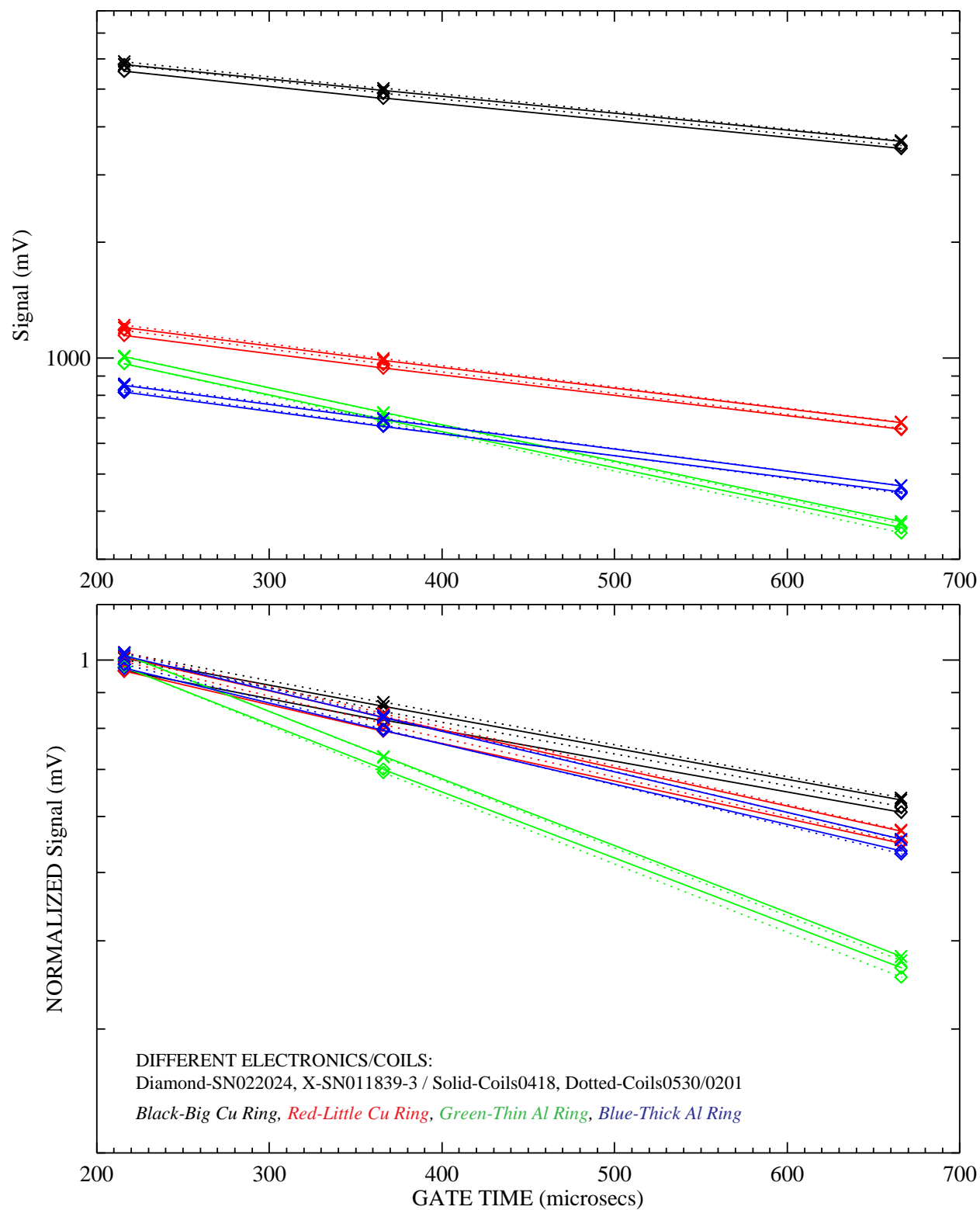


Figure 3-43 – Comparison of Response from EM61 MkII Electronics Packages and Two Sets of EM61 Coils to Several Standard Objects

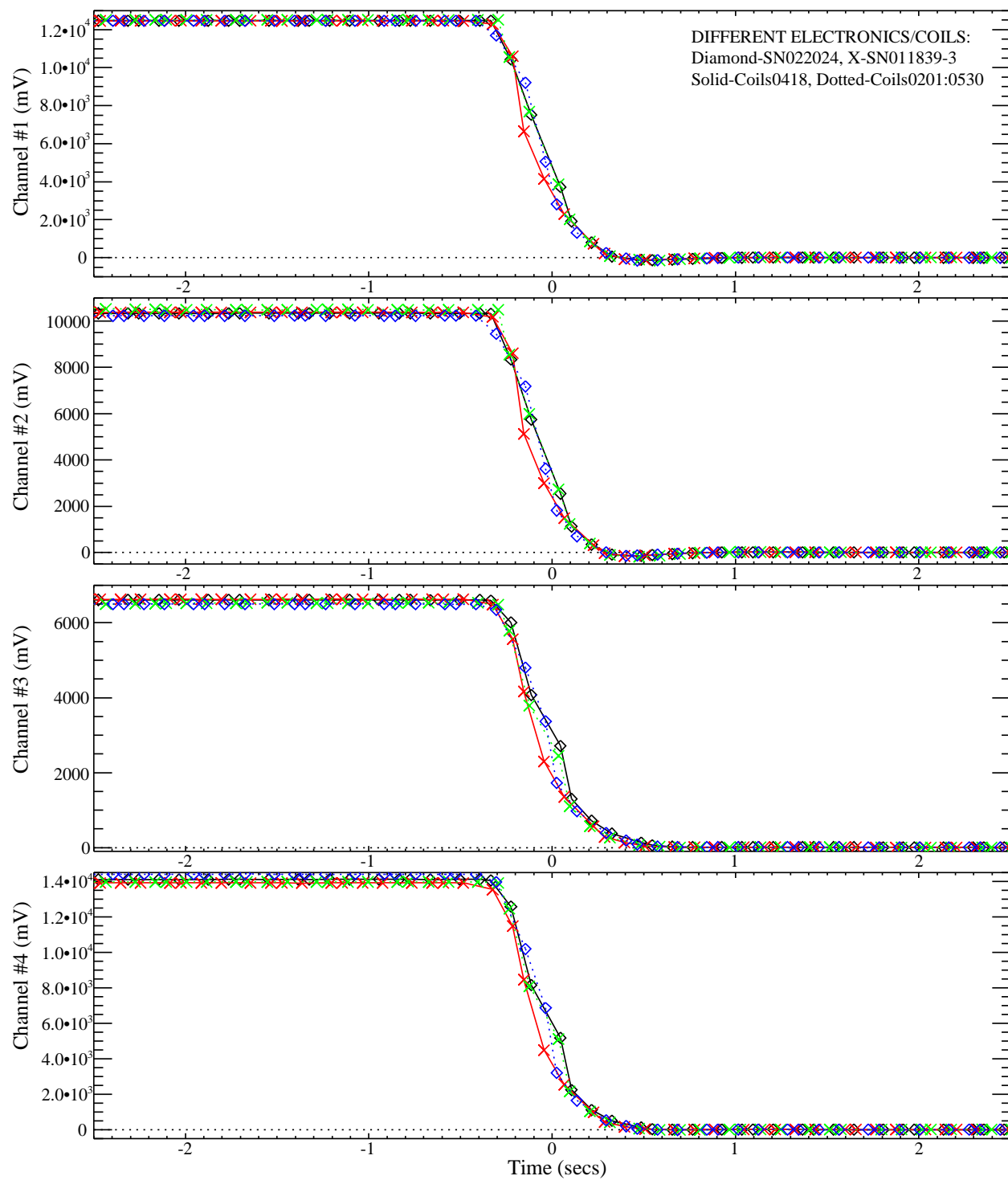


Figure 3-44 – Comparison of Time Response from Two EM61 MkII Electronics Packages and Two Sets of EM61 Coils using a Circular Loop of Wire and a Fast Switch

### 3.8.2 External Noise

Figure 3-45 plots the power spectra measured with the NRL low frequency spectrum analyzer discussed in Section 2.1.2. The three columns correspond to the three sites at Blossom Point: the “L Range”, the “Boat Launch” area, and the “Environmental” area. The top row spectra are with the coil oriented on-edge facing north, the middle row on-edge facing west, and the bottom row with the coil laying flat. As with the passive GEM-3 measurements, 60 Hz and harmonics are present. There are also the VLF transmissions in the 20 kHz range. Unlike the GEM-3, there are a variety of lines from 100’s of Hz out to kHz. In particular, a large consistent line is present at 2 kHz. There is a broad feature around 50 kHz. The amplitude of these features is comparable to the 60 Hz and VLF features.

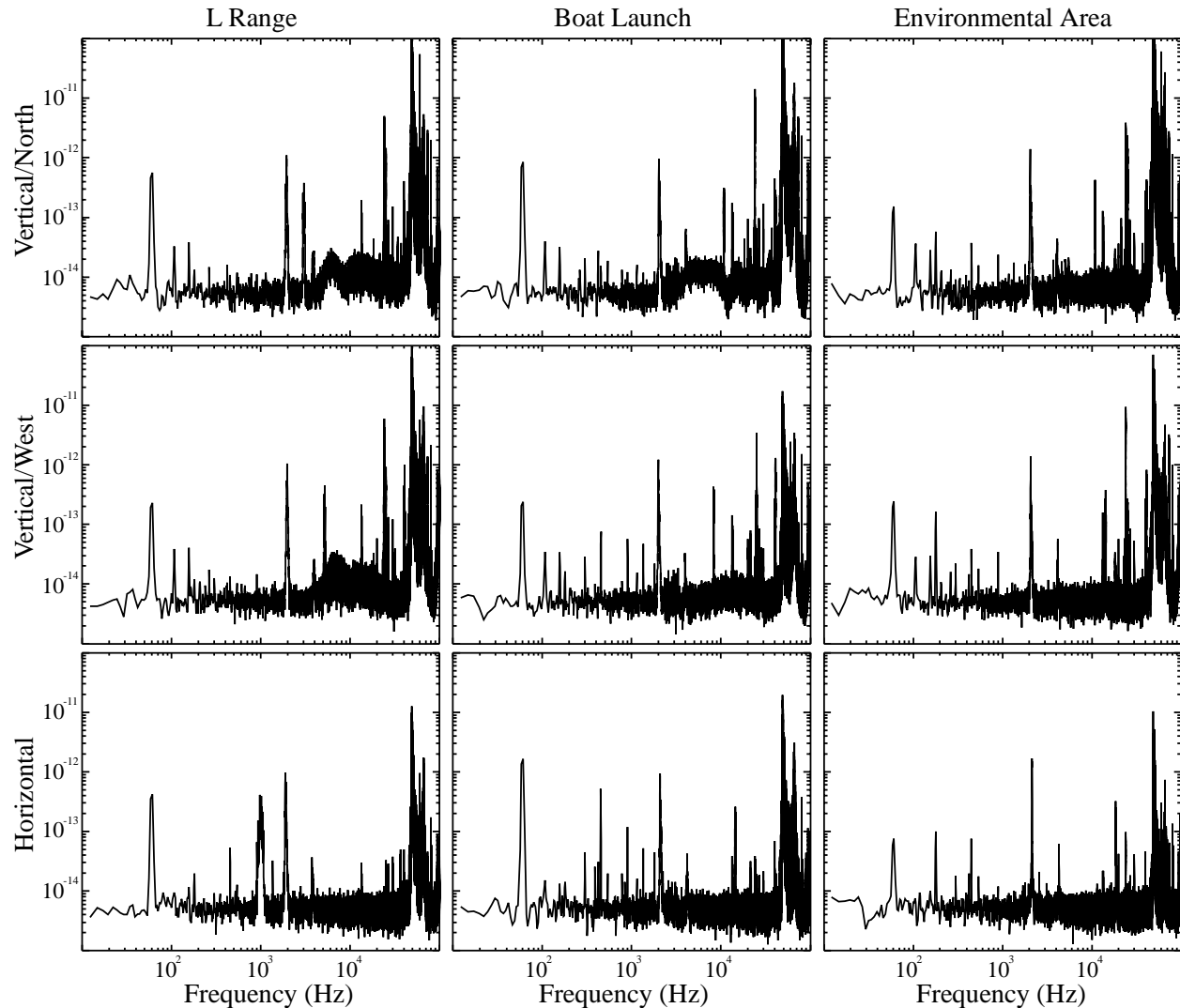


Figure 3-45 – External Noise Relative Power Spectra as a Function of Detector Orientation at the Test Sites

It is not clear if these noise sources are external to the spectrum analyzer. In future work this needs to be worked out. One test would be to run the passive GEM-3 sensor with and without the spectrum analyzer running nearby. Overall, these external voltage induced in the EM61 receive coils get gated and analog integrated with the long time constant. This effectively averages the external noise to very low levels.

### **3.8.3 Inherent Noise**

When placed in open fields away from power lines, the EM61 MkII measures very consistent low-level noise, consistent with the source being the sensor electronics. EM61 MkII data were collected with the sensor operating in Differential mode and using the NRL logging software at a rate of 10 samples per second. In Differential mode, the first three data channels sample time windows increasingly later in time for the receive coil. The fourth data channel samples the top coil at the last time window from the bottom coil. The data were normalized by the measured transmit current and multiplied by the standard gain factors to give units of “milliVolts”. Data were collected for over one hour with the sensor remaining stationary. Figure 3-46 plots averaged power spectra for each data channel. As was seen with the GEM-3, each data channel has a basic white noise level between frequencies of 0.1 to 10 Hz. At lower frequencies (longer time scales), the sensor output begins to exhibit drift. Above 1 Hz, the spectra roll off as determined by the appropriate time response. The red curves plot the power spectral response as determined by the sensor’s step response equation discussed in Section 2.1.1.1. The dotted line indicates the digitizer signal floor (bit level) of the sensor’s A/D electronics. The noise observed for the later time gates is not significantly above A/D digitizer signal floor. For the particular data sequence shown in Figure 3-46, there were unexpected peaks at several frequencies. These peaks were not always present and their cause is currently unknown.

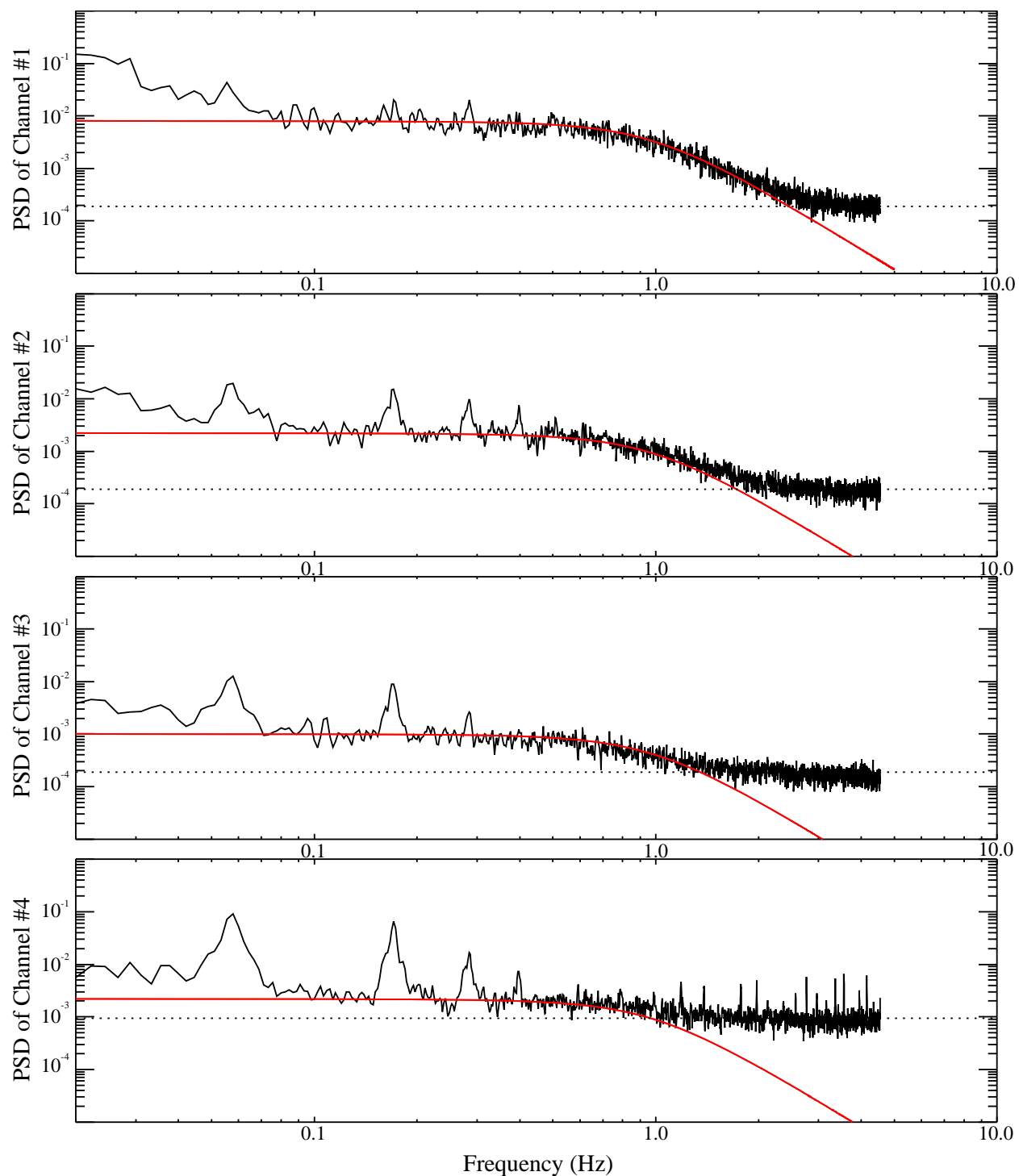


Figure 3-46 – Averaged Relative Power Spectra for a Stationary EM61 MkII in a Quiet Location. The dotted lines represent the channel-specific noise floor (bit level). The red curves plot the power spectral response as determined by the sensor's step response.

### 3.8.4 Geologic Response

For the time domain sensors, the EM61 MkII and the EM63, there was no significant response to the soil observed for the rail/tower heights used (see Section 2.2.4). During the data analysis effort, this observed lack of response was revisited by making additional measurements with the EM61 MkII placed almost directly on the ground surface. To account for the unavoidable drift in the sensor response, the coils were alternately placed high in the air on plastic shelves (~ 2.0 m AGL) and then close to the ground on a single shelf (~ 0.05 m AGL). Because of the coil size, cable lengths, and the presence of the electronics package and backpack, these measurements were somewhat unwieldy to conduct. Any future time-domain measurements will require a different protocol to collect soil response measurements at small height increments close to the ground. One possibility is to use the time domain sensor developed under ESTCP MM-0601 which has several advantages and is discussed further in Section 4.1.1.

Figure 3-47 plots the EM61 MkII results on the Blossom Point test field near the pit used for overlapping signature measurements. The sensor was in the four time gate mode (no upper coil). The symbol/curves plot the measured data at four different heights. The y-axis on the right side indicates the response in manufacturer units of “milli-volts”. The amplitude of the signal in the first gate is on the order of 10 mV with the sensor only 0.10 m off of the ground. It is not surprising that there was no measurable signal at the rail height of 0.4 to 0.5 m with the EM63.

While the soil model used for evaluating the GEM-3 response can be applied to time domain sensors, its application to the EM61 MkII or EM63 sensors is, numerically, more involved. Our approach was to model the rectangular transmit coil as a sum of  $m$  by  $n$  dipoles and sum the field from these dipoles over the area of the receive coil. The soil response to a dipole can be found in [11]. A real conductivity and the frequency dependent complex susceptibility equation were included in the calculations. The response was calculated in the frequency domain and convolved with the FFT of the EM61 transmit pulse to get the time decay curve. The model results for the EM61 MkII are plotted as dashed curves in Figure 3-47 and scaled as voltage induced in the receive coil on the left side of the figure. In general [8], it has been noted that the time domain response is sensitive to the frequency dependence of the magnetic susceptibility. Based on an empirical model of this frequency dependence, the EMI response of weakly magnetic soil to a step function is expected to fall off as  $t^{-1}$ . The EM61 MkII measured and modeled response shows a similar, but not exact, dependence. The numerically modeled response to soil conductivity (for the range of values measured by the GEM-3, 0.002 to 0.1 mho/m) result in levels not measurable by the sensor. The curves fall off as  $t^{-5/2}$  and are rapidly lost in the sensor noise.

At a later date, a single sensor was borrowed from the MTADS Discrimination Array and used to measure the soil response on the Blossom Point test field. The results are shown in Figure 3-48. The TEM sensor has a 0.1 s base period with a 50% (bipolar) transmitter duty cycle and produces a transmit waveform that is much closer to a step function than the EM61 MkII (0.013 s base period and 25% duty cycle). The single sensor TEM curves, both measured and modeled, closely follow a  $t^{-1}$  decay. The TEM sensor measures the soil response over a much wider range of time gates, from less than 0.1 milliseconds out to 25 milliseconds. The TEM sensor output is also calibrated to the current output of the transmitter coil during the transmitter ON time.

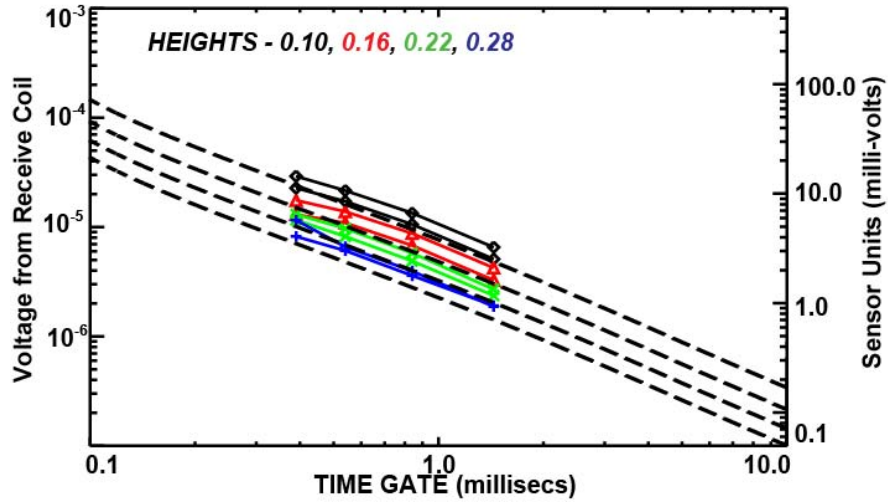


Figure 3-47 – Time-Domain Soil Response Measured using the EM61 MkII in 4-channel mode as a function of measurement height. The experimental data are shown as color-coded symbols and lines. The dashed lines represent the soil model discussed in the text as a function of sensor height.

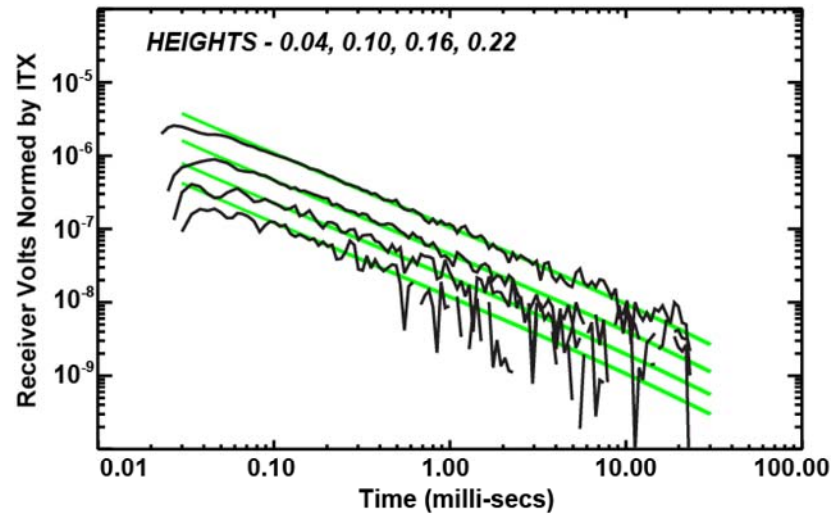


Figure 3-48 – Time-domain soil response measured and modeled using single sensor from MM-0601 TEM array as a function of measurement height. The black lines are the experimental data and the green lines represent the model results.

### 3.8.5 Motion-Induced Noise

The EM61 MkII was placed on the same platforms (MP cart, towed platform, and rail / tower system) as the GEM-3 and data were collected over the three sites at Blossom Point. The EM61 MkII was operated in Differential mode and sampled at 10 Hz. Data were collected and time stamped with the NRL data logging software. Cm-level GPS positioning at 10 Hz and IMU accelerations and angular rates at 20 Hz data were collected concurrently.

Figure 3-49 and Figure 3-50 show power spectra and time rasters from the EM61 MkII on the MP cart at the “Environmental Area”. The power spectra are averaged over a number of short segments. The lower PSDs in Figure 3-49 are from the IMU and show motion comparable to the GEM-3 on the MP cart (mostly pitching at a rate just under 2 Hz). The PSDs for the four EM61 MkII data channels show a peak at the same frequency as well as a significantly higher noise level across all frequencies. Like the noise spectra measured when the sensor was stationary, the PSD curves fall off as determined by the sensor’s dynamic time response and level off near the sensor’s measurement noise floor (bit level) at high frequency. The upper right graph in Figure 3-49 plots the correlation spectra between the EM61 MkII data channels. Unlike the stationary measurements, there is a modest correlation in the noise between the data channels. Figure 3-50 shows a sample time raster of the data measured over one pass of the cart for each data channel. The large peaks are from metal objects present in the ground. On short time scales (several seconds), the noise level for the first time gate is on the order of 1-2 mV peak-to-peak and the later gates are smaller in amplitude.



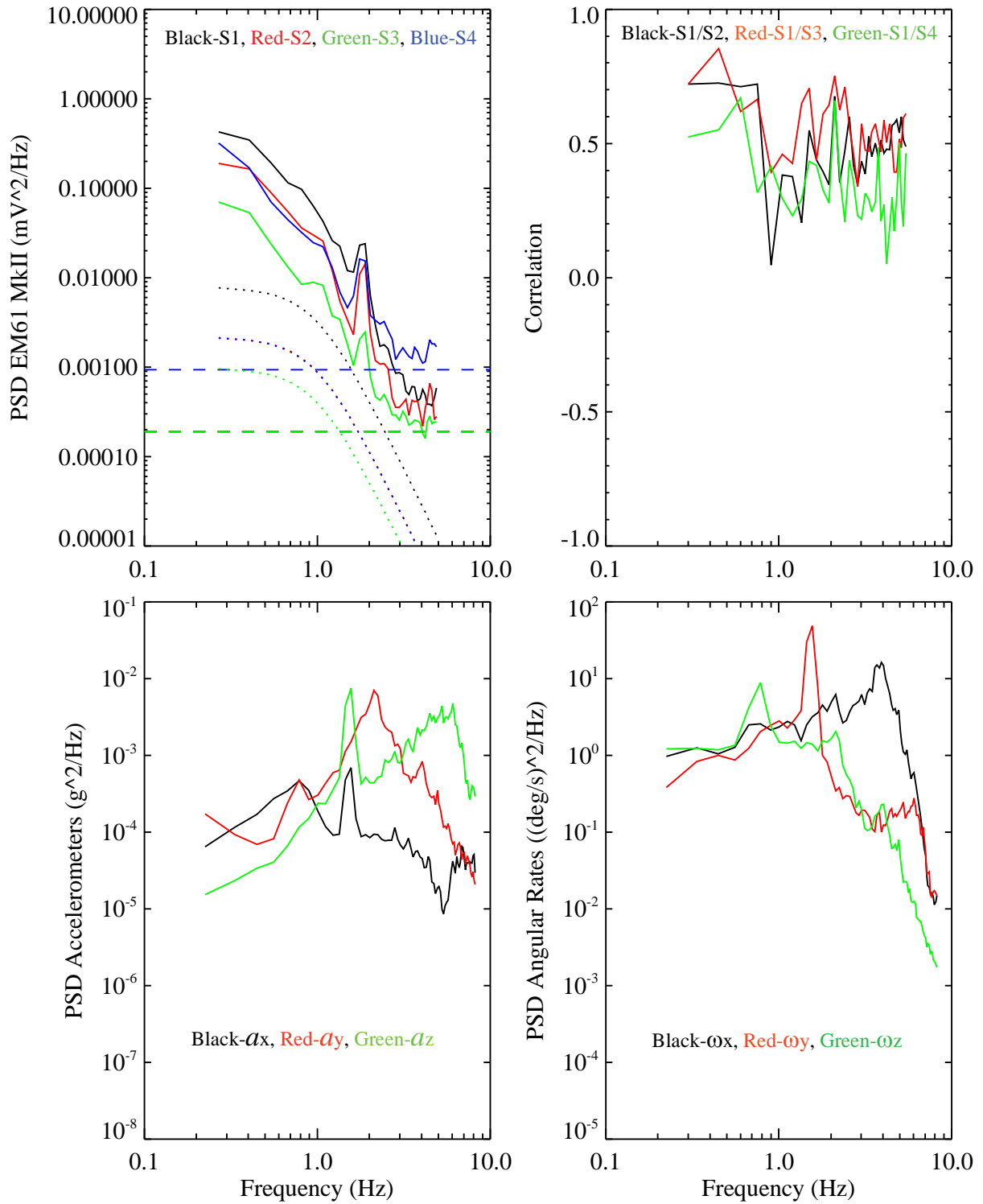


Figure 3-49 – Power and Correlation Spectra for the EM61 MkII / MP Cart Combination at the Environmental Area versus IMU Data. The color-coded dashed lines in the upper-left panel are the time gate-specific bit-level noise for the sensor as found in Figure 3-46. The color-coded dotted lines in the upper-left panel are the time gate-specific stationary noise due to the sensor's time response function as found in Figure 3-46.

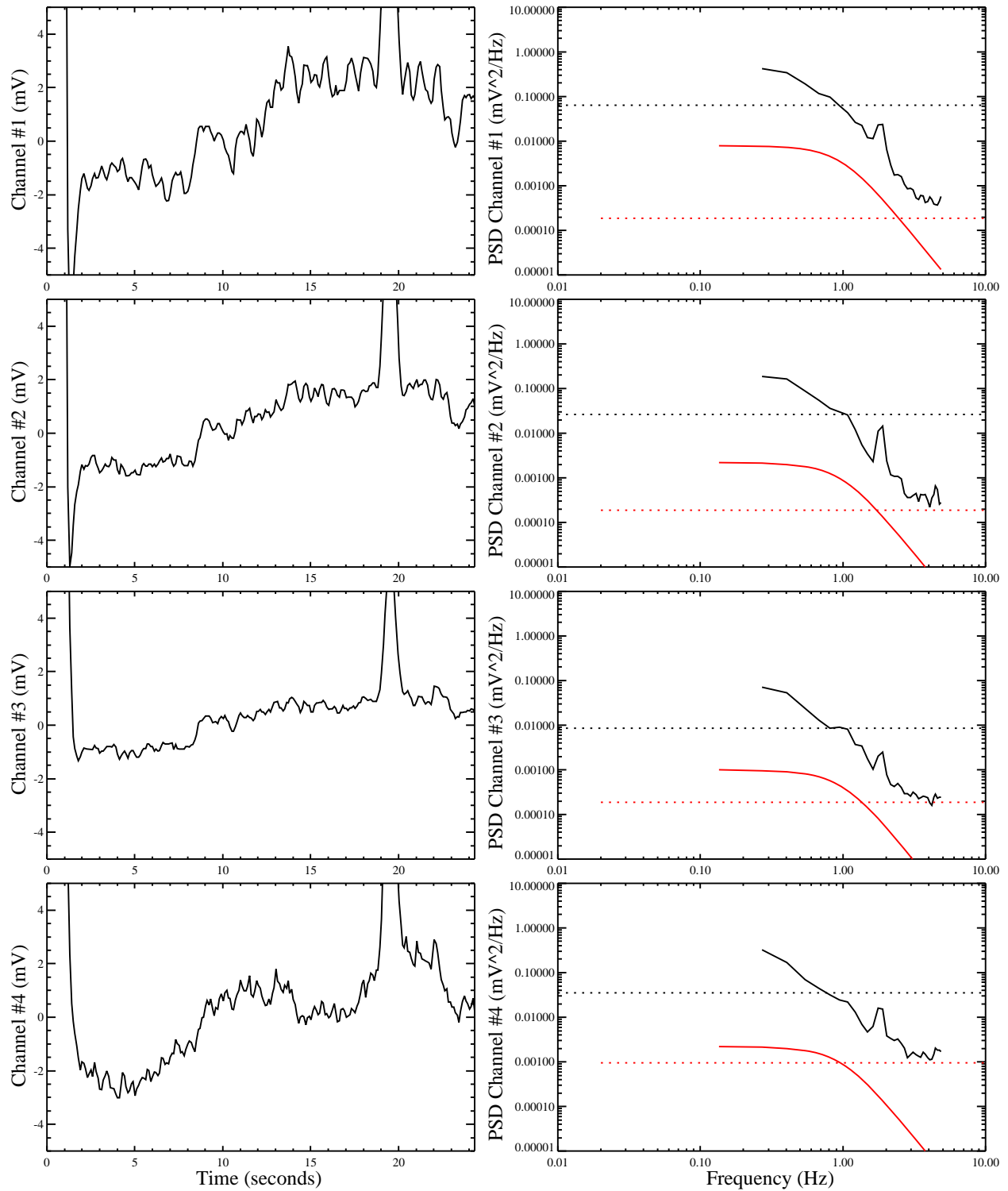


Figure 3-50 – Time Rasters (left) and Power Spectra (right) for the EM61 MkII / MP Cart Combination at the Environmental Area. The red-dotted lines in the right-hand panels are the time gate-specific bit-level noise for the sensor as found in Figure 3-46. The black-dotted lines are the rms noise levels calculated on short time scales.

Figure 3-51 and Figure 3-52 plot the same analysis for the towed platform. Again, the IMU measurements show the same motion as measured with the GEM-3. The motion is reduced in amplitude and the spectra are broader. The EM61 MkII noise spectra are also lower than those made on the MP cart and exhibit no distinct spectral features. The correlation between data channels is also weak. The single pass time rasters shown in Figure 3-52 exhibit short scale variation on the order of 0.5 mV and the third data channel has almost no discernable noise.

As shown in Figure 3-53 and Figure 3-54, the rail and tower system provided a significantly higher noise level environment than was intended. The EM61 MkII mounted on the tower pitched at a high frequency as it moved down the rail bed and produced very high levels of noise. The EM61 MkII power spectra showed no distinct features, and exhibited the usual sensor response roll-off behavior. The measured noise levels in the lower coil data channels were highly correlated across all three time gates. The lower coil data channels were not correlated with the upper coil data channel. The measured noise level in the EM61 MkII was on the order of 4 mV, peak-to-peak.

As an overall comparison, short scale standard deviations were calculated for each EM61 MkII channel on each platform at each site. The upper plots in Figure 3-55 are from the rail platform on each of the three sites. The noise levels range from 1 to over 2 mV. When the tower was moved faster, the noise level increased. The lower three plots show the noise levels from the MP cart, the towed platform, and with the sensor stationary. The noise levels on the MP cart and towed platform decrease with the first three time gates. The upper coil/third time gate has larger noise levels than the lower coil/third gate due to more turns in the coil and possibly due to more motion related noise. The MP cart RMS noise level was greater than that for the towed platform. The L Range and Environmental Areas exhibited similar noise amplitudes, but the RMS noise level for the Boat Launch was significantly greater.

As with the GEM-3, there are two dominant sources of motion-related noise, voltages induced by the receiver coil moving in the earth's field and voltages induced by motion of the sensor relative to the ground. The same equations can be used to calculate the voltage induced in the EM61 MkII receive coils from the measured IMU roll, pitch, and angular rates. See the discussion in Section 3.7.4 for further details. The voltage calculated from the motion measured by the IMU would then be time gated to the EM61's time gates and integrated using the sensor's dynamic response function. As long as this voltage changes on time scales greater than the sensor's pulse rate (75 Hz), all of the time gates will sample the exact same noise. Because of the sensor's response function, the measured voltage will be shifted in time. At higher frequencies, the measured voltage will also be reduced in amplitude.

A series of measurements were designed to characterize the influence of motion on the measured signal for the EM61 MkII and to calibrate the modeled voltage induced in the receiver coil into the sensor's units of milliVolts. The EM61 MkII was pitched in a controlled fashion while positioned high above the ground ( $> 2$  m). The SAIC Labview procedure was used to collect data from the EM61 MkII data and the Crossbow IMU, references to a common PC clock. The Crossbow IMU (IMU-400) was used in place of the VG-300 unit because of its larger bandwidth for both angular rates and accelerations (3dB at 25 Hz and 75 Hz). The Labview routine was written to capture the IMU data at its full data rate (130 samples per second). The sensor was aligned approximately with magnetic north and pitched at varying rates.

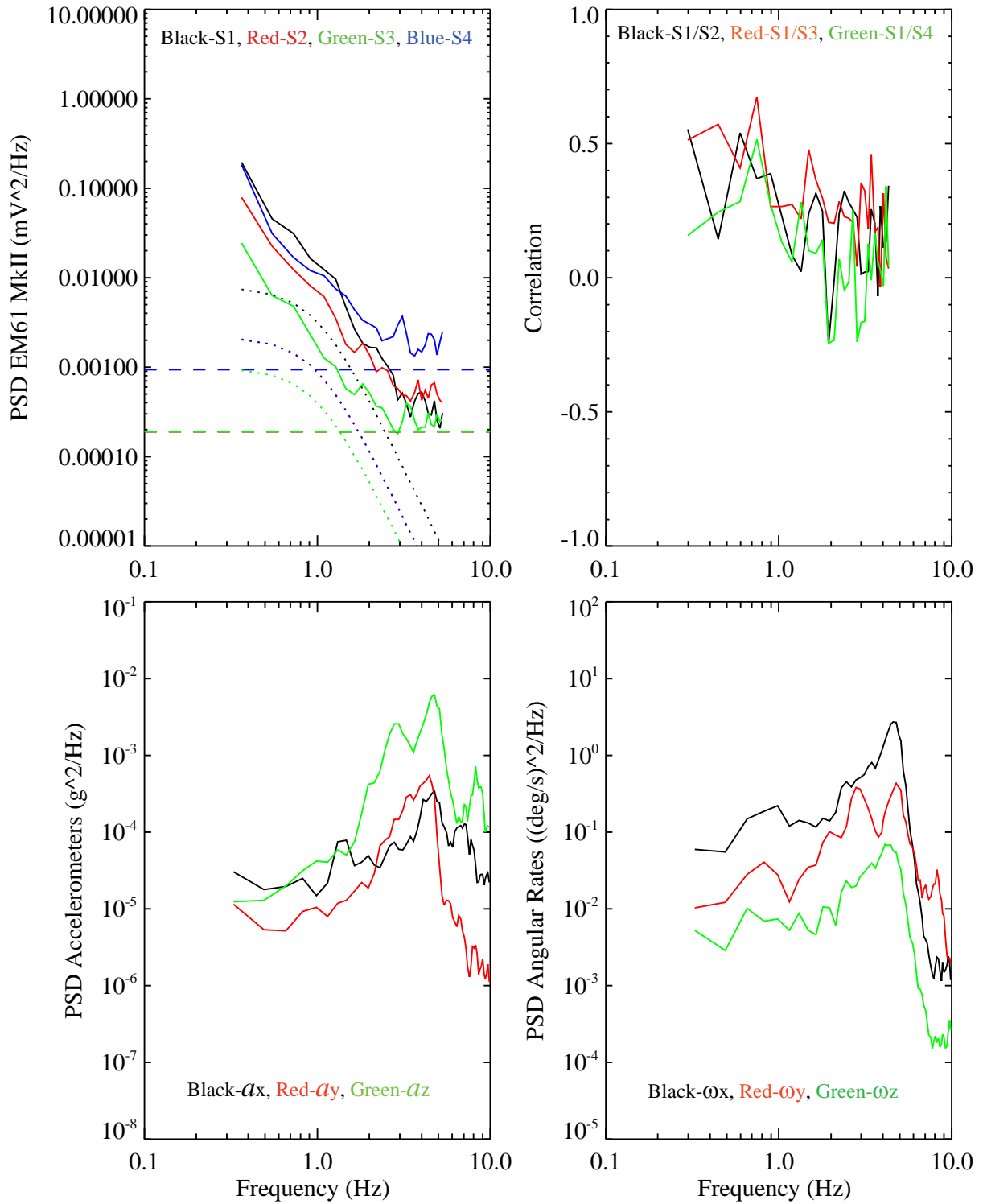


Figure 3-51 – Power and Correlation Spectra for the EM61 MkII / Towed Platform Combination at the Environmental Area versus IMU Data. The color-coded dashed lines in the upper-left panel are the time gate-specific bit-level noise for the sensor as found in Figure 3-46. The color-coded dotted lines in the upper-left panel are the time gate-specific stationary noise due to the sensor's time response function as found in Figure 3-46.

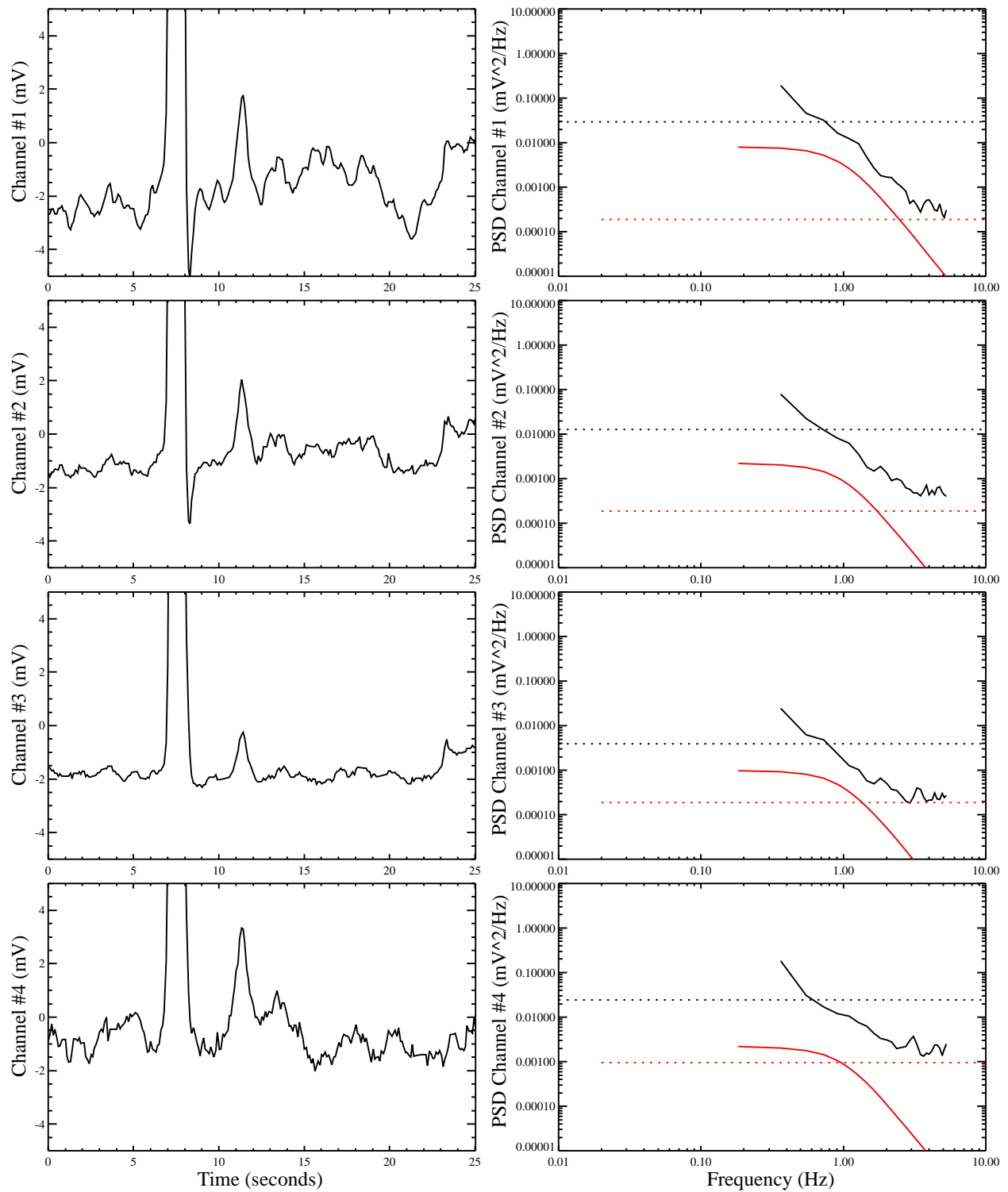


Figure 3-52 – Time Rasters (left) and Power Spectra (right) for the EM61 MkII / Towed Platform Combination at the Environmental Area. The red-dotted lines in the right-hand panels are the time gate-specific bit-level noise for the sensor as found in Figure 3-46. The black-dotted lines are the rms noise levels calculated on short time scales.

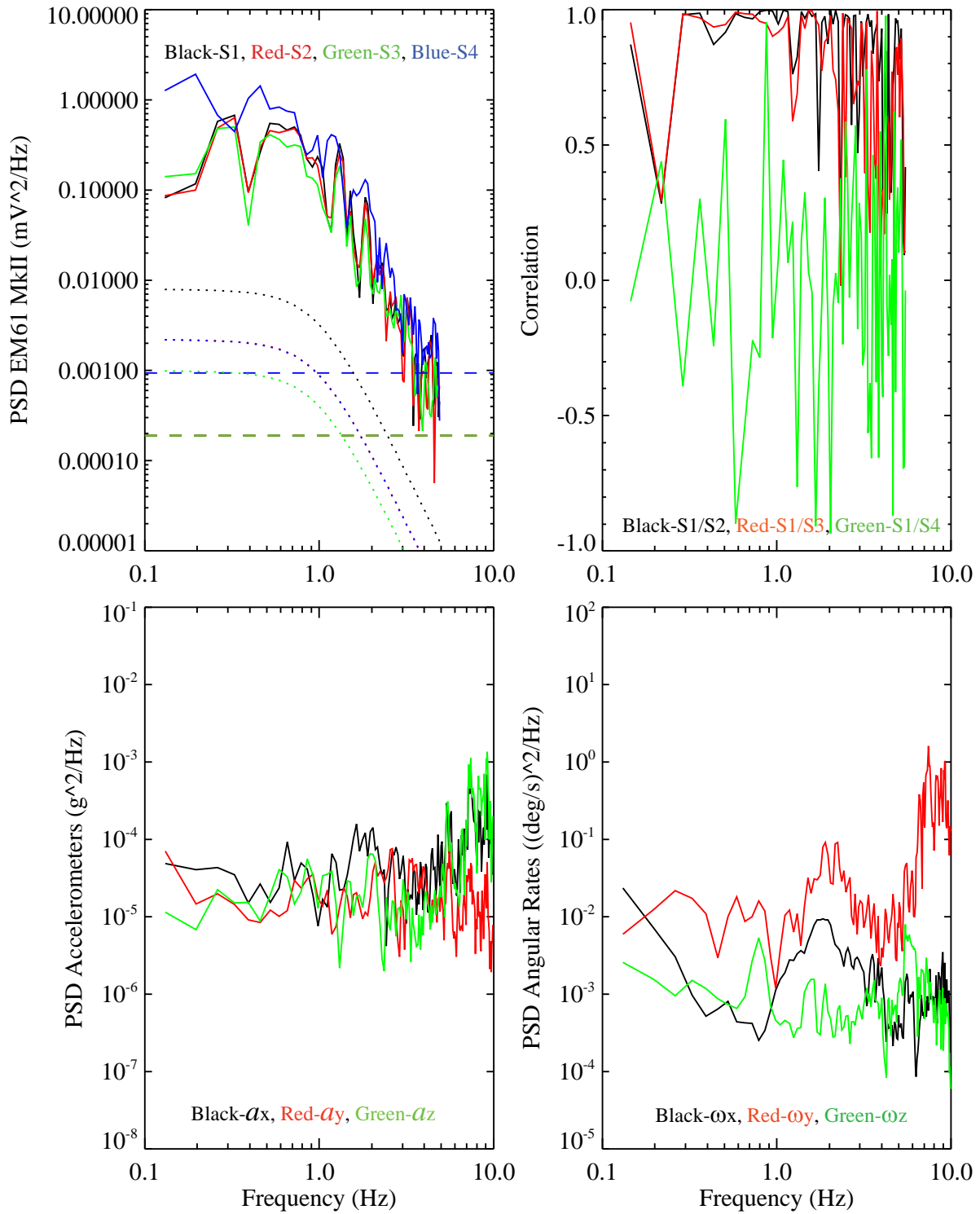


Figure 3-53 – Power and Correlation Spectra for the EM61 MkII / Rail System Combination at the Environmental Area versus IMU Data. The color-coded dashed lines in the upper-left panel are the time gate-specific bit-level noise for the sensor as found in Figure 3-46. The color-coded dotted lines in the upper-left panel are the time gate-specific stationary noise due to the sensor's time response function as found in Figure 3-46.

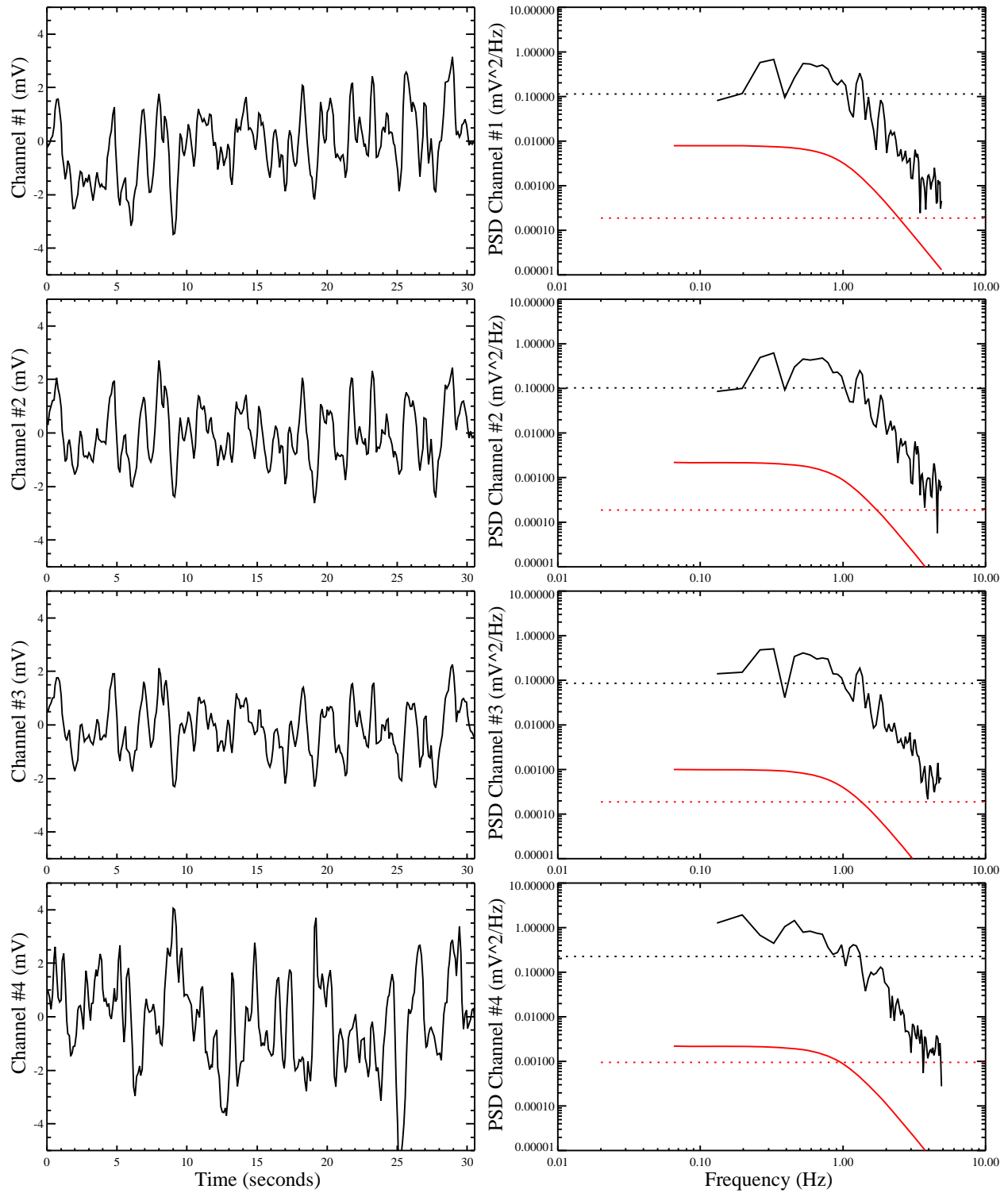


Figure 3-54 – Time Rasters (left) and Power Spectra (right) for the EM61 MkII / Rail System Combination at the Environmental Area. The red-dotted lines in the right-hand panels are the time gate-specific bit-level noise for the sensor as found in Figure 3-46. The black-dotted lines are the rms noise levels calculated on short time scales.

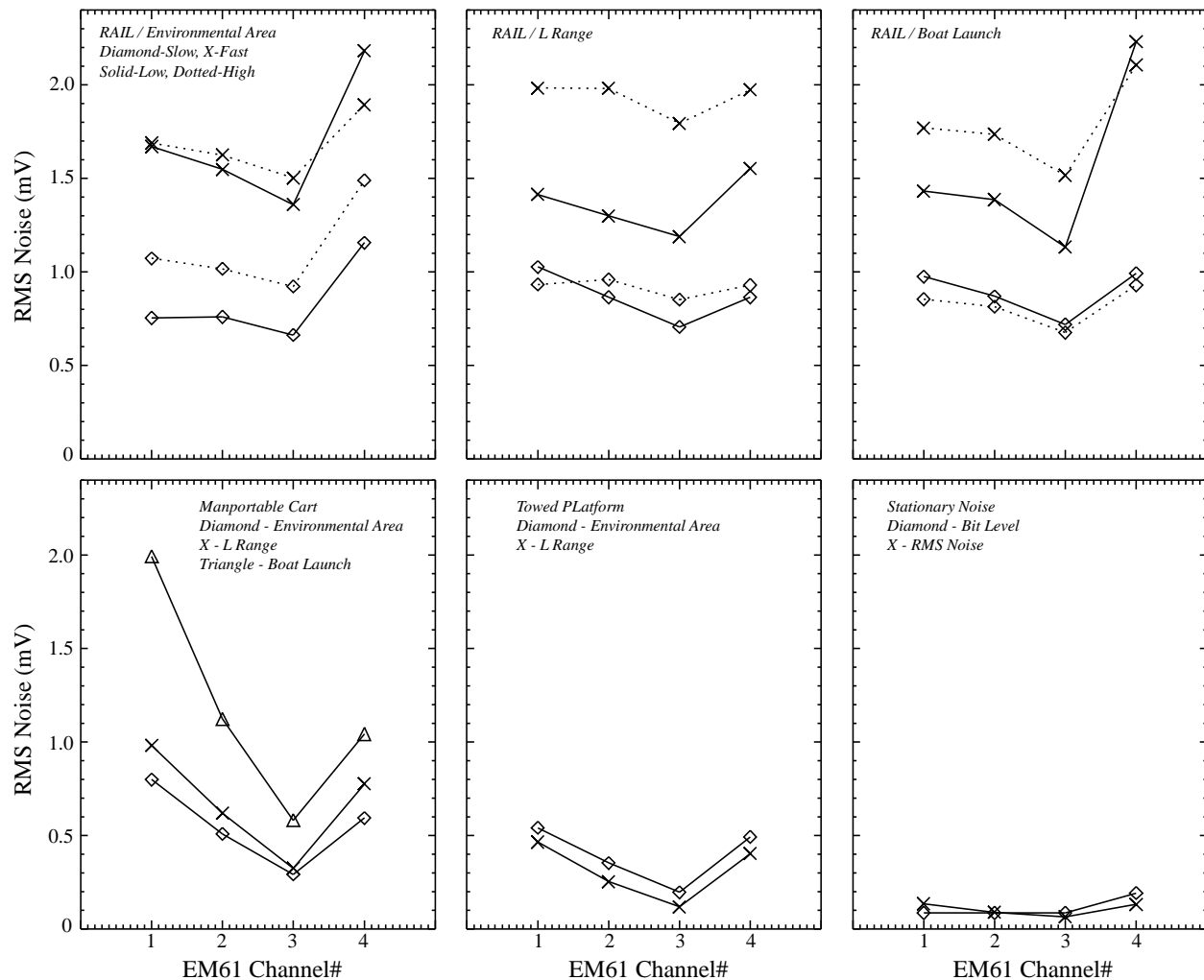


Figure 3-55 – EM61 MkII RMS Noise Levels for Several Platform by Time Gate

Figure 3-56 plots fifteen seconds of data as the EM61 MkII was pitched at a rate of once every two seconds. The top graph shows the measured angular pitch rate. The bottom graph shows the measured EM61 MkII data channels shifted slightly for comparison. The EM61 MkII was operated in 4-channel Mode and the data from each time gate are shown in magenta, blue, red, and green, respectively by gate center delay. The black curve is the expected output based on the measured IMU motion. The induced voltage was calculated from the pitch rate and pitch angle as a function of time, filtered by the sensor's dynamic response, and multiplied by a fixed gain factor. Note that both the measured EM61 MkII response and the modeled signal are shifted from the pitch rate by approximately 0.4 seconds because of the sensor response function. Figure 3-57 plots the measured and modeled EM61 MkII signals as the frequency and amplitude of the pitch rate are increased. The red and green curves are the measured EM61 MkII third and fourth time gates; the black curve is the expected signal based on the IMU measured motion. The frequency of the pitch rates are roughly 0.22, 0.5, 1.0, and 2.0 Hz. The peak-to-peak amplitudes of the pitch rate range from 10 to 60 degrees per second. The induced EM61 MkII signal initially increases with increasing pitch rate, but from 1 to 2 Hz, the sensor's dynamic response begins to significantly damp the induced noise.



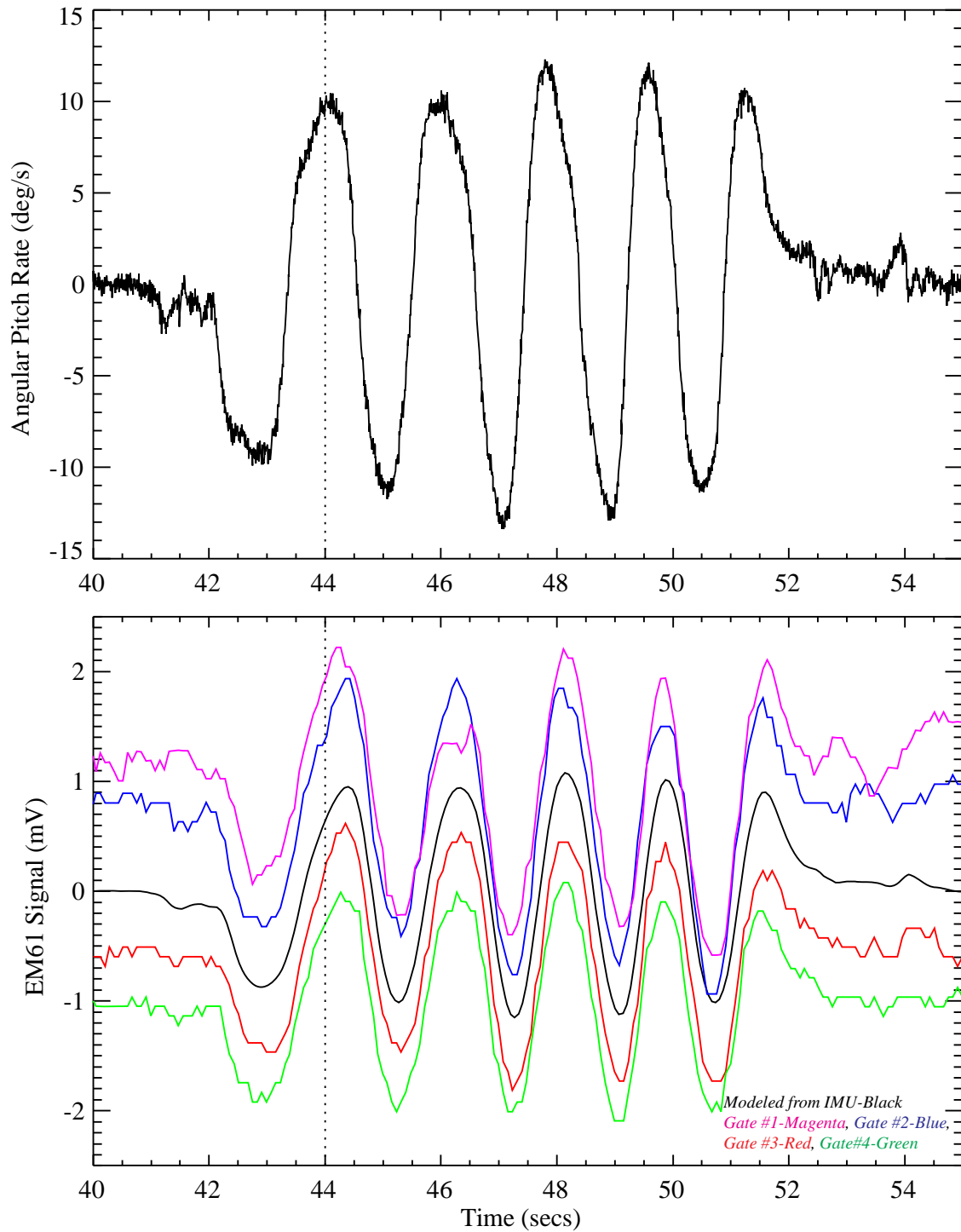


Figure 3-56 – Measured Response from an EM61 MkII while Undergoing Controlled Pitching. The top panel shows the sensor motion as measured by the IMU. The channel data are shown in the bottom panel as color-coded lines (time gates 1 – 4, magenta, blue, red, and green, respectively). The black line represents the modeled response using the IMU data.

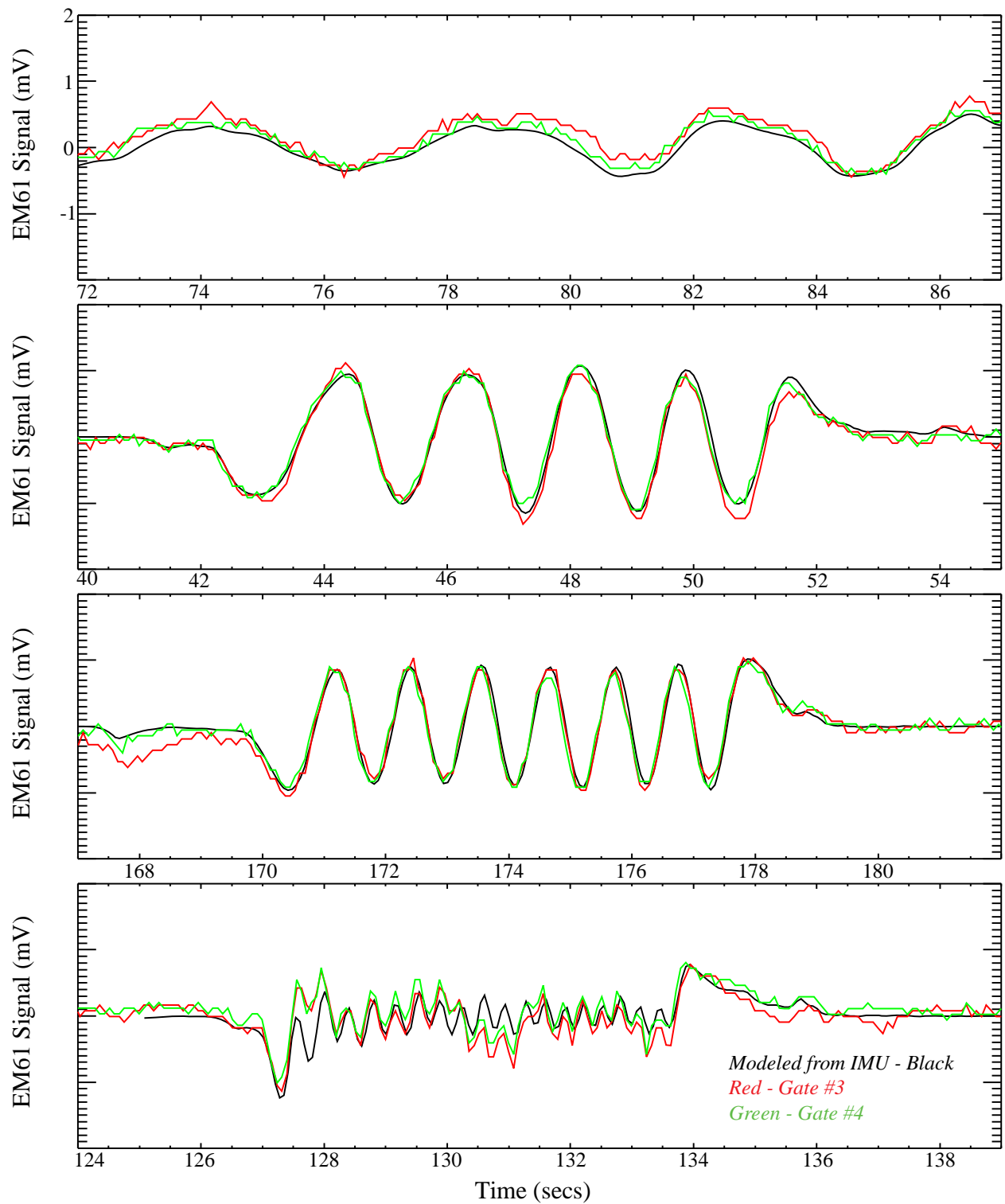


Figure 3-57 – Modeled and Measured EM61 MkII Response (for Various Pitching Rates. The channel data are shown as color-coded lines (time gates 3 – red and 4 – green). The black line represents the modeled response using the IMU data.

Figure 3-58 plots the signals measured as the MP cart makes one pass over the Environmental Area. The top graph plots the response for the first three time gates as measured by the EM61 MkII's lower coil (black, red, and green, respectively). Each time series has been roughly "zeroed" by subtracting a median value. The second graph plots the MP cart's roll (black) and pitch (red) rates measured by the IMU and shifted for clarity. The IMU (model VG-300) was sampled at 20 Hz and has a roll off in bandwidth at 10 Hz. The wheel barrow-style cart has a distinct pitch rate. The side-to-side roll is higher in frequency and more irregular, presumably due to the wheel base rolling over rough, irregular ground. The measurements on this site were at a significant angle to magnetic north and the voltage induced in the receiver coil was therefore mostly driven by the roll rate. The filtering effect of the sensor's time response damped out all but the low frequency content. The modeled EM61 MkII noise is shown in the bottom plot. The noise level is comparable to the short-scale noise (1 to 2 seconds). In addition to large signal peaks due to buried metal objects, there is consistent structure in the sensor response that reduces in amplitude for the later time gates, for example from 16 to 24 seconds in the times series shown in Figure 3-58. The apparent relative amplitude between the responses for the different time gates in this region is not inconsistent with the simple soil measurements that were made along the measurement transect. Further measurements and modeling of the soil response would be required to further analyze this contribution. A method to determine the zero level, or the response of the sensor in the absence of the ground or of any metallic objects, would be required and would most likely involve the ungainly effort of lifting the sensor and cart reasonably high off of the ground repeatedly.

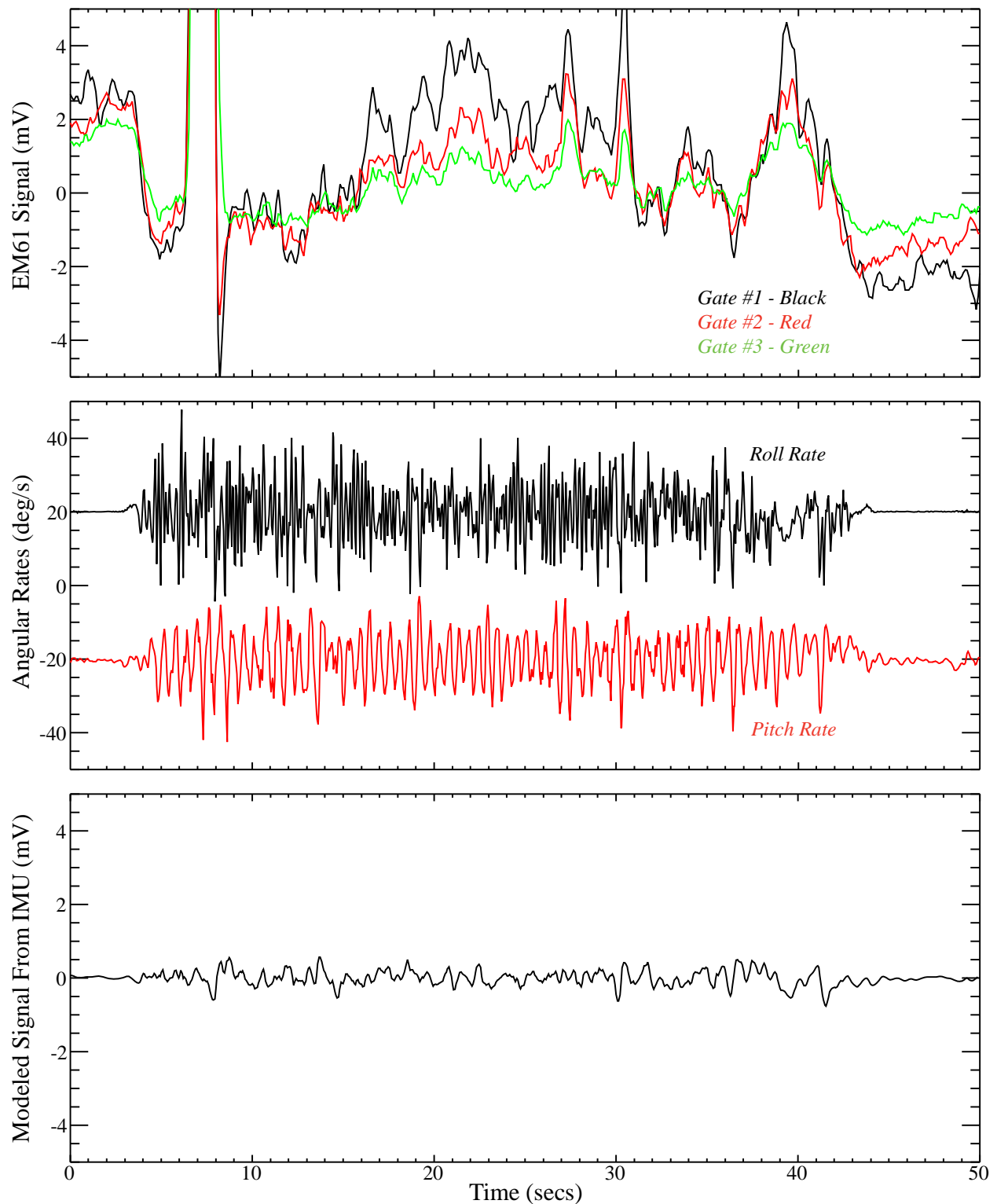


Figure 3-58 – Modeled and Measured EM61 MkII Response for the MP Cart / EM61 MkII Combination at the Environmental Area. The experimental data for time gates 1,2,3 are shown in the upper panel. The measured angular rates from the IMU are shown in the middle panel. The bottom panel has the modeled noise results based on the above data.

### **3.9 Monte Carlo Study**

#### **3.9.1 Objective**

The goal this demonstration was to investigate sources of noise in EMI surveys and to quantify their effects on detection probabilities and UXO/clutter discrimination success rates. For complete results, this goal requires noise sources to be understood both individually and in combination. We also aimed to quantify effects of survey configuration parameters that may be altered by site operators, such as survey speed and lane spacing.

#### **3.9.2 The Monte Carlo Approach**

To meet this goal, we employed the Monte Carlo method. We represented the complete system using a stochastic model, including the buried target, vehicle, sensor, and data inversion process. Multiple realizations were then drawn from this model to estimate performance under various assumptions. This effort differed from previous work in that noise sources in the stochastic model are carefully grounded in data from controlled measurements from Blossom Point, allowing separate noise mechanisms to be investigated individually and in concert. In particular, we have implemented new models to isolate sensor noise due to motion in the Earth's field, as well as motion relative to the ground. These improvements allow us to study effects from an increased range of scenarios e.g. different sensor height above ground, and different locations of the GPS receiver and sensor coils on the vehicle.

#### **3.9.3 System under Study**

The analysis performed here may be repeated for any system in general, provided adequate knowledge of the sensor (e.g. time gate information for time-domain systems, or frequency information for frequency-domain systems), but in the current work, we studied the specific system shown in Figure 2-5. This wheeled cart platform incorporated a GPS receiver and IMU sensor rigidly mounted to the frame and it operates with various sensors including the GEM-3 and the EM61-MkII. We simulated this system moving at walking speeds over moderately bumpy ground, based on data collected at Blossom Point MD. The cm-level GPS receiver and the IMU operate at data rates of 10 and 20Hz, respectively as described in Section 2.1.1.4. We ran Monte Carlo simulations for both the GEM-3 and EM61-MkII configurations.

#### **3.9.4 Stochastic Model**

Each realization of the stochastic model is drawn in a sequence of five steps. The sequence is summarized in Table 3-7, and details follow. After executing a large number of trials, overall performance is evaluated by comparing recovered values from Step 5 against true values from Step 1. Results of these trials are presented in following sections.

Table 3-7 – Steps of the Stochastic model

Step	Action
1	The target is defined. This includes position, orientation, and magnetic polarizability values (beta values).
2	The survey is defined. This includes the complete travel pathway for the sensor, including location and orientation (roll, pitch, yaw) at each measurement point.
3	Synthetic data are created. These are calculated using the dipole model (Appendix B), given information from Steps 1 and 2. In the case of the EM61-MkII sensor, the dynamic response is incorporated into the forward model. In the case of the GEM-3, the dynamic response is negligible.
4	Observed data are created. These data include observed GPS values, IMU values, and sensor signals, all of which differ slightly from true GPS, IMU, and sensor signals established in Steps 2 and 3.
5	Observed data are inverted. Data from Step 4 are submitted to inversion using the same tools employed on real data from field surveys.

#### 3.9.4.1 STEP 1. The Target is Defined

We assume the target is spatially isolated with no other targets nearby to contribute overlapping signals. This is a common assumption for data inversion schemes and it is reasonably accurate for a significant fraction of targets at typical UXO sites.

We always simulate the same target on each run so target response parameters (betas) do not vary from one realization to the next. This is done to focus on factors under operator control such as vehicle design, lane spacing and sensor height, instead of factors beyond operator control such as inherent target variability. This approach also facilitates comparison of true betas vs. recovered betas.

The target is a sphere, based on test stand measurements (both GEM-3 and EM61-MkII data) on a permeable steel ball with a 3 inch (76.2mm) diameter. Beta values derived from the test stand are used to define the target response. After executing a series of preliminary simulations for the EM61-MkII, we discovered this target was too small to produce the desired maximum signal strength under all configurations, so the betas were multiplied by a factor of 10 for simulations of the EM61-MkII. This roughly corresponds to a larger steel-ball target with a diameter approximately 6.5 inches. Betas for the GEM-3 were not adjusted in this way. The betas are identical for all three principal axes (longitudinal, two transverse) due to symmetry, with values:

Table 3-8. Beta values for Monte Carlo sphere target.

EM61-MkII betas		
Time gate	Center of EM61-MkII gate window ( $\mu$ s)	Beta ( $m^3$ )
1	216	0.41
2	366	0.29
3	666	0.17

GEM-3 betas			
Channel	Frequency (Hz)	I Beta ( $m^3$ )	Q Beta ( $m^3$ )
1	90	-0.0011479880	0.00034207795
2	150	-0.0010242577	0.00039629527
3	270	-0.00085539574	0.00045175003
4	570	-0.00060661200	0.00049949040
5	1170	-0.00033037260	0.00050922969
6	2370	-6.8273980e-005	0.00047738015
7	4890	0.00015611596	0.00041677300
8	10110	0.00034094436	0.00034125477
9	20970	0.00045062862	0.00028406464
10	43470	0.00056847474	0.00021086384

Note that the EM61-MkII instrument includes 4 data channels, but the data collected for this demonstration was collected in a differential mode where the 3rd and 4th channel take signals from the lower and upper coils (respectively) at the same (3rd) time gate, so these channels are both associated with the 3rd time gate beta. In this mode, there is no 4th time gate beta.

By using a spherical target, we reduce modeling errors that arise from our implementation of the forward model. As discussed below, we utilize the dipole model (see Appendix B), which is known to produce modeling errors particularly for large, elongated targets at shallow depth. For the purpose of this Monte Carlo study, this error occurs in the generation of synthetic data, and is therefore not one of the noise mechanisms under study. By using a spherical target, we reduce this error and allow the investigation to focus on other error sources of interest.

The sphere target is randomly positioned with uniform probability in a square region centered about the origin. Each side of the square region has length equal to the lane spacing, so the full range of target positions relative to the survey lane is possible. The target will sometimes lie directly under a survey lane, and sometimes lie directly between two lanes. The target z coordinate (depth) is drawn from a uniform random distribution from 0 (ground surface) down to -1.0m. This produces the desired range of signal strengths needed for analysis of SNR.

Uniform distribution for the z coordinate results in non-uniformity in the distribution of associated signal strengths, since the two are not linearly related. This acts to produce relatively fewer high-signal targets, and relatively more low-signal targets. This property is helpful for characterizing performance with respect to noise mechanisms since failure cases correlate with low SNR. However, at real sites, accurate prediction of performance requires accurate

estimation of the true distribution of target depth. Our assumption of a uniform depth distribution from 0 to 1m is a crude approximation which must be refined when this approach is tailored to a specific site.

### **3.9.4.2 STEP 2. The Survey is Defined**

This step involves the determination of the complete travel pathway for the sensor as it travels back and forth over the target, including location (x,y,z) and orientation (roll, pitch, yaw) at each measurement point. Since the GPS receiver is spatially separated from the sensor itself, we generate travel path information for both.

A problem arises from the “lever arm” interaction between the GPS and the IMU. We use the term “lever arm” to refer to the fact that when the vehicle undergoes rotation about any axis, the GPS receiver experiences spatial deflection. These deflections can be accounted for during processing if orientation data is provided, but errors in orientation data translate into associated navigation errors when calculating coil position. This is what we mean by “lever arm” errors. These errors would be entirely absent if the GPS receiver were somehow co-located with the sensor, which is not possible since the GPS equipment interferes with sensor performance. These errors also scale with the separation distance between the GPS receiver and the sensor.

In the process of developing the Monte Carlo model, we recognized that the pivot point for changes in orientation tends to be the point of contact where the wheels meet the ground, and this results in a significantly smoother travel path for the sensor itself since it is close to the ground, compared to the GPS receiver which is typically mounted higher up. The GPS receiver tends to meander left & right of the intended travel path more than the sensor coils do because rolling motion due to uneven soil produces greater cross-track deflections in the upper portions of the vehicle. A similar mechanism operates with respect to yaw: GPS data tend to exaggerate cross-track deflections due to yaw when compared to cross-track deflections experienced by the sensor, since the GPS receiver is mounted farther away, horizontally, from the pivot point, which is the point of contact where the wheels meet the ground. For this reason, we were unable to get realistic results using raw GPS records as our basis for travel path simulations. Instead, we based our simulations on calculated sensor pathways which were derived from GPS and IMU data collected at Blossom Point. As mentioned above, these pathways tend to be somewhat smoother than the raw pathways reported by the GPS.

#### *Sensor Location (x, y, z)*

True sensor motion results from a combination of random processes with non-trivial underlying probability distributions. To simulate motion as accurately as possible, we “cut-and-paste” short segments of actual sensor position data collected at Blossom Point. Each simulated survey lane over the target is determined by carving a separate random “snippet” of a few meters’ length from very long (100m+) straight-line transects of data collected at Blossom Point.

The data structure containing the long straight-line transects was prepared as follows. The system shown in Figure 2-5 was used at Blossom Point to make several passes around a long skinny rectangular pathway with the long dimension greater than 100m. For each traverse of the long dimension, the sensor position was calculated using IMU and GPS data, then these 3D point



clouds were each separately fitted to a straight line in 3-D. The straight-line fit represents the intended path, and the actual coordinates represent deflections from the intended path. These deflections were assembled into a data structure indexed by distance along the transect, which was then used to support random realizations of sensor motion.

Realizations of sensor location are prepared as follows. Our simulated survey lanes always run north-south (parallel to Y axis) direction. This is solely for the sake of convention and does not introduce any bias, since coordinates can always be rotated without loss of generality. Individual measurement points for each lane are determined by indexing into the data structure described above using a random reference point along the fitted lines. A short interval of associated sensor measurement points before and after the reference point is mapped to corresponding locations in the synthetic survey. Each survey lane crossing over the anomaly is determined separately in this way; by randomly “cutting” and “pasting” a separate snippet of sensor location data from the Blossom Point record.

Note that each reference point is a continuous variable which is allowed to have fractional values and will generally not coincide with sensor positions in the Blossom Point data structure. This means associated measurement points in the synthetic survey will generally not be synchronized from one lane to the next: they will be staggered along-track randomly, which is appropriate.

Deflection values within each snippet are de-measured prior to their application into the synthetic survey. After each snippet is selected, but before it is applied to the synthetic survey, cross-track deflections are centered about their mean (within the snippet), and vertical deflections are separately centered about their mean. This eliminates long-range meander in the Blossom Point data, and it removes gross elevation changes in the Z direction.

This approach assumes that sensor motion over the target is independent from one survey lane to the next. This assumption is reasonable in the horizontal XY plane: barring ruts or other large-scale features on the ground surface, cross-track meander is independent from one survey lane to the next, due to the fact that meander is predominately affected by operator difficulty keeping the vehicle on the intended path. The operator is assumed to have no pre-disposition to meander left or right in correlation to adjacent lanes. In contrast, however, vertical dimension is likely to experience a greater degree of correlation due to ground elevation. To the extent that Z deflections are caused by operator motion (tipping, bouncing, etc.) Z deflections are uncorrelated. However, to the extent these deflections are caused by gross features in ground elevation, Z deflections may be correlated, if the scale of fluctuation in the ground surface is long compared to the survey lane spacing. In this work, we assume *no* correlation of Z deflections within the anomaly, from one survey lane to the next. Thus, we assume the ground is relatively flat and any Z deflections are attributed to small-scale undulations in the ground surface, and/or vehicle tip & bounce. This approximation could be refined in the future by modeling 3D ground elevation, but that is not within the scope of the current project.

We refer to signals resulting from coil motion (vertical bouncing and tilting) relative to the ground as “geologic noise”. This noise results from the fact that soil produces a signal which depends strongly on range and sensor orientation. We model this noise using a detailed soil model (see Sections 3.7.3 and 3.8.4) that includes frequency-dependent magnetic susceptibility values fitted so as to match the observed soil response at Blossom Point. Our current

implementation of this model provides signal estimates only for a horizontal coil over a half-space, so we have not implemented ground effect from coil tilting (orientation), only from coil bouncing (Z elevation).

There is a difficulty in modeling this noise source because we have no direct field data reflecting a running record of coil-to-ground distance, as the sensor moves along the survey lane. We have only the Z coordinate from the GPS in the vehicle, and not the Z coordinate of the ground. To overcome this difficulty, we partition the Z motion of the sensor into two components: 1) motion caused by the ground, i.e. the long-scale rise and fall of the vehicle as it rolls over broad features in the terrain, producing no net changes in the coil-to-ground distance. 2) everything else, i.e. “Z bounce” resulting from transients in the suspension, small bumps & ruts in the ground etc. which cause changes in the coil-to-ground distance.

Component (2) is the one that produces geologic noise, and we are forced to make use of an assumption when modeling it since data are not available. We assume sensor position records of vertical motion at Blossom Point may be divided as follows: Motions at 1 to 2 Hz and slower represent ground elevation changes (component 1), while motions at higher frequencies represent Z bounce (component 2). We developed a desired spectrum for Z-bounce by high-pass filtering the observed spectrum of sensor Z data collected at Blossom Point.

Realizations of Z-bounce motion are created by taking an FFT of a white noise source and convolving the result with the desired spectral density, described above, then taking the inverse FFT to define the synthetic data set. This method guarantees that on average, synthetic data will possess the desired spectral density. Long records of jointly-simulated Z-bounce motion and associated geologic noise are prepared and used to support realizations of the Monte Carlo model. Random snippets of Z-bounce motion, along with associated geologic noise, are selected from the long synthetic record, and the Z-bounce component is added onto the sensor Z data determined from the snippet of Blossom Point data.

To summarize, each survey lane crossing over the anomaly is generated independently, based on a single “snippet” of actual Blossom Point sensor pathway data, which is cut-and-paste into position, and the Z component has an additional synthetic term added on representing coil-to-ground variations (Z-bounce).

Table 3-9 – Summary of sensor xyz travel simulation

Axis	Simulation
x	Snippet from GPS.
y	Snippet from GPS.
z	Snippet from GPS plus synthetic Z-bounce added on.

#### *Sensor Orientation (roll, pitch, yaw)*

Records of roll, pitch, and yaw are independently constructed using a procedure similar to Z-bounce described above. The motivation for this choice is that roll, pitch, and yaw produce sensor signals due to receiver coil motion in the Earth’s field, so joint simulations with associated noise are needed. When sensor orientation changes, the Earth’s magnetic flux  $B$  through the receive coil may also change, inducing a signal which is proportional to the rate of

change of B, dubbed “B-dot” noise. Long records of jointly simulated sensor orientation and B-dot noise are constructed and used to support random realizations of the Monte Carlo model.

These records are constructed as follows: White noise is generated and submitted to FFT. The result is convolved with a spectral density function derived from IMU data (no high-pass filter required here), and then the inverse FFT yields the synthetic data set. This method guarantees that on average, synthetic data will possess the desired spectral density. Separate and independent realizations for roll, pitch, and yaw are constructed in this way, each making use of specific desired spectral densities. Associated B-dot signals are calculated by assuming each set of coil deflections occur around a quiescent coil orientation which is flat. Cross terms representing interactions e.g. between roll & pitch are assumed to be negligible: each contributes to the simulated record of noise independently.

The on-board IMU used at Blossom Point provides roll and pitch data, but not yaw. Angular acceleration signals are available for all 3 axes, but the task of integrating to find yaw is troublesome since errors accumulate, so we instead based our desired spectral density for yaw on the existing spectral density for roll. This approach ignores the relationship between yaw and x,y pathway i.e. the vehicle exhibits tendency to meander left following a yaw signal to the left, but in our implementation, this effect is not reproduced. While that represents a limitation to our simulation, it is not a significant problem since performance is governed most strongly by errors in coil positions, not by relationships between yaw and x,y pathway. In any case, sensitivity to yaw for the EM61 MkII is low and GEM-3 is zero (having circular coils).

Separate and independent data sets are constructed for roll, pitch, and yaw. Associated signals resulting from coil motion in the Earth’s field (B-dot) are also calculated and added into the synthetic data later in Step 3.

### **3.9.4.3 STEP 3. Synthetic Data are Created**

This step is a straightforward application of the dipole model (Appendix B) using the “true” target defined in Step 1 and the “true” sensor information defined in Step 2. As mentioned in the discussion of Step 1, the dipole model introduces a known modeling error which is accentuated for elongated targets. By using a sphere target this error is reduced, but a more accurate solution would be obtained by using a numerical model such as BOR.exe [14] to create the synthetic data. This approach is currently not computationally feasible however.

For the case of the EM61 MkII sensor, the forward model includes the dynamic response filter which acts to delay changes in sensor response, effectively “pushing” anomaly peaks along-track in the direction of travel.

### **3.9.4.4 STEP 4. Observed Data are Created**

In this step, the full collection of observed values is defined, incorporating all noise mechanisms acting in concert. This represents our most accurate approximation to real field data.

*Observed GPS data*

Observed GPS data are determined by first calculating the true position of the GPS receiver using the true sensor position and the true orientation of the vehicle. An error term is then added, derived from a long record of GPS data collected with a stationary receiver at Blossom Point. The centroid of these stationary data was subtracted from the entire record, leaving only residual errors, and random snippets of these errors are selected and applied to the true GPS position to yield the observed GPS position. In this way, the exact nature of GPS error fluctuations is preserved in the simulated data.

Based on the stationary receiver data, errors are about 7mm RMS horizontal and 12mm RMS vertical. This is smaller than what was previously estimated based on goodness-of-fit arguments, but the question of GPS errors under motion was evaluated using data from the rail system at Blossom Point (see Sections 3.7.4 and 3.8.5). Those data confirmed that GPS errors under motion along the rail are the same as errors for a stationary receiver, which agrees with claims made by the GPS manufacturer.

#### *Observed IMU data*

Observed IMU data are determined by adding an error term onto the true orientation of the vehicle. The error term is a random snippet taken from a long record of IMU data collected at Blossom Point with the vehicle stationary. The long record includes separate channels for roll and pitch, and each is de-meaned (deflections about the mean) before being used to support Monte Carlo realizations. Observed yaw is created by adding a separate random snippet from the roll signal onto the true yaw orientation. This approach makes the assumption that yaw errors exhibit approximately the same kind of randomness as roll errors, and also that IMU errors in general are similar at rest compared to the motion case.

#### *Observed Sensor Data*

Observed sensor data are created by taking the noise-free signal originally generated in Step 3 and adding three noise components: B-dot noise, Z-bounce noise, and static sensor noise. The B-dot noise and Z-bounce noise are available from the joint simulations of sensor motion described above. The static sensor noise is a random snippet taken from a long record of sensor data with the sensor stationary. As with the other data sets, the static noise data is de-meaned before being used to support Monte Carlo realizations.

#### *Observed Timing*

Timing error between the GPS clock and the sensor clock is simulated by taking a single realization from a normal distribution and applying that time lag (s) to the GPS data. The mean and variance of the distribution, 0 and 0.01 respectively, are derived from experience with systems of this kind.

### **3.9.4.5 STEP 5. Observed Data are Inverted**

Realizations of observed synthetic data drawn from the stochastic model are submitted for processing just like real data from a site survey. First, the data is carved to include only the collection of measurement points within 1.0m of the anomaly center. This carve radius is fixed for all anomalies, and it may be adjusted as a configuration parameter. In practice, an operator

carves the data manually using polygons, and we have not implemented code to simulate that process. The 1m circular disk curve is intended to be a reasonable surrogate for the case of an isolated target with no neighbors nearby.

In the case of the EM61 MkII, the dynamic response of the sensor creates a significant spatial shift in the data. Figure 3-59 in shows how dynamic response acts to shift data along-track and produce “chevron” patterns. A typical method of processing these data is to apply a time shift on the GPS position information until contours of the sensor signal appear to be aligned by eye. The data carving step is performed on these “aligned by eye” data. The data are then inverted in their shifted locations using a static inverter. However, after carving, the down-selected data are also returned to their true measurement locations for inversion with the dynamic inverter.

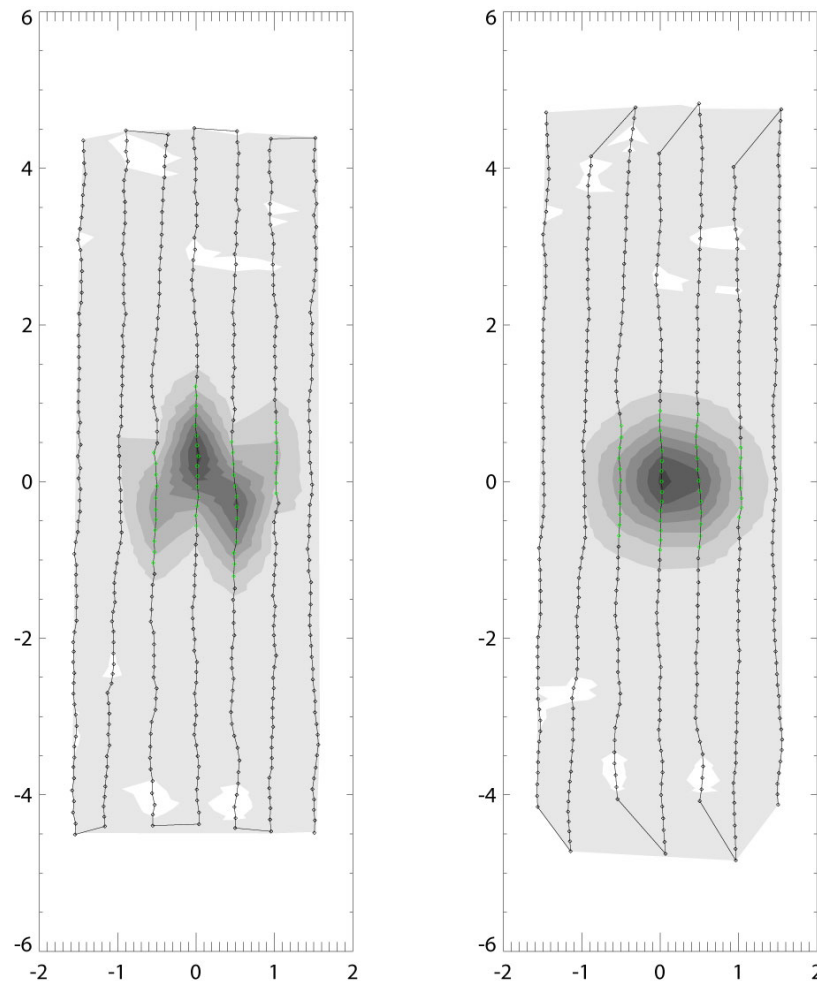


Figure 3-59 – Contour maps of synthetic EM61-MkII data, first time gate. The raw data (left image) shows the characteristic “chevron” pattern caused by the delayed onset of peak signals due to dynamic response of the sensor, which is moving at walking speed ( $\sim 1$  m/s). In the right image, a time lag is applied to the raw data, effectively shifting positions along-track until contours appear by eye to be aligned properly for further processing.

Each segment of survey passing over the anomaly is leveled separately by removing the median value from each channel, and sensor coil position & orientation is calculated using the observed GPS data and the observed IMU data. In this way, imperfect knowledge of sensor roll, pitch & yaw produce additional “lever arm” errors in the calculated coil position, over and above the existing navigation errors, as experienced in real surveys. Sensor yaw was initially calculated using point-to-point course-over-ground information, but we quickly discovered that this approach produced severe deflections in the coil position, so we chose to define platform yaw using only the first and last points in each survey segment, and assume it to be constant along the whole segment.

Processed data is then submitted for inversion using standard practice for EM61 MkII data. We implement a 2-stage fit in which the first stage uses the “full matrix” method where target  $z$  is stepped through values at 3cm intervals,  $x,y$  coordinates are searched non-linearly at each  $z$ -depth, and tensor response terms are found linearly within each iteration. This stage results in a different solution for each  $z$  depth, and the  $k$ -best of these, measured using the goodness of fit criteria, are passed into the second stage to serve as starting points.

The second stage also executes a “full matrix” solution, but here,  $x,y$ , and  $z$  are all searched non-linearly and the response tensor elements are found linearly within each iteration as before.

#### **3.9.4.6 Standard inversion**

For the case of EM61 MkII data, the dynamic response of the sensor acts to shift transect data later in time, which effectively moves these signals farther along the survey transects, creating a characteristic chevron pattern as the sensor sweeps back and forth over the target, Figure 3-59. The amplitude of the peak is also decreased and the down-track width of the peak broadened. This phenomenon is typically addressed by applying a small time lag to the sensor data in order to bring the signals into alignment, judged by eye, and then applying inversion without the dynamic response effect. This approach has the advantage of simplicity, but the disadvantage that distortions in the transect data due to the dynamic response are not addressed.

#### **3.9.4.7 Dynamic Response Inversion**

An alternative fitting method incorporates the sensor’s dynamic response into the fit. In this approach, no time lag is needed and the observed sensor data is submitted, chevrons and all, for inversion. This approach is somewhat more complicated to implement and it runs more slowly, but it has the advantage that distortions in the transect data are addressed.

Our implementation of dynamic inversion relies on expressing the dynamic behavior of the EM61 MkII as a transform, and making use of the fact that this transform is linear. This equation can also be expressed as a linear filter applied to a step function excitation. We implement dynamic inversion by making use of the linearity of this filter.

Static inversion proceeds by executing a non-linear search on the spatial  $xyz$  coordinates of the target, and a linear solution is found in each iteration representing the best possible match to data assuming that  $xyz$  location. This solution is obtained by calculating six signal sets, corresponding to the six elements of the symmetric response tensor which fully define the tensor. Appendix B describes these six entries. In practice, the signal sets are found by inserting unity

into each of the six tensor positions and calculating a signal set for each. A linear combination of these is found and the resulting best-fit weights then define the values of the best-fit tensor.

For dynamic inversion, we proceed with the same approach, except that each of the six signal sets is modified using the dynamic response transform (kernel convolution) before finding the best-fit linear combination to match observed data. This approach relies on the fact that for linear transforms:

The transform of summed functions = the sum of transformed functions,

so application of the dynamic filter on the six signal sets is equivalent to applying the filter to their sum, regardless of the best-fit weights found to match observed data.

### **3.9.5 Results**

Output from the simulator generally exhibits patterns of variability which are similar in scale and shape to variability seen on real surveys with similar hand-pushed cart vehicles, such as the EM61 MkII MP cart survey at Site 18 of the former Camp Sibert, AL which we recently analyzed. This comparison is important because it is the only form of validation we have to confirm that our results comport with reality.

Figure 3-60 shows a comparison of results from this Monte Carlo study against results obtained from a field survey at the former Camp Sibert, in which a wheeled EM61 MkII sensor was deployed. Figure 3-60 shows data for a large collection of 4.2-in mortars measured in the ground at the former Camp Sibert. These rounds will have some inherent variability from one example to the next, and the spread of recovered beta values must reflect this fact, while the synthetic sphere targets in our study were always identical, so we expect some differences in the recovered beta clouds. There is also the fact that the 4.2-in mortars were a different shape, and larger than the ~6.5 inch spheres used in our study, and lastly, the terrain at Camp Sibert would produce different characteristic motion in the sensor platform, compared to motion at Blossom Point, which was the basis for our simulations. So we expect some differences, but we view the broad comparison favorably, and feel that it encourages a sense that our simulations are representative of reality.

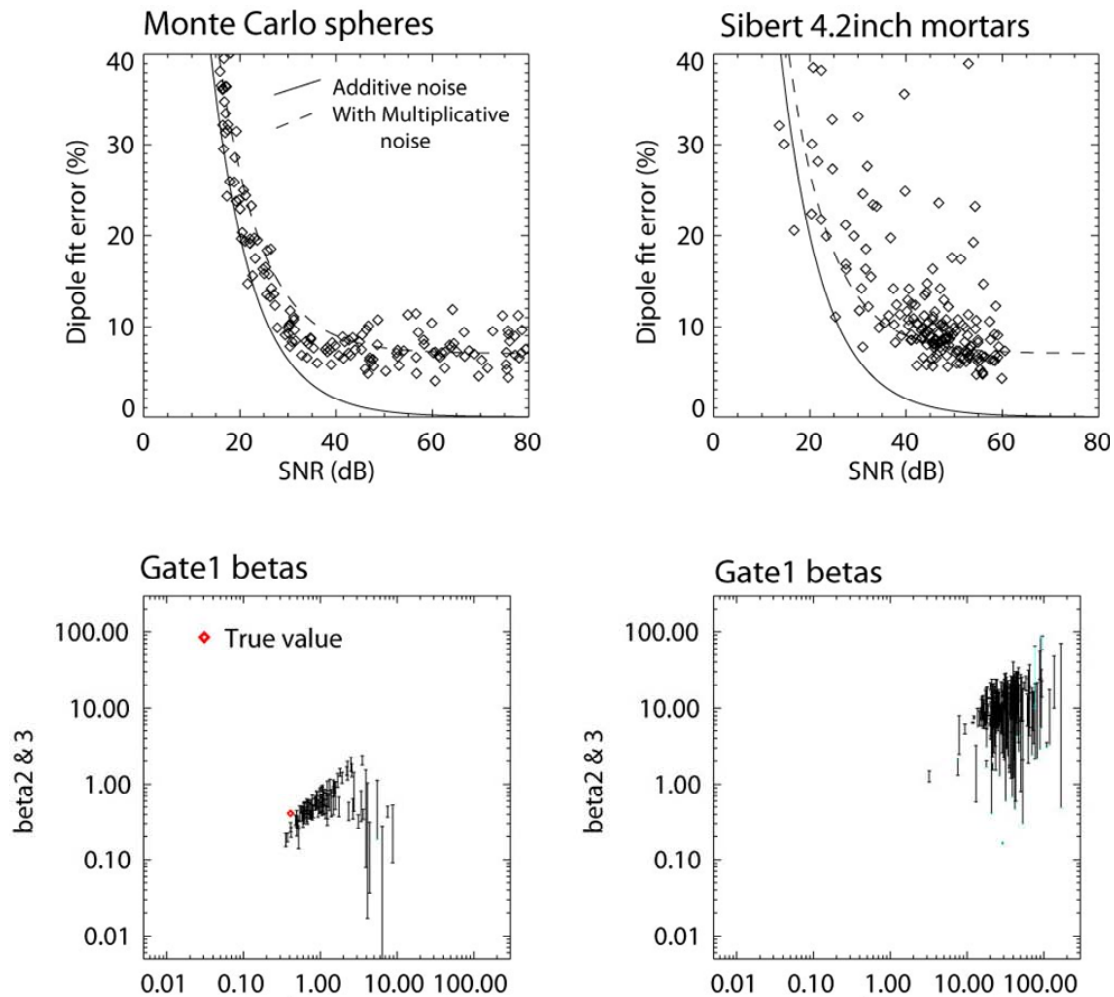


Figure 3-60 – Output from this Monte Carlo study (left two graphs) compares with corresponding results from Camp Sibert (right two graphs) in which a large number of 4.2-in mortars were processed. The upper set of graphs shows the relationship between fit error and signal to noise ratio (SNR). The lower set shows the spread of recovered beta values. This comparison is imperfect since the man-portable system deployed at the former Camp Sibert is different from the system modeled in this study (Figure 2-5). Still, the broad trends encourage a sense that these results are reasonable representations of reality.

A more rigorous test of this approach could be obtained by applying the methods outlined in this project to a specific wheeled EM61 MkII system which is involved in a site survey. This test would require that the site contain many examples of a specific target type, and careful measurement of environmental noise and platform motion using a high performance IMU.

#### *Additive noise vs. Multiplicative noise*

The upper two graphs in Figure 3-60 include a pair of lines drawn to illustrate the impact of additive noise and multiplicative noise. Additive noise refers to noise which is added on to the signal of interest, an example is B-dot noise. Multiplicative noise scales with the signal, an example is navigation error, which produces large effects where signal gradients are steep, thus



they scale with signal strength. The solid line represents theoretical performance in the presence of additive noise. Additive noise includes a variety of mechanisms and is generally site dependent. The amount of noise reflected by the solid line was adjusted to facilitate comparison on the graphs. The dashed line represents performance with both additive and multiplicative noise. Again, the amount of multiplicative noise here was chosen simply to facilitate comparison on the graphs. The equations for these theoretical performance curves are derived in Reference 15.

This Monte Carlo study assumed 6.5-in diameter sphere targets, which produce less response compared to the Sibert 4.2-in mortars, as evidenced in the lower two graphs. This study also assumed a wide range of burial depths for the targets, which is reflected in the wide distribution of SNR in the upper left graph, compared to a tighter grouping of SNR in the upper right graph.

Note that results in Figure 3-60 are generated without knowledge of IMU signals, and using static inversion. This was done to simulated actual data processing implemented at real sites, as closely as possible.

#### *Dynamic response vs. Static response*

As discussed in the section above titled “STEP 5. Observed Data are Inverted,” we implemented the standard static inversion approach, as well as a dynamic inversion.

One interesting effect seen in these data is the clear bias in fitted target depth using the standard inversion procedure, but this bias is absent when dynamic response is incorporated. This effect can be understood since the dynamic response acts as a low-pass filter which tends to flatten sharply varying signatures (shallow targets) more than smoothly varying ones (deep targets). The effect of this distortion is to incorrectly fit shallow targets to deeper fitted depths, and assign high values to the response tensor to compensate for the increased range. This effect is most pronounced for shallow targets where sensor data includes more high-frequency components and the low-pass filter thus has more effect.

#### *Lane spacing trade-off*

Figure 3-61 shows predicted performance under different lane spacing. These data apparently suggest there is little benefit in going to 0.25m lane spacing since results are comparable to 0.5m. Performance at 0.75m and 1m lane spacing are notably worse, which might allow decision-makers to weigh this trade-off more accurately when designing the survey.

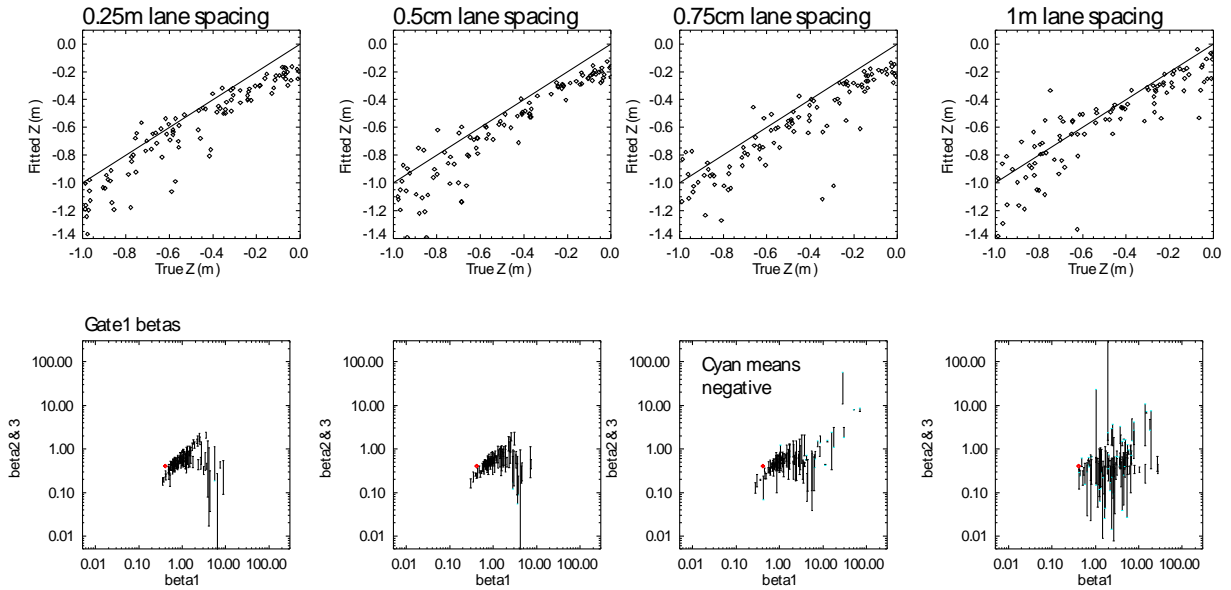


Figure 3-61 – Predicted performance with different lane spacings. The upper panels show the fitted  $z$  results and the lower panels plot  $\beta_2$  and  $\beta_3$  versus  $\beta_1$ . The solid line in the upper panels indicates where the fitted  $z$  equals the true  $z$  value.

#### *Trade-offs for other configurations*

Figure 3-62 shows predicted performance under different survey configurations. If the sensor is placed with 0.5m height above the ground instead of 0.25m, there is an associated degradation in performance. We also expect degraded performance when the sensor is too close to the ground due to heightened geologic noise, and this tool would allow determination of an optimal height, when applied to a specific sensor and site.

Figure 3-62 also shows the performance benefit gained by including IMU signals in the inversion, as well as benefit gained by simply mounting the GPS receiver directly over the sensor instead of having it positioned toward the rear of the platform. The improvement in performance results from removing the horizontal lever arm, which contributes navigation errors through interaction with imperfect yaw data.

Note that all the results in Figure 3-62 illustrate the same bias for depth errors, which is accentuated at shallow depths. This effect is due to the low-pass filter aspect of the sensor dynamic response, as discussed above in “Dynamic response vs. Static response”.

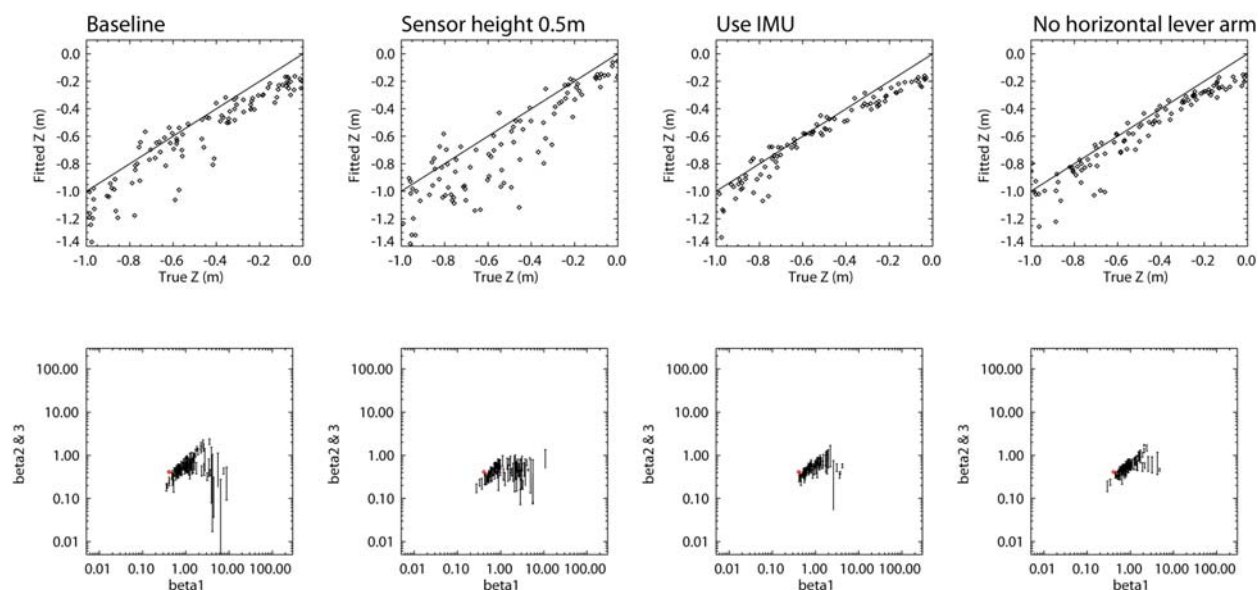


Figure 3-62 – Predicted performance for other survey configurations. The upper panels show the fitted  $z$  results and the lower panels plot  $\beta_2$  and  $\beta_3$  versus  $\beta_1$ . The solid line in the upper panels indicates where the fitted  $z$  equals the true  $z$  value.

### 3.10 Management and Staffing

The project was initially managed by Dr. Herbert Nelson, NRL. Drs. Dan Steinhurst and Tom Bell assumed the management role during the later portion of this demonstration. Staff for the investigation includes employees of Nova Research, SAIC-ASAD (formerly AETC), and NAEVA Geophysics. All contact information is listed in Section 7 of this plan.

## 4. Future Demonstrations

Based on the modeling results and analysis from this demonstration, we outline below two proposed strategies for future demonstrations. The first strategy is a full set of measurements and analysis based on the lessons learned from this demonstration to be conducted over the course of a week. The second involves the EM61 MkII Simulation Tool that was presented to the Program Office during the May 2008 In-Progress Review. From these results, one can begin to understand real world EMI survey noise sources both individually and in combination. One can start to quantify these effects in terms of survey configuration parameters which are under site manager and data collection operator control, such as lane spacing and survey mode.

### 4.1 Full-Scale EMI Noise Characterization Demonstration

This strategy's level of effort is designed to require approximately 1 week of data collection with a staff of 6 people, as per the scope of work from the original project definition. The following

sections discuss the proposed set of EMI sensors to be used in the next demonstration and the suite of measurements to be made with these sensors.

#### 4.1.1 EMI Sensors

Individual samples of the three EMI sensor types discussed in Section 2.1.1 were characterized at length during this initial demonstration. The Geonics EM61 MkII sensor is the de facto standard instrument used in the UXO industry and remains a part of future demonstrations in the project for this reason. The Geophex GEM-3 sensor has yielded significant information on geological response in this current demonstration and the data products has proved amenable to separating the contributions of the noise sources studied in this demonstration, as shown in earlier Sections of this report, e.g. Section 3.7. The richness of results from the GEM-3 more than compensate for the sensor's limited penetration into the UXO industry. The GEM-3 is also the only frequency-domain EMI sensor examined in this demonstration. Based on these considerations, the GEM-3 will remain a part of future demonstrations in this project.

The Geonics EM63 sensor is a time-domain instrument like the EM61 MkII, but samples a larger portion of the signal transient (180  $\mu$ s – 25 ms versus 216  $\mu$ s – 1.27 ms for the EM61 MkII) with more points (26 versus 3/4 points). The value of sampling the signal transient at later times is demonstrated in Figure 4-1, where data from the MTADS Discrimination Array (built under ESTCP Project MM-0601) are shown for UXO and cultural items.

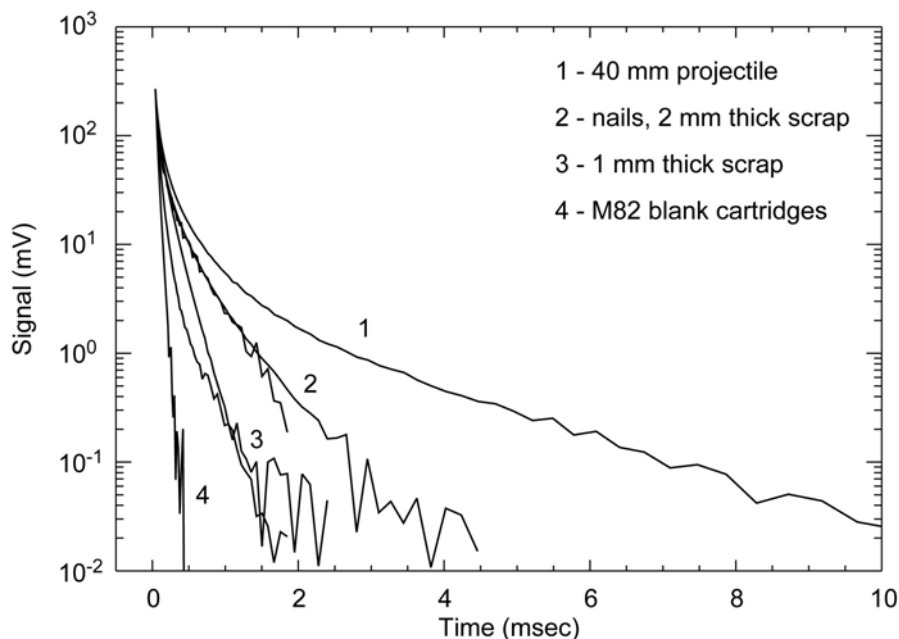


Figure 4-1 – MTADS Discrimination Array Transients for Several Items

The EM61 MkII can only sample the sample transient out to 1.27 ms, where the transients for the four items shown in Figure 4-1 are still very similar and would be difficult to separate. After 2 ms, the thin-walled items are clearly separated from the heavier walled items. As discussed in Section 2.2.4, the frequency-dependent geologic responses measured with the GEM-3 sensor increase in the quadrature response as a function of frequency (see Figure 2-12). The first time

gate of the EM63 is at 177  $\mu$ s, and corresponds roughly to a GEM-3 frequency of 1 kHz. Later EM63 time gates correspond to lower GEM-3 frequencies. The lack of a measured geological response in the data collected with the Geonics sensors, Figure 2-13 for example, is consistent with the trends of the GEM-3 measurements. A time-domain sensor capable of sampling the signal transient earlier is likely required to resolve any geological response in the time domain.

The EM63 is a heavy instrument with masses of 32 kg, 4.5 kg, 10 kg, for the sensor, console, and battery pack, respectively. The EM61 MkII masses 22 kg total for reference, 14 kg for the sensor and 8 kg for the backpack (electronics and battery). Given the signal drift rates associated with EM63 and the data collection protocols required to overcome these drift rates (see Section 2.2.4) and the physical stresses of making these measurements, a significantly lighter, preferably lower-drift rate sensor is required to make reasonable TEM geological response measurements.

Fortunately, such a sensor has recently become available to us. The TEM sensor developed by G&G Sciences for the MTADS Discrimination Array (ESTCP MM-0601) is significantly lighter than the EM63 (2.5 kg) and similar to the EM61 MkII-HH and the GEM-3 handheld models. The coils are wound on concentric stiff foam cores using a square coil design, with transmitter and receiver coil widths of 35 and 25 cm, respectively. The coils are wound in a non-overlapping pattern which leads to a coil height of 8 cm. Figure 4-2 shows an example of the completed coil assembly. The full decay curve can then be measured from 40  $\mu$ s to beyond 10 ms at 500 kHz. The recorded transients are either recorded as all points or binned into approximately 120 time gates. A lightweight amplifier is collocated with the coil assembly, increasing the maximum cable run to the electronics to at least 7m. At this time, the electronics and transmitter from the MTADS Discrimination Array can operate the sensor but an ESTCP-funded project to develop a handheld version is currently under way (ESTCP Project MM-0807). The existing Discrimination Array electronics may also be configured to act as an external background monitor, using the array's high-bandwidth D/A electronics. The system's 500 kHz bandwidth is more than double that of the NRL system and provides a high-quality amplifier to boost the recorded signal.

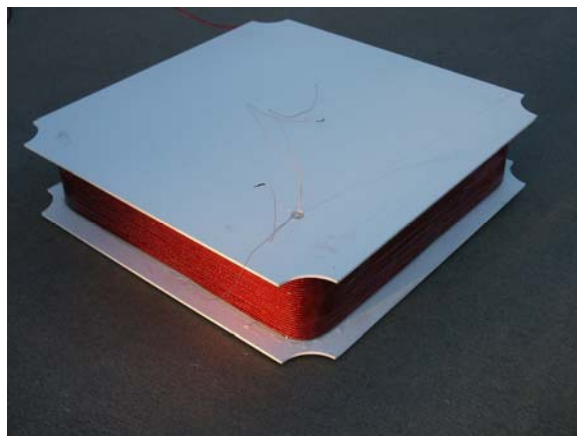


Figure 4-2 – EMI sensor developed during ESTCP MM-0601

Based on the quality and scope of the data that can be collected with the MM-0601 sensor, it is recommended that the MM-0601 replace the EM63 in future demonstrations for this project.

#### **4.1.2 Measurements**

Upon selection of the next demonstration site and mobilization to the site, 3 – 4 unique areas, or traverses, with at least 30m of usable area each will be selected for study. Soil moisture and magnetic susceptibility will be measured along each traverse with the ESI and Bartington instruments described in this report. The impact of external noise sources will be monitored using the GEM-3 and MM-0601 sensors. If a strong external noise source is identified such as a power line, measurements as a function of distance will be made with the GEM-3 and EM61 MkII to characterize the effects.

The geological response will be characterized with two methods along each traverse. The horizontal structure of the geological response will be measured with the GEM-3 and EM61 MkII sensors mounted on the MP cart as described in this report. At selected stations along each traverse that are free of compact anomalies, the vertical structure of the geological response will be determined using the modified procedure discussed in Section 3.7.3 using the GEM-3 and the MM-0601 sensors.

Motion-induced noise will be characterized for several modes of operation for EMI sensors. The data sets collected for the horizontal structure of the geological response will provide continuity with the Blossom Point measurements. The standard EM61 MkII wheeled configuration and a litter-carried variant will also be characterized. The addition of cm-level GPS and higher bandwidth IMU measurements will facilitate these measurements.

#### **4.1.3 Deliverables**

The results of the demonstration would be analyzed and the unique noise characteristics of the site determined and a site-specific guidance document would be generated. Comparison to past studies (initially to Blossom Point) would allow site managers and data collectors to make informed decisions about the appropriateness of the various sensor technologies on the site and the noise floor limitations on anomaly detection and classification.

### **4.2 EM61 MkII Simulation Tool Demonstration**

As was presented at the May 2008 IPR for this project, a scaled-back version of this effort more tightly focused on the ubiquitous EM61 MkII sensor potentially offers a higher cost to benefit ratio and more general applicability to the UXO community as a whole. Here we propose to couple one half day's measurements with an active EM61 MkII survey effort. These measurements could be helpful to survey data collectors and to the regulatory community. The inclusion of the dynamic response of the sensor does appear to have an impact on the overall performance of the data collection and processing methodology. Evaluation of the dynamic response impact on data from the site could guide the decision to use more advanced analysis methods or not.

#### **4.2.1 EMI Sensors**

As stated above, EM61 MkII sensor is the de facto standard instrument used in the UXO industry. As such, this effort would solely be focused on the EM61 MkII sensor. This measurement strategy is envisioned to be as “bolt-on” to an existing effort as possible. The

EM61 MkII and the positioning system (e.g. cm-level GPS) planned for the production effort would be used. A high-bandwidth IMU ( $\geq 25$  Hz rolloff) would be added to the survey platform to measure the platform orientation. If it is not feasible to include an IMU, orientation information from another appropriate source could be used if desired to estimate the effect of platform motion for the site, with the associated cost of degraded fidelity. A test coil with a switched contact would be used to measure the dynamic response parameters for the specific EM61 MkII(s) to be used as outlined earlier. A canonical test object with a well-characterized sensor response such as an Aluminum sphere would be used as well.

#### **4.2.2 Measurements**

Six classes of measurements would be made in the course of a half day. A long set (approximately 1 hour) of stationary data would be collected with the entire system (EM61 MkII, GPS, and IMU) previously warmed up and running. Several long transects would be surveyed with the entire system. Five to ten profiles, both horizontal and vertical in orientation, would be collected to characterize the soil response at the site. At three different heights above the ground, static calibration measurements would be made with the canonical object. Dynamic calibration measurements would be made by passing the system many times (approximately 10) over the canonical object placed on a hard-packed, flat surface. Non-reinforced pavement would be acceptable for these measurements. The dynamic response parameters would be determined for the specific EM61 MkII(s) using the switched test coil.

#### **4.2.3 Deliverables**

The deliverables from this effort would be an evaluation of the site-specific noise characteristics of the site and the EM61 EMI sensor, both in general and specifically for the tested units, for the classification of UXO items on the site. Additionally, the value added of using advanced modeling techniques such as dynamic inversion for data collected on site can be evaluated.

## 5. Cost Assessment

The costs for this demonstration are tabulated in Table 5-1.

Table 5-1 – Blossom Point Demonstration Costs

<b>Planning</b>		
Site Selection		4500
Demonstration Plan Preparation		9000
	<b>Total</b>	<b>13500</b>
<b>Data Collection</b>		
Field Data		
Nova		9000
NAEVA		12000
Nova		13500
SAIC		21000
Support (Data / Programming)		
SAIC		4200
NRL		5250
Rail System and Fixtures		32,400
	<b>Total</b>	<b>97,350</b>
<b>Equipment Rental</b>		
ESI Moisture Probe		1728
Bartington		800
	<b>Total</b>	<b>2,528</b>
<b>Data Analysis</b>		
Data Analysis		44800
Post-Demo Data collection		11200
	<b>Total</b>	<b>61056</b>
<b>Reporting</b>		
Demonstration Report Writing		13500
Symposium Poster and attendance		4500
IPR Prep and Presentation		4500
	<b>Total</b>	<b>22500</b>
<b>Grand Total</b>		<b>196,934</b>



## 6. References

1. "Report of the Defense Science Board Task Force on Unexploded Ordnance," December 2003, Office of the Under Secretary of Defense for Acquisition, Technology, and Logistics, Washington, D.C. 20301-3140, <http://www.acq.osd.mil/dsb/uxo.pdf>.
2. "Operating Instructions, EM61MK2 Data Logging System for Field Computer Allegro Field PC, EM61MK2A, v2.20," Geonics, Ltd., February 2005.
3. "Electromagnetic Induction and Magnetic Sensor Fusion for Enhanced UXO Target Classification," H. H. Nelson and Bruce Barrow, NRL/PU/6110--00-423 (September 15, 2000).
4. "Frequency Domain Electromagnetic Sensors for the Multi-sensor Towed Array Detection System," H. H. Nelson, B. Barrow, T. Bell, R. S. Jones, B. San Filippo, and I. J. Won, NRL/MR/6110--02-8650 (November 27, 2002).
5. "Demonstration of Basalt-UXO Discrimination by Advanced Analysis of Multi-Channel EM63 Data at Kaho'olawe, Hawaii," G. H. Ware, W. F. Tompkins, H. A. Ware, K. E. Lemley, and A. Z. Kostera, Proceedings of the UXO/Countermining Forum 2002, September 3-6, 2002, Orlando, FL.
6. Geologic Map of Charles County, Maryland, McCartan, Lucy, 1989, Maryland Geological Survey.
7. "Design and Construction of the NRL Baseline Ordnance Classification Test Site at Blossom Point," H.H. Nelson, J.R. McDonald, R. Robertson, NRL/MR-6110--00-8437 (March 20, 2000).
8. Y. Das, "Effects of Soil Electromagnetic Properties on Metal Detectors," IEEE Trans. Geosci. Remote Sens., vol. 44, no. 6, pg. 1444-1453, June 2006.
9. C. Bruschini, "A multidisciplinary analysis of frequency domain metal detectors for humanitarian demining," Ph.D. dissertation, Vrije Univ., Brussels, Belgium, 2002.
10. "Interpretation Theory in Applied Geophysics," F. S. Grant and G. F. West, McGraw-Hill, New York, 1965.
11. M. N. Nabighian, Ed., Electromagnetic Methods in Applied Geophysics, ser. Investigations in Geophysics no. 3. Tulsa, OK: Soc. Explor. Geophys., 1987, vol. 1 and 2.
12. S. Chikazumi, Physics of Magnetism. New York: Wiley, 1964.
13. T. Lee, "The effect of a superparamagnetic layer on the transient electromagnetic response of a ground," Geophys. Prospect., vol. 32, pp. 480-496, 1984.

14. Irma Shamatava, K. O'Neill, F. Shubitidze, K. Sun, and K.D. Paulsen (2005). Treatment of a permeable non-conducting medium with the EMI-BOR program, SPIE Defense & Security Symp 28 Mar – 1 Apr 2005, Orlando FL. PDF and code downloadable at <http://www.engineering.dartmouth.edu/uxo/>.
15. Jim Kingdon and T.H. Bell, "Processing and Analysis Results for MM-1310 Blossom Point Demonstration," SAIC Technical Report for MM-1310.

## 7. Points of Contact

POINT OF CONTACT	ORGANIZATION	Phone/Fax/email	Role in Project
Dr. Jeff Marqusee	ESTCP	Tel: 703-696-2120	Director, ESTCP
		Fax: 703-696-2114	
		Jeffrey.marqusee@osd.mil	
Dr. Anne Andrews	ESTCP	Tel: 703-696-3826	Deputy Directory, ESTCP
		Fax: 703-6962114	
		Anne.andrews@osd.mil	
Dr. Herb Nelson	ESTCP	Tel: 703-696-8726	Program Manager Munitions Management
		Fax: 703-696-2114	
		Herbert.nelson@osd.mil	
Ms. Katherine Kaye	HydroGeoLogic, Inc.	Tel: 410-884-4447	Program Manager Assistant Munitions Management
		kkaye@hgl.com	
Dr. Dan Steinhurst	Nova Research, Inc.	Tel: 202-767-3556	Senior Staff Scientist Co-PI of Project
		Fax: 202-404-8119	
		Cell: 703-850-5217	
		dan.steinhurst@nrl.navy.mil	
Mr. Glenn Harbaugh	Nova Research, Inc.	Tel: 301-392-1702	Site Safety Officer
		Fax: 301-392-1702	
		Cell: 804-761-5904	
		roo749@yahoo.com	
Dr. Tom Bell	SAIC – ASAD	Tel: 703-414-3904	Chief Scientist Co-PI of Project
		thomas.h.bell@saic.com	
John Breznick	NAEVA Geophysics, Inc	Tel: 434-978-3187	General Manager
		Cell: 434-825-8175	
		Fax: 434-973-9791	
		jbreznick@naevageophysics.com	
Jack Kaiser	Army Research Laboratory Blossom Point Facility	Tel: 301-870-2329	Facility Operations Specialist
		Fax: 301-870-3130	
		Cell: n/a	
		jkaiser@arl.army.mil	

## **Appendix A. Health and Safety Plan**

All survey operations took place in accordance with the United States Army Blossom Point Research Facility Standard Operating Procedures for Range Operations. The emergency procedures are outlined below, along with emergency contact numbers. A copy of this sheet were available to the crew at all times during the demonstration.

### **Emergency Procedures**

- A. The first priority during an accident/incident situation is to ensure timely and proper medical attention is provided to victims to prevent or reduce undue injury and/or save lives. In case of an accident requiring medical assistance or fire fighting backup, the Nanjamoy Rescue Squad and Fire Department will respond:

### **EMERGENCY –DIAL 911**

- B. All accident/incidents will be reported within one hour of occurrence to the following offices:

- (1) Directorate of Plans, Training, Mobilization and Security, 301-394-2739/5922
- (2) Security Office – 394-1100

Provide the following information:

- Name of caller
- Telephone number of caller
- Location of incident
- Assistance needed, i.e. number of persons injured, is ambulance required, etc.
- What type of procedures have already been taken
- Point of contact for further information, if needed

- (3) Explosive Test Operator for BPRF 301-870-2329
- (4) If accident involves helicopter from Ft. Belvoir also call Davidson Army Airfield, Commercial (703) 806-676/7220/7221/7672  
DSN 656-xxxx

- C. Calls will be made as described above and in the order shown and performed without delay.
- D. **ADDITIONAL NUMBERS:** Charles County Police – 301-932-2222 / 911  
LaPlata Fire Department – 301-8703781 / 911

Civista Memorial Hospital – 301-609-4160

749<sup>th</sup> EOD – 301-981-6218

Tech. Escort (APG) – 410-671-2773

Any deviation to this SOP must be approved by the Directorate for Plans, Training, Mobilizations and Security.

Health and Safety issues of particular importance include:

**Communications** – The survey team will maintain communications with range control at all times. Cellular telephones will be available to the crew as well as a range radio.

**Pretest Briefings** – Each morning the NRL program manager will brief the team on the objectives for the day. Then, the site safety officer, Mr. Glenn Harbaugh, will conduct a short briefing on any particular hazards expected to be encountered during the course of the day's operations.

**Hypothermia** – Prolonged exposure to cold weather can result in hypothermia if personnel are not dressed appropriately, or in the event of immersion. Care will be taken to ensure all field personnel are aware of the dangers of hypothermia, the appropriate procedures for the prevention and care of hypothermia, and are dressed appropriately for the conditions.

**Heat Stress** – Field operations during the summer months can create a variety of hazards to personnel. Heat cramps, heat exhaustion, and heat stroke can be experienced; and if not remedied, can threaten life or health. Therefore, it is important that all personnel are briefed on recognition of the symptoms and the appropriate procedures for the prevention and care of these conditions, and dressed appropriately for the conditions.

**Lyme disease** – The U.S. Army declared the Army Research Laboratory Blossom Point Facility to be a high risk area for contracting Lyme disease in a 1993 assessment report. The assessment found the Lyme disease tick, the Lyme disease bacteria in the ticks and mammals at the facility, and cases of human Lyme disease in the surrounding area.

## Appendix B. Dipole Model Framework

We have used the standard dipole model framework in which target response is expressed as a point dipole  $\mathbf{m}$  arising from primary magnetic field  $\mathbf{H}$  oscillating at frequency  $\omega$ :

$$\mathbf{m}e^{i\omega t} = V\mathbf{A}\mathbf{H}_0e^{i\omega t} \quad (1)$$

where  $V$  is the volume of the target and  $\mathbf{A}$  is the magnetic polarizability tensor:

$$\mathbf{A} = \begin{bmatrix} \alpha_{11} & \alpha_{12} & \alpha_{13} \\ & \alpha_{22} & \alpha_{23} \\ & & \alpha_{33} \end{bmatrix}. \quad (2)$$

Since  $\mathbf{A}$  is symmetric, the six terms in equation (2) are sufficient to define it. With suitable rotation matrix  $\mathbf{U}$ , the polarizability tensor may be diagonalized:

$$\mathbf{A} = \mathbf{U}\mathbf{B}\mathbf{U}^T$$

with

$$\mathbf{B} = \begin{bmatrix} \beta_1 & & \\ & \beta_2 & \\ & & \beta_3 \end{bmatrix}. \quad (3)$$

Under the “Full matrix” inversion algorithm, only the x,y,z coordinates of the target are searched non-linearly, and the  $\alpha$  terms in (2) are the values found by linear means within each iteration of the loop. Under an alternative approach, target orientation angles phi, theta, and psi are also searched non-linearly along with x,y,z, and the  $\beta$  terms in (3) are then found linearly within each iteration of the loop.